Grain boundary-dislocation interaction: A local investigation via micron-sized bicrystals

Dissertation

Zur Erlangung des Grades des
Doktors der Ingenieurwissenschaften (Dr.-Ing.)
der Naturwissenschaftlich-Technischen Fakultät III
Chemie, Pharmazie, Bio- und Werkstoffwissenschaften
der Universität des Saarlandes

Von

Nousha Kheradmand

Saarbrücken, Mai 2012

Tag des Kolloquiums: 10.05.2012
Dekan: Prof. Dr. W.F. Maier
Berichterstatter: Prof. Dr. H. Vehoff
Prof. Dr. F. Mücklich
Vorsitzender: Prof. Dr. R. Hempelmann
Akad. Mitarbeiter: Dr. Isabella Gallino

Contents

Acknowledgments

In the first place I would like to express my utmost gratitude to Prof. Dr. rer. nat. Horst Vehoff for his contribution to the completion this research work. I will never forget his insight into the world of science and his unique way of teaching and supervision, which makes one proud to be a scientist. Without his support and understanding during the beginning of the “baby time”, I may not have been able to finish my PhD now.

I gratefully acknowledge Prof. Dr. Ing. Frank Mücklich for accepting to being a part of the Reading Committee of this thesis, and also for his support all along my studies at Saarland University, specifically within the AMASE Program.

I would like to thank Christine Welsch, my diploma student, for performing multi-sided experiments, from lithography, to cutting pillars in FIB, to nanoindentation, and Vitoria Boiko, my HiWi, for performing the long-term heat treatments of Ni samples.

Many thanks go in particular to Dr. Ing. Michael Marx, a multi-talented colleague and friend in social life, for constructive scientific comments, to Dr. Ing. Afrooz Barnoush for his fabulous theoretical and experimental ideas anytime and performing the MD simulations of this thesis, to Kerstin Schüler and Dirk Hildebrecht for being such nice friends and having unforgettable time together, to Tao Qian for sharing the office and many interesting discussions about saving the world, to Mohammad Zamanzadeh for his support when I needed his helps and hearing me when I needed somebody to talk, to Alain Knorr for helpful discussions on the heat treatment of Ni and invention of a new imaging equipment for my Ni samples: his scanner!, to Dr. Ing. Wolfgang Schäf for assisting in the start the *theoretische Grundlage der Werkstoffwissenschften*, to Dr. Ing. Markus Welsch, our EBSD measurements master, to Dr. Ing. Mark Henning for leaving so many useful self-developed software behind for us, to Dr. Camille Perrin for bringing the French culture nearer to us.

Collective and individual acknowledgments are also owed to other diploma and master students in our group: Bastian Philippi, Vera Marx, Martin Weinmann, Michael Bick, Velayarce Jorge Rafael, Philip Kerger, Markus Mischo.

Many thanks to Stephan Schmitz and Peter Limbach whose handiwork and good ideas served to design my sample holders, and who were fast if I needed something urgently. I also thank Andreas Kirsch and Rita Maron for their availability and support for laboratory materials. Many thanks to Frau Ohm, who accompanied us in the institute almost until the end of my work, for making the administrative work easier, and Frau Born for being so practical and fast in response. To Frau Galli and Melani Groh many thanks for organizing our library very well.

I would like to thank Prof. Mao Wen from the school of Materials Science and Engineering at Shanghai Jiao Tong University in China for providing us with his MD simulation code and his support during the simulation of the bicrystalline micropillar

compression tests.

From the Institute of Functional Materials I would like to acknowledge Dr. Ing. Flavio Soldera, Christoph Pauly, Dominik Britz and Agustina Guitar for their support in the preparation of thin films, and special thanks to Paula Souza for the professional and quick English proof-reading.

From the Institute of Engineering Mechanics I would like to thank Dipl. Ing. Zhaoyu Chen for performing the FEM simulations of micropillar compression tests for this research and from the Institute of Technical Physic many thanks to Dipl. Ing. Jörg Schmauch for his assistance in performing the high resolution EBSD measurements.

Finishing this thesis would not have been possible for me without the incredibly nice people at the "Kindertagesstätte für Bedienstete der Universität des Saarlandes", specially Frau Hombücher, Nicole Wagner, Regiene Bleyer, Sandra and Manuela. I was extraordinarily fortunate in having you to take care of my child.

I would like to thank my parents, whose education and encouragement, love and sincerity brought me to where I am standing now; my brother and my other family members in Saarbrücken for their supports in all its forms; my parents in-law for their understanding and patience, and an angel in our neighborhood, Frau Hoffmann.

Finally, to my precious husband Afrooz, for your help especially in the crucial moments we spent together, for your permanently *good ideas* and your support in my scientific and daily life. And last but not least, my special thanks will be dedicated to my beautiful son *Suren*, for showing me that there is something more challenging than a PhD thesis.

Thank you all!

List of Tables

List of Figures

Abstract

In this research work, an experimental method is developed at the mesoscopic scale to investigate the interaction of dislocations with a selected grain boundary and its strengthening effect as a function of the grain boundary type.

The local mechanical testing method is based on microcompression tests of Focused Ion Beam (FIB)-cut bicrystalline micropillars with the component crystals oriented for single slip and multiple slip. Orientations identical to the experiments are used to generate models of the bicrystalline micropillars with up to four million atoms (140 nm in diameter) in Molecular Dynamics (MD) simulations. The compression test of these bicrystals is followed by Electron Backscatter Diffraction (EBSD) measurements on the bicrystal cross sections to investigate crystal lattice rotation in correlation with the excess dislocation density.

The microscopic test specimens are fabricated using high-voltage ion beam currents, which leads to the interaction of the ions with the host material. This problem, referred to as "FIB damage", was examined by high-resolution EBSD and nanoindentation techniques. The results show that FIB damage is a function of the ion beam current and the crystallographic orientation of the lattice, and that its main effect is the introduction of surface defects and the facilitation of dislocation nucleation.

Different sized bicrystals, from 1 to 5 μm in diameter, show different deformation behaviors. In bicrystals over 2 μm in diameter, identical flow stresses to single crystals with multiple slip orientation are obtained. These bicrystals resemble two single-crystalline micropillars connected in parallel and Taylor hardening is the responsible mechanism of deformation. Diameters below 2 μm, where the grain boundary-dislocation interaction plays a more crucial role than the dislocation-dislocation interaction, show a pronounced hardening effect of the grain boundary. Our EBSD measurements and the orientation analyses on the bicrystals with 1 μm diameters prove the increase of the misorientation in the vicinity of the grain boundary. In contrast, in a large bicrystalline micropillar with a 5 μm diameter, the orientation gradient is observed only in the bottom-up direction (parallel to the loading axis), which is a clear evidence of the independent deformation of the adjacent crystals. In agreement with the literature, lattice rotation is required for slip transmission and, thus, for compatible deformation of the bicrystals.

Zusammenfassung

Im Rahmen dieser Arbeit wurde eine experimentelle Methode entwickelt, um die Wechselwirkung zwischen Versetzungen und ausgewählten Korngrenzen, sowie ihre Verfestigungseffekte auf einer mesoskopischen Skala als Funktion des Korngrenzentyps zu untersuchen. Die lokale mechanische Testmethode basiert auf Mikro-Drucktests von Focused Ion Beam (FIB) geschnittenen bikristallinen Mikropillars, deren Einzelkristalle für Einfachgleitung sowie für Mehrfachgleitung orientiert sind.

Die gleichen Orientierungen werden benutzt, um Drucktests an bikristallinen Mikropillars mit bis zu vier Millionen Atomen mittels Molekular-Dynamik-(MD) Rechnungen zu simulieren. Im Anschluss an die Druckversuche wurden Electron BackScatter Diffraction (EBSD) Messungen auf der Querschnittsseite der Mikropillars durchgeführt, um die Gitterrotation des Kristalles in Korrelation mit Überschussversetzungen (excess dislocations) zu bestimmen.

Die Mikropillars wurden mit Ionenstrahlen hoher Beschleunigungs-Spannung hergestellt, was üblicherweise zu einer Wechselwirkung zwischen den Ionen und dem Probenmaterials führt. Dieses als “FIB Schädigungseffekt” bekannte Problem wurde durch hoch aufgelöste EBSD-Messungen und durch die Nanoindenter Messungen überprüft. Die Ergebnisse zeigen, dass die FIB Schädigung eine Funktion der Ionenstrahlstärke und der kristallographische Gitterorientierung ist und, dass ihr Haupteffekt die Erzeugung von Oberflächendefekten und dadurch eine erleichterte Versetzungsnukleation ist.

Unterschiedlich große Bikristalle von 1 bis 5 μm Durchmesser zeigen unterschiedliches Verformungsverhalten. In Bikristalle über 2 μm Durchmesser ist die Fließspannung gleich der Fließspannung einkristalliner Mikropillars, die für Mehrfachgleitung orientiert sind. Diese Bikristalle gleichen zwei einkristallinen “parallel geschalteten” Mikropillars wobei die Taylor Verfestigung die Verformung kontrolliert. Bikristalle unter 2 μm Durchmesser zeigen ausgeprägte Verfestigungseffekte der Korngrenze, wobei die Wechselwirkung zwischen Korngrenze und Versetzung eine wesentlich wichtigere Rolle als die Wechselwirkung der Versetzungen untereinander spielt.

Die EBSD Messungen an Bikristallen mit 1 μm Durchmesser und die darauf basierende Orientierungsanalyse weisen eine steigende Fehlorientierung in unmittelbarer Nähe der Korngrenze nach. Im Gegensatz dazu ist in einem großen Bikristall mit 5 μm Durchmesser der Orientierungsgradient nur in der “Bottom-Up”-Richtung (parallel zu der Belastungsrichtung) zu beobachten, was ein klarer Beweis für die unabhängige Verformung beider Einzelkristalle ist. In Übereinstimmung mit der Literatur konnte die Gleittransmission als Ursache für die Gitterrotation bestätigt werden und somit für die kompatible Verformung der Bikristalle als erforderlich identifiziert werden.

I would probably not say everything
I think, but definitely think all I say.

Gabriel Garcia Marquez

Chapter 1.

Introduction

If one excludes the single crystal research, one could claim that materials science is the science of interfaces [*Hirth*, 1972]. The topic of interfaces in materials is a broad one. It comprises boundaries between continuous, homogeneous grains of the same phase (e.g. grain boundaries or twin boundaries), or of different phases (e.g. phase boundaries). Through the further development of new materials, the crucial role of the grain boundary becomes more and more clear. Nanocrystalline materials are the most famous example. Because of the extremely small grain sizes (up to about 100 nm), a large volume fraction of atoms is located at the grain boundaries, which confers special attributes to these materials such as increased strength and/or hardness.

In other fields like fracture mechanics, among all the microstructural features altering the propagation of short cracks, grain boundaries have been observed to play a key role [*Ludwig et al.*, 2003]. They decrease the crack propagation rate as crack approach the boundary [*Schaef et al.*, 2011]. The grain boundary can be the crack initiation site in materials, if hard particles exist along it [*Han et al.*, 1996]. Experiments in different environments, e.g. for nickel-based alloys [*Lin et al.*, 1995] and for stainless steels [*Bruemmer and Was*, 1994], show that grain boundaries with no special crystallographic relationship between the adjacent grains are more prone to intergranular stress corrosion than certain “special” boundaries, which tend to have high degrees of lattice coincidence. The results of these studies have supported the generic concept of “Grain Boundary Design and Control” as first advanced by Watanabe [*Watanabe*, 1984].

To develop predictive models for grain boundary effectivity, more information is required about how the grain boundary crystallography and the orientations of its surrounding grains affect material properties. In the 1940s to 1960s, local studies on grain boundaries by mutual interaction of only two adjacent grains, i.e. a bicrystal, were used to investigate the local plasticity across a grain boundary. The vast amount of research focused on this topic was based on experiments in macroscopic scales which cannot necessarily be applied to small scale problems such as nanocrystalline materials. It is clear that novel studies are only possible by developing the available techniques and equipments. Atomic observation of grain boundaries was first made possible by the development of Transmission Electron Microscopes. In this size scale, it was possible to reveal fundamental mechanisms that take place *at* and *through* the grain boundary, but the shortcomings, like foil sample preparation and its influence on the microstructure, limit the capability of this method. A more detailed review of the literature is given in chapter 2. In this study, we developed a new experimental procedure in the mesoscopic scale to bridge the gap between the studied macroscopic and atomic length scales as mentioned above. Development of the Focused Ion Beam and Nanoindentation techniques made possible this research, which focused on the influence of the grain boundary on the plastic deformation and the flow stress. A precise explanation of the experimental procedure is given in chapter 3. We also used Molecular Dynamics simulation to answer the questions which could not be answered experimentally. The parameters used for simulation are presented in chapter 4. Chapter 5 provides the experimental as well as the simulational results. The results of the micromechanical tests, the simulation and the microstructural tests are displayed in separate sections, and after each section the results are discussed. A preliminary summary is given after the micromechanical and simulation results and discussion. Finally, the concluding remarks and the outlook for future works are presented in chapter 6.

Chapter 2.

Literature review

2.1. Grain boundary-dislocations interaction

Grain boundaries play an important role in materials science as a crucial feature controlling the mechanical behavior of materials. They are barriers to slip and hence confer strength on metallic materials. Paradoxically, grain boundaries are also sources of failure and weakness due to their relatively open structure compared to the lattice. The open structure allows the possibility of degradation between grains, potentially leading to reduced performance or even failure in service [*Randle*, 2010]. The modern concept of Grain Boundary Engineering was proposed by Watanabe [*Watanabe*, 1984] to improve the properties of polycrystals by manipulation of the structure to increase the proportion of special grain boundaries. This concept was used to improve resistance to various forms of intergranular degradation such as corrosion, embrittlement [*Bechtle et al.*, 2009] or cracking [*Gao et al.*, 2005]. However, for the successful application of Grain Boundary Engineering, it is necessary to identify the desired grain boundaries through local studies. For instance, artificial crack initiation in the vicinity of a grain boundary was developed by Schäf et al. [*Schaef et al.*, 2010] to investigate the interaction of short fatigue cracks with grain boundaries as microstructural barriers. It was shown that the crack growth rate always decreases, sometimes until a complete stop, while interacting with grain boundaries. The grain boundary blocks dislocations emitted from the crack tip and the emission of further dislocations becomes increasingly difficult, causing a decrease in the crack growth rate. The dislocation pile-up at the grain boundary was also used in the well-known Hall-Petch model to explain the increasing hardness in polycrystals by decreasing the grain size beyond ultrafine grained to nanocrystalline structures. However, any further grain refinement may lead to lower yield stress. In the range of smaller grain sizes the so-called *inverse* Hall-Petch behavior, i.e. softening with further reduction of grain size, was reported [*Pande and Cooper*, 2009]. Such discrepancies are the motivation for detailed studies on dislocation-grain boundary interactions. A local investigation of systematically altered grain sizes (from coarse grain to nanocrystalline materials) was performed using nanoindentation by Yang and Vehoff to provide a closer view of the grain boundary barrier effects (Figure 2.1) [*Yang and Vehoff*, 2007]. The variation of hardness was related to the interaction of the plastic zone below the indenter with the grain boundaries surrounding it. The dislocation pile-up in the indented grain activates new dislocation sources in the neighboring grains. Using in-situ nanoindentation in Transmission Electron Microscopy (TEM) on ultrafine grained materials, Hosson et al. visualized the propagation of dislocations and revealed the grain boundary motion as an important deformation mechanism in ultrafine grained materials [*Hosson et al.*, 2006]. Although a localized investigation method was used in these studies, the grain boundaries are crystallographically unknown and the obtained data is an average on all the grain boundaries under the indenter. Therefore, Soer et al. [*Soer et al.*, 2005] and Ohumra and Tsuzaki [*Ohmura and Tsuzaki*, 2007] performed nanoindentation near one defined grain boundary. The grain boundary-dislocation interaction was considered based on only the analysis of pop-in behavior and nanohardness, and no visual evidence was provided.

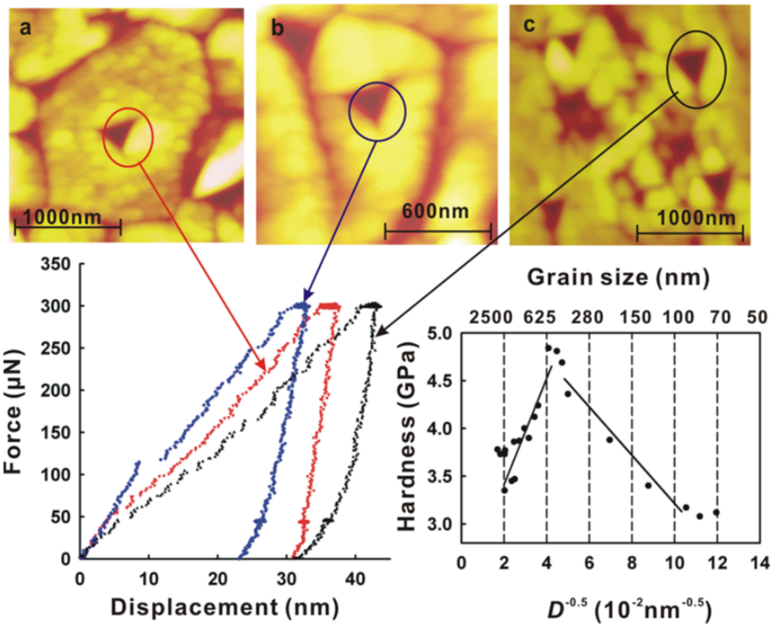

Figure 2.1.: Nanoindentation of polycrystalline nickel with variable grain sizes used as a grain boundary effect test method

Wilkinson et al. combined the nanoindentation near a grain boundary with Electron Backscatter Diffraction (EBSD) measurements to give an estimate of the total Geometrically Necessary Dislocation (GND) density distribution around the indent [*Wilkinson et al.*, 2010]. The map of the total GND distribution is shown in Figure 2.2, indicating that the slip penetrates a considerable distance into the adjacent grain. But how the slip transmission develops in the material interior is yet an open question, which can not be simply answered due to the complex stress and strain fields under the indenter.

In spite of so many efforts regarding the grain boundary-dislocation interaction as a crucial mechanism in polycrystals, for a better understanding, a systematic and precise local study with simple uniaxial stress distribution (in contrast to nanoindentation) is still required. This can be obtained by the application of crystallographically well defined *bicrystals*. In this way, each grain boundary can be characterized individually and, in contrast to the polycrystals, the obtained data is not an "average".

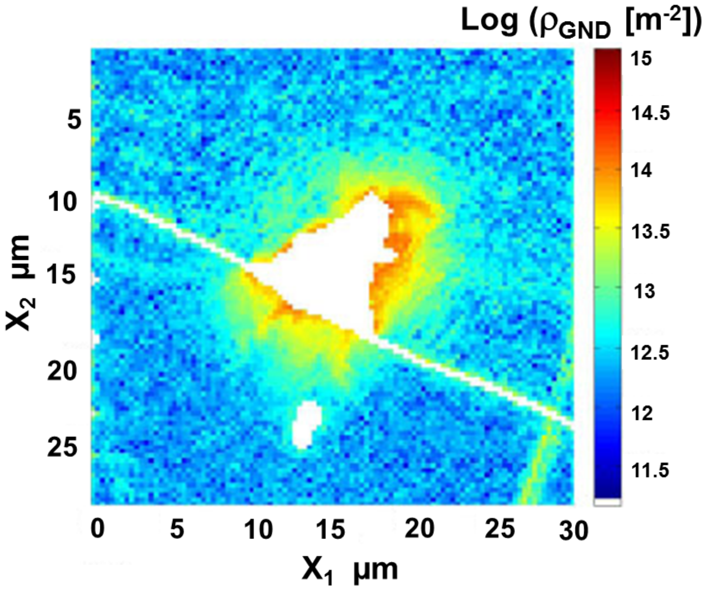

Figure 2.2.: The lower bound estimate of the total GND density distribution around the indent [*Wilkinson et al.*, 2010].

2.2. Bicrystals in the literature

2.2.1. Macroscopic bicrystals

Focused study on bicrystals was started by Chalmers on tin (tetragonal crystal structure) produced by means of the seeded growth method, which controls the orientation of each component crystal [*Chalmers*, 1937]. Thereafter, metal bicrystals with different crystallographic structures like nickel (FCC) [*Livingstone and Chalmers*, 1957], aluminum (FCC) [*Clark and Chalmers*, 1954; *Aust and Chen*, 1954] and Fe-3.3%Si (BCC) [*Sittner and Paidar*, 1989] were mechanically tested (under tensile or compression tests). Parallel to this method the perfect planar boundaries were produced by diffusion bonding [*Hauser and Chalmers*, 1961; *Hook and Hirth*, 1967a,b]. Measurements of the required stress for bicrystals yielding indicated that the grain boundary structure, i.e. misorientation angle of the component crystals, influences the bicrystal yield stress. Increasing the misorientation angle leads to higher yield stresses (Figure 2.3) [*Chalmers*, 1937; *Aust and Chen*, 1954; *Clark and Chalmers*, 1954]. Chalmers suggested that the critical shear stress of the bicrystals is determined by this misorientation angle and that the grain boundary has no inherent strength [*Chalmers*, 1937]. It is possible that the component crystals adjacent to the grain boundary in a bicrystal do actually begin yielding at the same stresses as the corresponding single crystals [*Gilman*, 1953; *Clark and Chalmers*, 1954]. To explain this, it was supposed that dislocations within the component crystals far away from the boundary may move at the same stress as in the single crystal. Then, the boundary causes the moving dislocations to pile up and effect a rapid increase in the stress necessary to move other dislocations and produce the large number of new dislocations required to cause observable deformation [*Clark and Chalmers*, 1954].

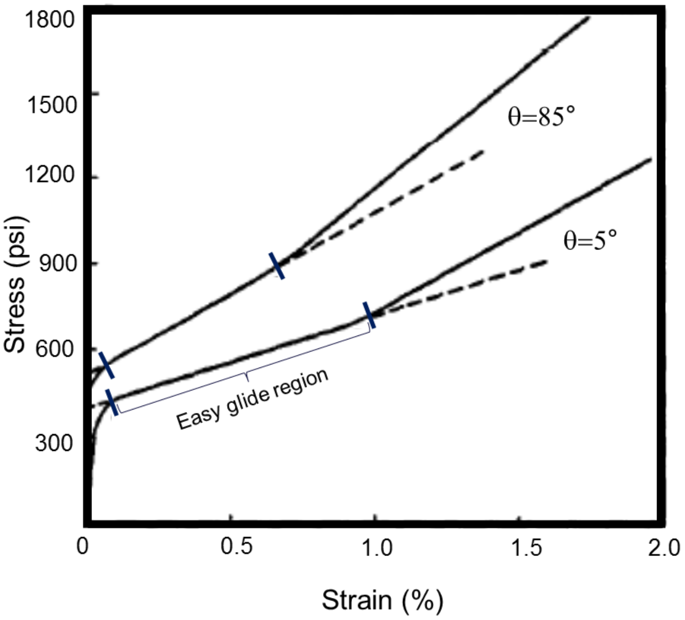

Figure 2.3.: The misorientation angle θ affect the flow stress curves of the bicrystals. The yield stress was defined as the stress obtained by extrapolating the easy glide region line to zero strain [*Aust and Chen*, 1954].

Deformation of these bicrystals was followed by careful observation of the slip lines on the free surface of bicrystals (Figure 2.4) [*Hauser and Chalmers*, 1961; *Hook and Hirth*, 1967a,b]. The macroscopic observations confirmed activation of secondary slip lines in the vicinity of the grain boundary, in addition to the primary slip systems which would be activated in the individual crystals if they were free. This resultant multiplicity of slip was shown to affect both the yield stress and the work-hardening of the bicrystal [*Livingstone and Chalmers*, 1957; *Clark and Chalmers*, 1954]. As a result of these studies, it was determined that the effect of grain boundaries on the flow stress is caused chiefly by the back stress of piled-up dislocations, the multiple slip due to compatibility at the boundary and the stress concentration of piled-up dislocations in the adjacent grain.

While some of the above-mentioned studies were in agreement with the strengthening effect of the grain boundary, Miura and Saeki showed that there is no difference in flow stress between the aluminum bicrystal having different misorientations and the component single crystals (Figure 2.5) [*Miura and Saeki*, 1978]. The results of their study on isoaxial symmetric bicrystals with different misorientations (4°, 14° and 37°), have shown that in bicrystals with large angles of misorientation (37°), slip cannot pass through the boundary in contrast to the small angle misorientations. Clustered slips were suppressed at the boundary and the stress concentration due to dislocation pile-ups against the grain boundary is relaxed by inducing slip in the neighboring grain. Therefore, they denied that back stress contribution due to groups of dislocation pile-

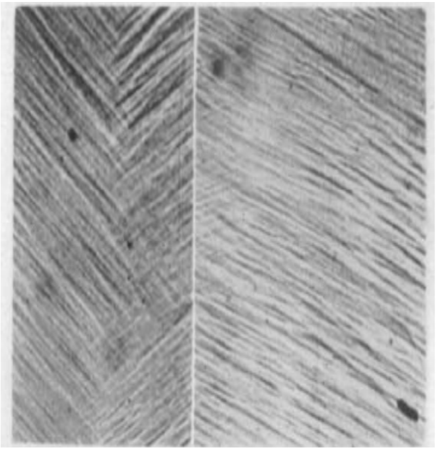

Figure 2.4.: A photomicrograph showing double glide in the vicinity of the grain boundary in a specimen with the misorientation of 85°: ×100 [*Aust and Chen*, 1954]. The two dimensional view on the lateral surface of a macroscopic bicrystal was used to study the grain boundary effect on the deformation of the bicrystal.

ups against the grain boundary is a factor causing increase in flow stress at large strain (2 %) in the bicrystal. They proposed that the main effect of the grain boundary on the flow stress is to introduce multiple slip at the beginning of deformation [*Miura and Saeki*, 1978]. A similar suggestion was given by [*Hook and Hirth*, 1967a,b]. Due to both *elastic and plastic incompatibilities* of the adjoining crystals, activation of at least four slip systems is required to fulfill the continuity conditions at the grain boundary (see Appendix A).

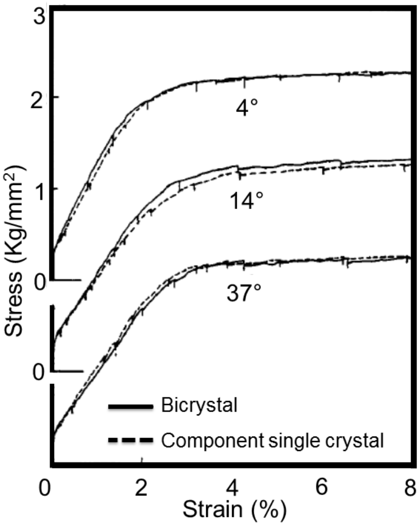

Figure 2.5.: Stress-strain curves of (100) bicrystals having 4°, 14° and 37° misorientation boundaries compared with the component single crystals [*Miura and Saeki*, 1978].

In a study on aluminum bicrystals Rey and Zaoui considered the intragranular slip heterogeneity at the beginning of the plastic deformation in each component crystal, which was not discussed in detail in the previous works [*Rey and Zaoui*, 1979]. Their model was successfully used for copper bicrystals [*Rey and Zaoui*, 1982] and pointed out that the introduction of some intergranular plastic incompatibility does not alter the process initiating the slip heterogeneities.

These types of examinations of bicrystals, including mechanical testing followed by slip line observations could not, with the limited equipments of that time, deliver more information about the dislocation-grain boundary interactions. The development of EBSD technology was later used by Sun et al. to study the lattice rotation near the grain boundary of deformed aluminum bicrystals [*Sun et al.*, 2000]. At low strains pile-up of GNDs due to high lattice rotation near the grain boundary was observed, while their distribution changed dramatically with further deformation. The complex nature of the GND distribution near the boundary suggests that substantial differences may be expected in the deformation as a function of boundary character. A decade later Field and Alankar performed the same experiment on copper bicrystals [*Field and Alankar*, 2011]. Intermittent observation of interrupted deformation has illustrated that a region near the boundary is strongly influenced by neighboring grain deformation (Figure 2.6). The experiments demonstrate a rotation in the lattice that is different from the rotation that might be predicted by the current understanding of texture evolution. They proposed that this difference might be explained by the strong slip transmission effects that are present, since the component crystals essentially shared a dominant slip system. There is still a need for an improved understanding of the effect of the grain boundary on deformation in the adjoining crystallite.

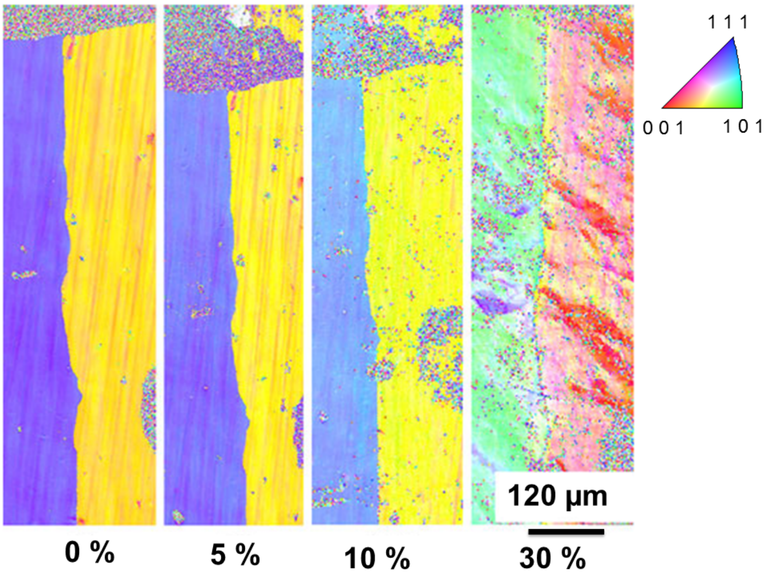

Figure 2.6.: Orientation images showing the successive progression of lattice orientation after 30 % compression [*Field and Alankar*, 2011].

2.2.2. Microscopic bicrystals

The main disadvantage of the macroscopic compression test of bicrystals was the limitation of the slip line observation on the surface of the bicrystals which delivered only a two dimensional view of the activated slip systems. Since the macroscopic observations cannot be extrapolated to microscopic problems, investigation of the grain boundary as a barrier to dislocation motion was continued by means of the powered TEM technique. This method was used to analyze the contributing mechanisms.

2.2.2.1. TEM observation method

Ex-situ TEM observations by [*Darby et al.*, 1978; *Bamford et al.*, 1986; *Shen et al.*, 1986; *Elkajbaji and Thibault-Desseaux*, 1988] made it possible to investigate the interaction of dislocations with the grain boundary at higher resolution. For this purpose, thin films containing at least two grains were prepared from already deformed polycrystalline bulk samples. Dislocation pile-up and slip transmission was confirmed by high-resolution TEM (HRTEM) observations (Figure 2.7).

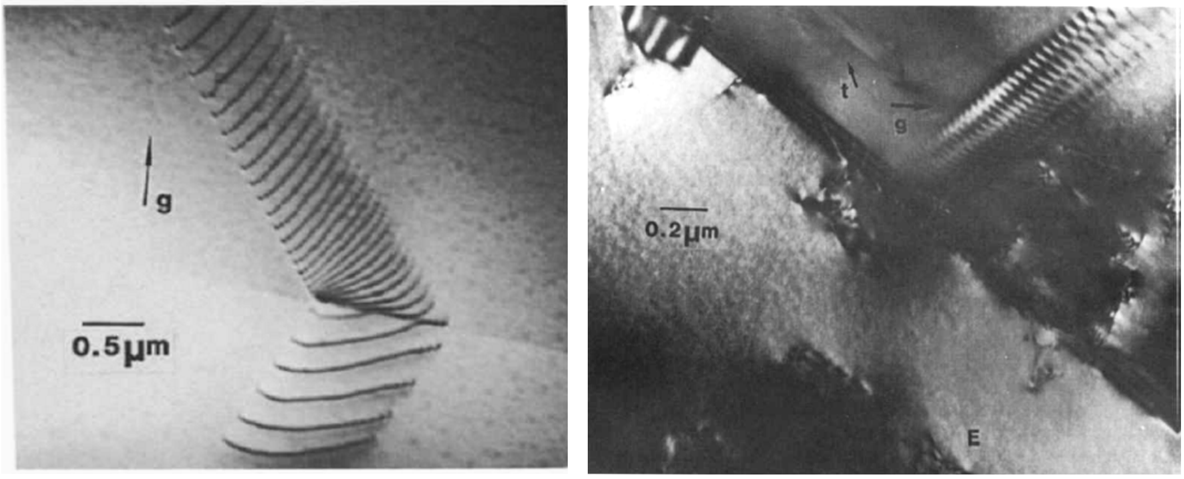

(a) **(b)**

Figure 2.7.: (a) Slip transmission observed by the ex-situ TEM experiment. (b) Similar interaction event observed in an in-situ TEM experiment [*Shen et al.*, 1988].

In-situ straining experiments in TEM [*Shen et al.*, 1988; *Lee et al.*, 1989, 1990], specifically on miniaturized bicrystals [*Baillin et al.*, 1987, 1990; *Gemperle et al.*, 2005], was performed as a complementary analysis method to the ex-situ TEM analysis. Quantitative results obtained for the dynamic dislocation transmission across a grain boundary, i. e. the prediction of the emitted slip plane and direction, were found to agree with those obtained from the ex-situ TEM experiment (Figure 2.7b). The qualitative observations of both ex-situ and in-situ experiments proposed that several mechanisms can accomplish the slip transfer from one grain to the next. These are as follows: nucleation of new dislocations (Figure 2.8a) [*Bamford et al.*, 1986], direct transmission of dislocations (Figure 2.8b) [*Lee et al.*, 1990] or the absorption and desorption of dislocations into and out of the grain boundary.

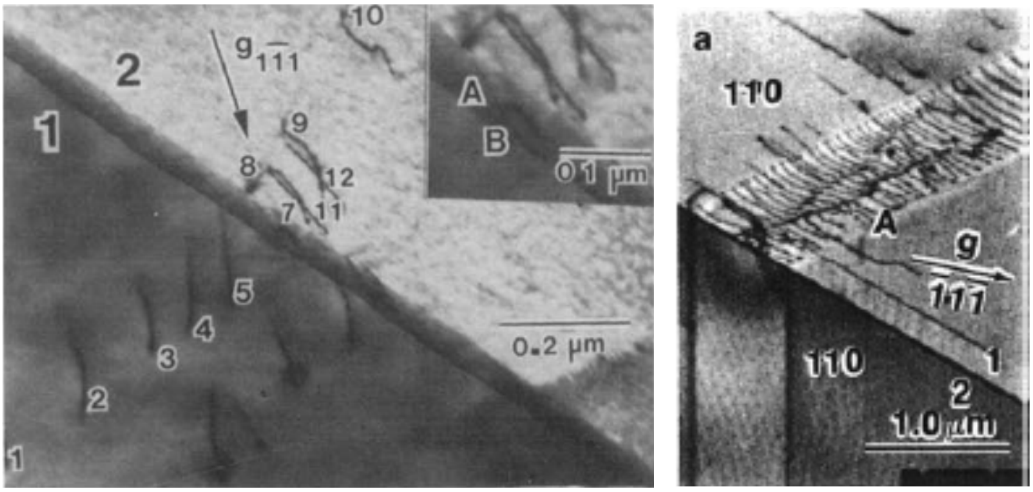

(a) **(b)**

Figure 2.8.: (a) Dislocation (1-5) pile-ups in crystal 1 generate sufficient stress to nucleate new dislocations (7-10) in crystal 2. The origin of dislocations 11 and 12 is unclear. [*Bamford et al.*, 1986]. (b) Direct transfer of dislocations through a grain boundary [*Lee et al.*, 1990].

TEM studies, as an alternative studying method, provide direct observation of grain boundary-dislocations interaction in smaller length scales, but the studies by TEM thin film preparation result in some relaxation of a previously deformed microstructure, which may lead to a change in the dislocation structure. On the other hand, the area observed in TEM foil is very small and therefore not representative for the whole sample. Finally, since no quantitative data about the mechanical effect of the grain boundary is available from these experiments (e.g. stress-strain curves), an alternative method is still missing.

2.3. Criteria on slip transmission

Three basic criteria are proposed by [*Livingstone and Chalmers*, 1957], [*Shen et al.*, 1988] and [*Clark et al.*, 1992] to predict the slip transmission based on macroscopic bicrystal deformation and microscopic TEM observations. Only the last version of criteria by [*Clark et al.*, 1992], which was developed based on the other two prime criteria, could successfully predict the slip transmission in accordance with the observations. The other two criteria were not satisfactory in terms of slip prediction and therefore are given in Appendix B. In this new criterion, Clark et al. and Lee et al. proposed a modified set of conditions [*Clark et al.*, 1992] as follows.

1. The Geometric Condition:

The crystallography of the boundary determines the angle θ, at which incoming and potential outgoing slip planes meet in the interface (Figure 2.9). This means that when an incoming dislocation arrives at the boundary, it must rotate its line direction by θ in order to align itself with the slip plane in the other crystal. In general, this process requires climb and provides a considerable obstacle to dislocation transmission, especially at low temperatures. Therefore, in this criterion, the slip plane for which θ is a minimum is chosen for dislocation emission. This is the slip plane for which M is a maximum (Equation 2.1),

$$M = L_1 \cdot L_i \tag{2.1}$$

where L_1 and L_i are the intersection lines of the incoming and the potential outgoing slip planes with the grain boundary, respectively. It should be noted that θ will change with the boundary plane orientation, even if the relative misorientation between the crystals remains constant. Thus, we should expect that for the same incoming slip system, different emitted slip systems will be activated in different regions of the same, curved, boundary. This possibility is not considered in the first criterion.

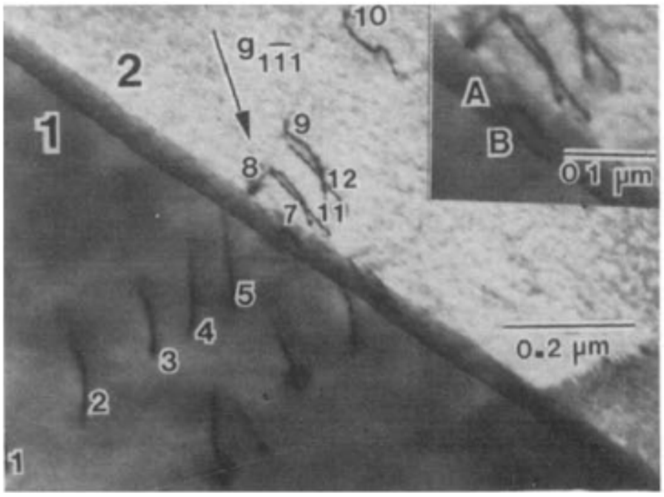

Bamford-clarck86,static, Nucleation-after

Figure 2.9.: Schematic diagram showing the geometrical relationship between the incoming and outgoing slip planes and θ [*Clark et al.*, 1992].

2. The Resolved Shear Stress Condition:

   Once the emitted slip plane has been determined, the most likely slip direction to be activated (within that slip plane) is that on which the resolved shear stress is maximum [*Clark et al.*, 1992]. The stress resolved on each potential slip system may be obtained directly from the stress field on the emission side of the boundary, or may be inferred from the glide force acting on a test dislocation introduced in the same location. These two steps were applied in a comprehensive study, using in-situ straining experiments. It was found that there were some cases in which the criterion did not unambiguously predict the emitted slip system for certain boundaries, but gave almost identical resolved shear stresses for two or more systems. These resolved stresses were so close that it was considered that the differences between them were too small to provide a definitive prediction [*Clark et al.*, 1992]. Therefore, a third step was added to this criterion.

3. The Residual Grain Boundary Dislocation Condition:

   The Burgers vector of a grain boundary dislocation $\vec{b}_{\text{grain boundary}}$ which is formed when a dislocation of grain A passes through the boundary and moves into grain B, can be represented as $\vec{b}_{\text{grain boundary}} = \vec{b}_A - \vec{b}_B$ where $\vec{b}_A$ and $\vec{b}_B$ are the Burgers vectors when a dislocation lies on grains A and B, respectively. Therefore, the Burgers vector of a grain boundary dislocation depends on the misorientation between $\vec{b}_A$ and $\vec{b}_B$. With a large misorientation, a boundary dislocation with a large Burgers vector is required to form, which is energetically unfavorable. It is energetically more favorable for a dislocation with a Burgers vector $\vec{b}_A$ in grain A to pass to a dislocation on the slip system of grain B with a Burgers vector $\vec{b}_B$ having a smaller misorientation than $\vec{b}_A$ [*Miura and Saeki*, 1978]. In other words, the magnitude of the Burgers vectors of this residual dislocation should be minimized. This and the resolved shear stress condition determine the active slip direction.

2.4. Mesoscopic bicrystals

Increasing interest in devices of reduced dimensions such as thin films, interconnects and Micro-Electro-Mechanical Systems (MEMS) calls for the development of investigation methods of appropriate length scales. These new technological devices are in a mesoscopic size scale, below which a solid no longer behaves as bulk. They deal with the physics of small condensed objects, often in the nanometer size regime, hence with a collection of atoms in contrast to atom physics. Importantly, it is assumed that the sample is large on the atomic scale, such that fluctuations in the number of atoms contained in the sample are not important. That is why the term *Meso* is used (in between a single atom and a bulk solid) [*Schoenenberger*, 2001].

Recently, Uchic et al. [*Uchic et al.*, 2004] developed the compression test for micropillars in the mesoscopic size scale using a flat-ended tip in a nanoindenter. This method was extensively used by many authors in order to study the size-dependent flow stress in much simpler stress and strain fields than nanoindentation tests. Pillars with diameters in the range of some tens of nanometers to some tens of micrometers were investigated in different materials including Ni [*Dimiduk et al.*, 2005; *Norfleet et al.*, 2008], Cu [*Kiener et al.*, 2006, 2007a,b, 2008a,b, 2009a,b], Mo [*Schneider et al.*, 2009b,a; *Greer et al.*, 2008; *Bei et al.*, 2007; *Kim and Estrin*, 2008; *Zaiser et al.*, 2008], NiTi shape memory alloy [*Frick et al.*, 2008], Ni_3Al [*Afrin and Ngan*, 2006], oxide dispersed alloy [*Pouchon et al.*, 2008], Au [*Volkert and Lilleodden*, 2006; *Greer et al.*, 2005; *Lee et al.*, 2009; *Brinckmann* *et al.*, 2008], nanoporous Au [*Biener et al.*, 2006; *Zepeda-Ruiz et al.*, 2007], nonmetallic systems like LiF [*Nadgorny et al.*, 2008], Si [*Östlund et al.*, 2009; *Jennett et al.*, 2009; *Gerberich et al.*, 2009], GaAs [*Michler et al.*, 2007] and $MgAl_2O_4$ [*Korte and Clegg*, 2009]. Presently, the flexibility of Focused Ion Beam (FIB) for cutting micropillars provides new possibilities for studying other topics than size effect. In this study a new method is proposed, which concentrates particularly on the plasticity in the near-grain boundary region. This is the most important area to investigate the plasticity of polycrystals, since earlier works on bicrystals showed multiple slip in the vicinity of the grain boundary, and recent EBSD measurements of bicrystals demonstrate that a region near the boundary is influenced strongly by neighboring grain deformation. Compression tests of bicrystalline micropillars with accompanying lattice rotation investigations in the sample interior combines the direct observation of the slip lines on the deformed bicrystal surfaces, with the measurements of flow stress curves and local misorientations. The results of these test methods and analyses provide an accurate understanding of the role of the grain boundary in deformation of polycrystalline materials. With the present method, small-scale bicrystals can be cut from an arbitrary grain boundary of a polycrystalline material via FIB. It is particularly of advantage for some metals, whose bicrystals cannot be fabricated by other methods like seeded growth technique. The micron-sized pillars exclude other possible barriers to dislocation motion, such as Lomer-Cottrell sessile dislocations, and provide higher accuracy in the determination of the grain boundary strength. For the cases where the study of segregations on the grain boundary is of interest, it is also easy to prepare bicrystals with segregated grain boundaries. This method provides a new perspective in the study of the interaction of the dislocations with the grain boundary.

Chapter 3.

Experimental procedure

Performing mechanical tests at the micron scale is more or less a combination of art and science. It means you have to perform tests on samples that you never see with your naked eyes and your interpretation must be done on the basis of indirect observation. Therefore, extraordinarily careful preparation of the samples, with documentation of each step during the sample preparation as well as testing, are the keys to successful measurements. In this chapter, a thorough overview of the procedures used to prepare, mechanically test and post-characterize the sample will be given.

3.1. Sample preparation

Sample preparation for micropillar compression tests can be divided into *macroscopic sample preparation* (bulk samples) and *microscopic sample preparation* (micropillars) steps. Due to the complexity of each step, they will be explained separately.

3.1.1. Macroscopic sample preparation

High purity nickel (99.99 %) was used as a model material to prepare the macroscopic samples. These were cut by an electrical discharge machine with a brass wire. The localized high tempretaure of this cutting tool produces an oxide layer contaminated with copper and zinc on the specimen surfaces. Since in the subsequent annealing process these elements can diffuse into the samples, pin the grain boundaries and impede the desired grain growth, it is neccessary to completely remove this layer. Hence, all six surfaces of the specimens were first ground and then mechanically polished.

In order to cut a microscopic bicrystal on the top of a polycrystalline sample, a grain boundary perfectly perpendicular to the surface is indispensable. It may sounds easy but, in practice, it is a very time-consuming procedure to achieve such a grain boundary. A special procedure was developed to produce microstructures with a perfectly vertical grain boundary. The procedure sequences are displayed schematically in Figure 3.1. From the thermodynamic point of view a perfectly vertical grain boundary can be achieved within a two-dimensionally microstructured material in complete equilibrium conditions. The specimen dimensions can influence the rate of grain growth and, when the average grain size approaches the thickness of the specimen, the free surface effect can completely stop grain growth [*Reed-Hill and Abbaschian*, 1994]. This implies that the grain growth rate is proportional to the sample size. Therefore, long-time heat treatments (3 days) at 1250 °C were performed on the bulk samples with 15 mm × 15 mm × 10 mm dimensions (as shown in Figure 3.2a left), in order to obtain coarse grains with diameters in the order of several millimeters (Figure 3.1a). Subsequently, plates with thicknesses less then the average grain size (≈ 2 mm) were cut from these coarse grained bulk samples (Figure 3.1b), which resulted in two-dimensionally microstructured samples (as shown in Figure 3.2a middle). Another long-time heat treatment (3 days) at 1300 °C for these plates to reach a complete equilibrium ensured the formation of grain boundaries perpendicular to the surface of the sample (Figure 3.1c).

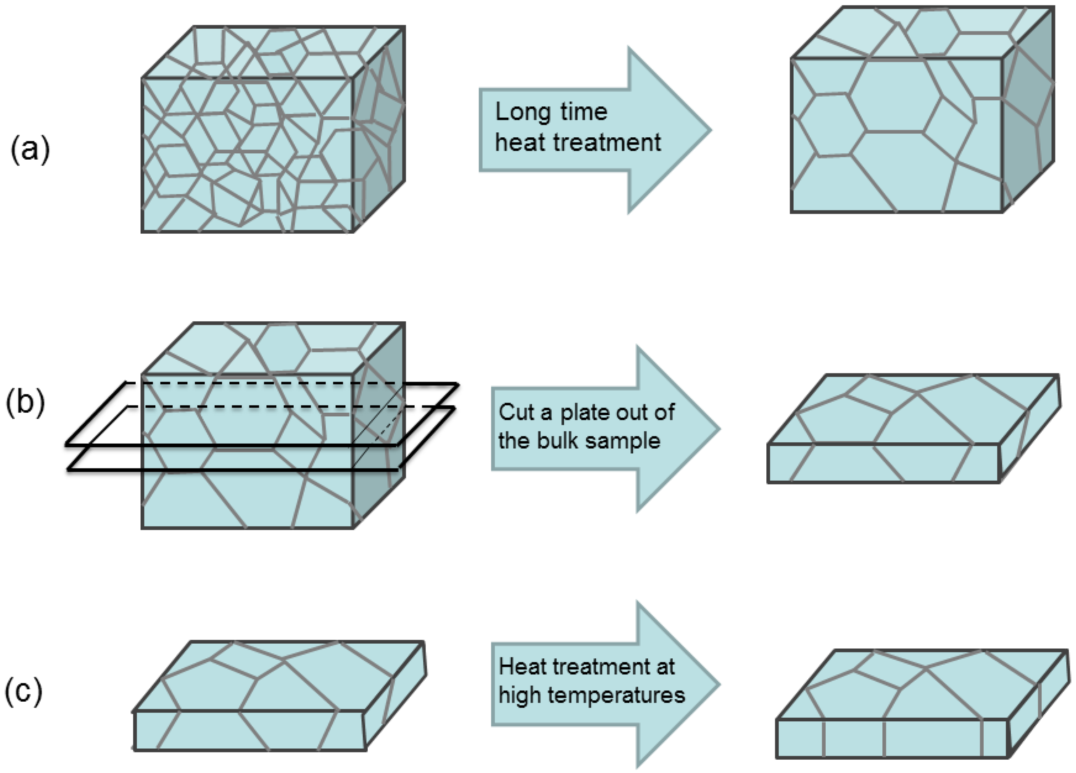

Figure 3.1.: The special procedure developed for production of two-dimensional, structured samples. (a) Long-time heat treatment of bulk samples for grain growth. (b) Plates were cut, with thicknesses less than the average grain size to obtain two-dimensionally microstructured samples. (c) A second heat treatment results in the formation of grain boundaries prependicular to the surface.

All heat treatments mentioned above were performed in a vacuum better than 10^{-5} mbar and followed by cooling in the furnace to obtain a very low defect density. The specimen surfaces were electropolished prior to and after the heat treatments. Electropolishing before heat treatment is necessary in order to have a perfectly clean surface, free from any pinning points, to enhance grain growth. Electropolishing after the heat treatment serves to have a perfectly reproducible surface condition for all tests.

Another set of samples with 30 mm × 30 mm × 2 mm dimensions (as shown in Figure 3.2a right) were cut from the same starting material and used to produce pillars using lithography (see section 3.1.2.2). These plates were heat-treated at 1000 °C for 1.5 hours and again 1200 °C for 24 hours in order to have an average grain size about 100 μm.

The surface preparation of all sample geometries was similar. To obtain a defect-free, clean and reproducible surface condition, all samples were electropolished. However, mechanical polishing to a fine state before electropolishing, for example 3 μm diamond paste, is needed to shorten the electropolishing time, since long-time electropolishing may result in a wavy surface or local overheating of the sample. For homogeneous electropolishing, an individual sample holder was designed and constructed for each sample geometry (Figure 3.2b). Electropolishing was performed using the commercial LectroPol-5 electropolishing machine from Struers. Table 3.1 summarizes the sample and surface preparation parameters used for all types of geometries shown in Figure 3.2a.

Table 3.1.: Sample and surface preparation parameters

Preparation step	Parameter	Value
Surface preparation	Grinding paper grades	600, 1000, 2500 and 4000
	Mechanical polishing	6 μm and 3 μm diamond suspensions
Annealing	Temperature (°C)	1000-1250-1300
	Time (h)	72 to 1200
Electropolishing	Solution	1 molar H_2SO_4 in methanol
	Voltage (V)	30
	Time (s)	30-90

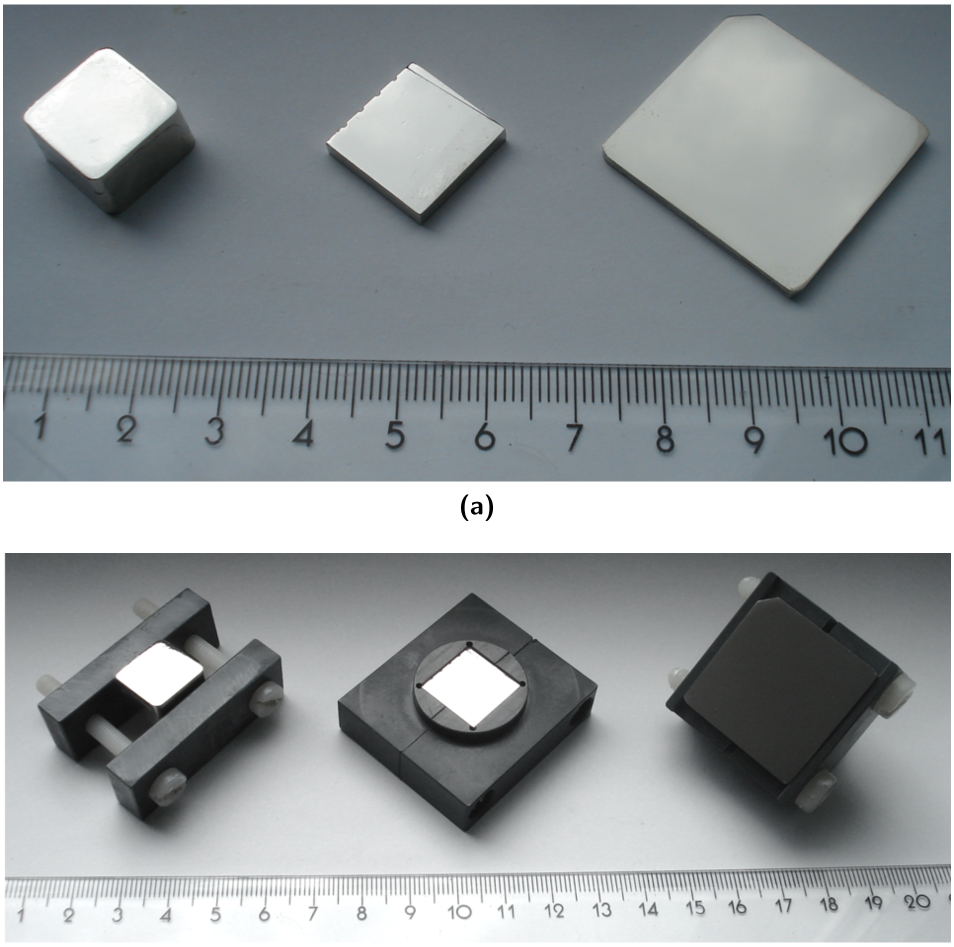

(a)

(b)

Figure 3.2.: (a) Nickel sample geometries employed in this work. (b) Sample holders designed for electropolishing of different sample geometries shown in (a).

3.1.2. Microscopic sample preparation

Two different methods were used to produce microscopic samples, i.e. micropillars. The first method, which is normally found in the literature as a classical method for the fabrication of micropillars, is FIB milling. A dual beam FIB system was used to cut the micropillars from a specified grain boundary as well as from the grain interior, to produce bicrystalline and single-crystalline micropillars, respectively. In the second method, the photo-lithography technique, combined with electrochemical etching and subsequent FIB milling, was used to fabricate micropillars. While the fabrication of single-crystalline pillars is possible by FIB as well as by lithography, the bicrystalline pillars were fabricated only by FIB milling, since with the lithography technique the probability of fabricating a bicrystal on a defined grain boundary is very low. To increase that probability, the lithography mask would have to be pre-programmed specially for each plate in question and be scanned on the surface by laser. Hence, precise positioning of the desired grain boundary in the pillar is only possible via the masks available in FIB.

Hence, from here on, pillars fabricated by only FIB milling will be called “FIB-Pillars” and those fabricated by the combination of lithography and FIB techniques will be called the “FIB-Litho-Pillars”.

3.1.2.1. FIB-Pillars

In order to fabricate bicrystals with a defined grain boundary, knowledge about the orientation of the grains in the polycrystalline samples is required. The EBSD technique was used to characterize the crystallographic properties of the prepared bulk and plate samples. With the knowledge of the misorientation angle/axis of the two adjacent grains (Appendix C), the grain boundary normals and assuming that the grain boundary is prependicular to the sample surface, the type of the grain boundary was characterized. The scalar product of the grain boundary normal ($\vec{n}_{\mathrm{GB}}$) and the rotation axis ($\vec{n}_{\mathrm{rotation}}$) determines the type of the grain boundary (Figure 3.3). If it is zero, the grain boundary is a twist grain boundary, other wise it deals with a tilt grain boundary. This information is summarized in Table 3.2 and show that the grain boundary in question is a *tilt* grain boundary.

Table 3.2.: The considered grain boundary parameters

Parameter	Value
Misorientation of adjacent grains (angle/axis)	$38°/(8\ 10\ \bar{1})$
Grain boundary normal in grain with single slip orientation	$\approx (1\ 3\ \bar{1})$
Grain boundary normal in grain with multiple slip orientation	$\approx (\bar{1}\ 1\ \bar{2})$

Figure 3.4 shows, for instance, the Orientation Imaging Microscopy (OIM$^{®}$) map of coarse-grained nickel and the selected grain boundary (Figure 3.4). Bicrystalline micropillars of different diameters were cut on this grain boundary. Single-crystalline

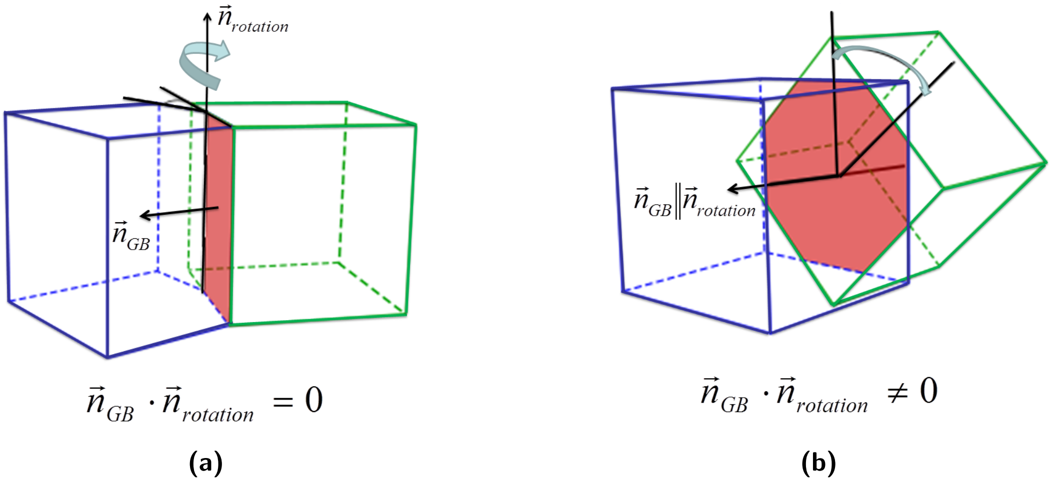

Figure 3.3.: The grain boundary was characterized according to grain boundary type definitions. The scalar product of the grain boundary normal and the rotation axis ($\vec{n}_{\mathrm{GB}} \cdot \vec{n}_{\mathrm{rotation}}$) determines the type of the grain boundary: (a) tilt grain boundary or (b) twist grain boundary.

micropillars with different sizes, in the same range as the bicrystals, were cut in the interior of the adjacent grains. The cutting tool was a Strata® dual beam 235 FIB (DB-FIB) system manufactured by the FEI® company. The FIB column on this instrument supplies 30 kV Ga^+ ions at beam currents ranging from 0.01 to 20 nA. In a first step, higher beam currents in the range of 20 to 3 nA were used for coarse milling a tapered pillar, surrounded by a large cavity, as a pre-form. This step is the most time-consuming part of the cutting procedure. A large cavity around the pillar is needed for the following purposes: (i) imaging the sidewalls of the micropillar, both before and after deformation, using Scanning Electron Microscopy (SEM) or FIB, (ii) ensuring that the flat-ended tip does not contact any other surfaces than the micropillar, (iii) lessing the probability that sputtered material will redeposit back onto the freshly-milled micropillar in the next cutting steps, and (iv) facilitating locating the micropillar using the optical microscope in the nanoindenter system [*Uchic and Dimiduk*, 2005]. In a second step, the smaller ion beam currents in the range of 0.5 to 0.1 nA were used for fine milling and removing the tapering of the pillars in several short-time steps. During the milling process the sample surface is tilted at 52°, so that the ion beam hits the sample surface perpendicularly. Figure 3.5 shows different views of the electron and ion beams for a typical micropillar on the tilted bulk sample.

The orientations of the crystals adjoining the grain boundary were chosen so that in one grain, with crystallographic orientation near {1 5 3}, single slip is enhanced, forcing the dislocations toward the grain boundary and making the pile-up at the grain boundary. The other grain with a crystallographic orientation near {1 1 1}, was oriented for multiple slip, which allows for dislocation multiplication and interaction, and hence for hardening and compatible deformation. These soft-hard oriented adjacent crystals allow the study of the grain boundary barrier effect on dislocation motion. In Table 3.6

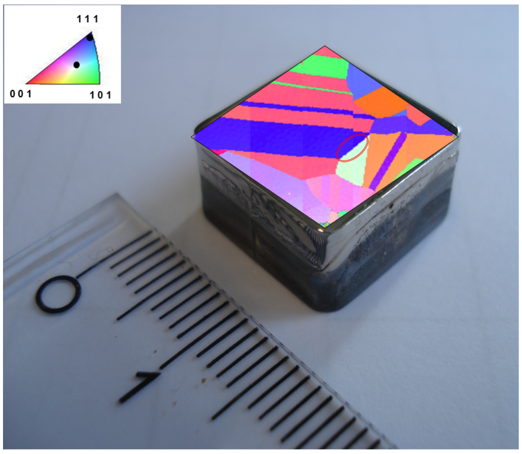

Figure 3.4.: EBSD map of the polycrystalline bulk sample surface used to produce micropillars. The marked grain boundary, with adjacent grain orientations shown in the inverse pole figure, was selected for fabrication of bicrystals.

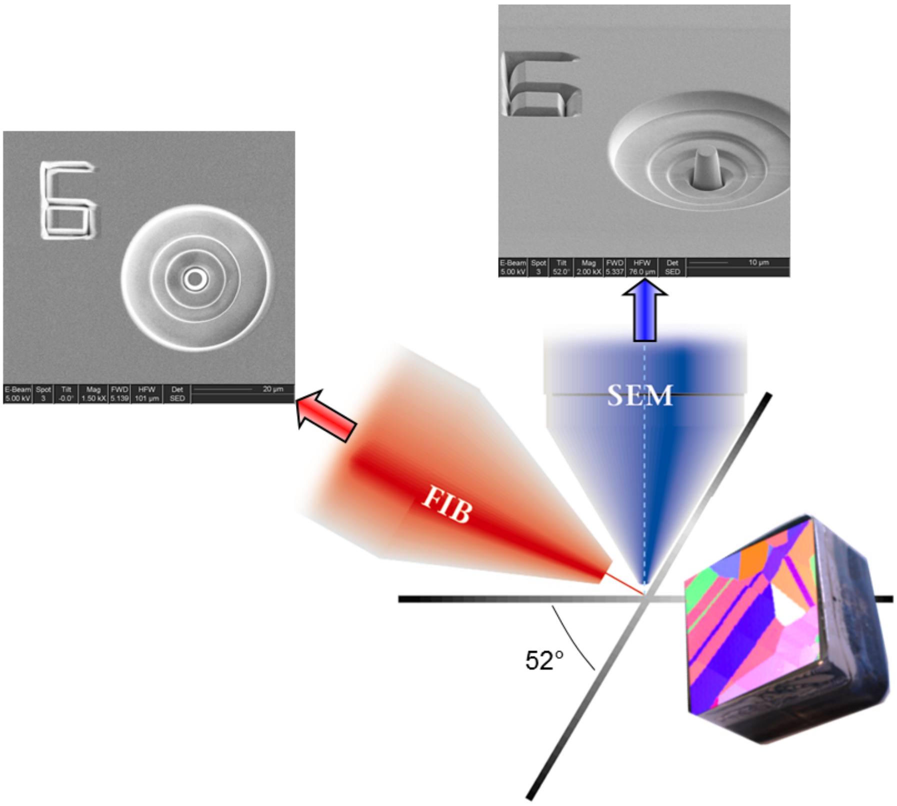

Figure 3.5.: Different views from the electron and ion beams of a typical micropillar cut in a DB-FIB.

the properties of the two counterpart crystals of the grain boundary are given. Figure 3.6 shows the SEM image, with Secondary Electron (SE) contrast, of a typical bicrystalline micropillar cut on this grain boundary, and with an aspect ratio (relation of height to diameter) of ≈ 2. A visible effect due to different crystallographic orientations of grains is a step produced at the grain boundary as shown. This issue can be related to the different milling rates of the two crystal orientations, referred to as *sputtering channeling*, due to the different ion-atom interaction modi. The incident ions on the material surface undergo inelastic as well as elastic interactions. In inelastic interactions (called electronic energy loss), ion energy is lost to the electrons in the sample and results in ionization and the emission of electrons and electromagnetic radiation from the sample. In elastic interactions (called nuclear energy loss), ion energy is transferred as translational energy to the target atoms and can result in damage (displacement of sample atoms from their initial sites) and sputtering from the sample surface. In the easy channeling orientations (here the $\{1\ 5\ 3\}$ orientation), the ion experiences only inelastic glancing-angle collisions with the atoms lying in a crystal plane and travels deeper into the crystal before causing elastic collisions, so that fewer atoms are sputtered from the surface [*Volkert and Minor*, 2007].

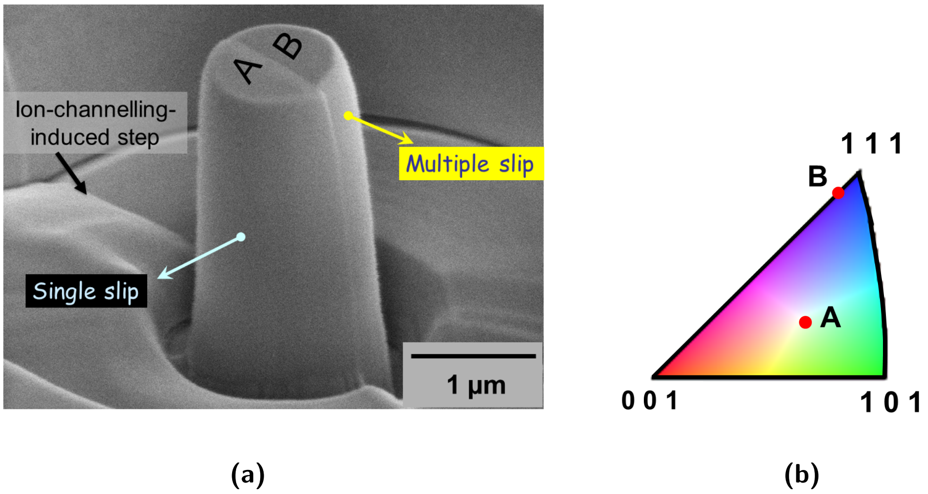

(a) **(b)**

Figure 3.6.: (a) The SEM image of a typical bicrystalline micropillar with diameter $\approx 1.4\,\mu$m with SE contrast. The orientation contrast makes the planar grain boundary observable. (b) Crystallographic orientation of the component crystals of the studied bicrystal.

3.1.2.2. FIB-Litho-Pillars

A novel technique was developed in this work through the combination of FIB and lithography to produce micropillars[1]. The motivation for using lithography was to reduce the fabrication time of micropillars. As mentioned in the last section, a large

---

[1] The experiments regarding the production of FIB-Litho-Pillars were performed by Dipl. Ing. Christine Welsch as part of her diploma thesis.

cavity around the micropillar is inevitable but costly in terms of time. Substituting this step by lithography followed by electrochemical etching as a less time-consuming method will help to increase the statistic of the experimental studies. In this way, a vast amount of pre-forms were made via lithography and subsequent electrochemical etching in one step (as shown in Figure 3.9) and the production of pre-forms in FIB which requires high ion beam currents (20 to 3 nA) and long time per each pillar will be obsoleted. Then, in a second step, these were milled to their final sizes using the FIB low ion currents (0.5 to 0.1 nA) and so the extreme tapering form of lithography-made pillars due to isotropic etching can be corrected (Figure 3.7).

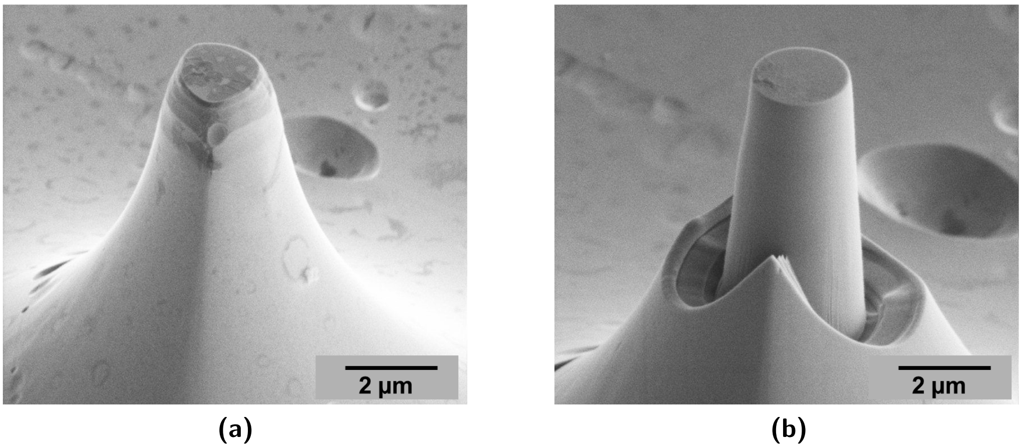

Figure 3.7.: (a) SEM image, with SE contrast of a pillar produced by electrochemical etching before FIB milling. (b) The same Litho-Pillar after FIB milling.

For the fabrication of pillars by lithography the plates shown in Figure 3.2a right were structured by a glass mask within the lithography process. A standard lithographic process is shown in Figure 3.8. With a ultraviolet beam and the glass mask, ordered circular patterns are produced manually on the coated substrate. The photo-sensitive lacquer AZ 1518 from AZ Electronic Materials® was used to cover the surface via the spin-coating equipment from Süss MicroTec®, model RC 8, in which the sample dimension are constrained to a defined size of 30 mm × 30 mm × 2 mm. In order to stabilize the polymer film on the surface, the coated samples were heated at 100 °C for 25 s. The layer has a final thickness of 25 μm. In a subsequent *development step* using the AZ 351B developer at the ratio of 1:4 (4 parts deionized water), the exposed polymer is then selectively removed, while the unexposed portions of polymer layer remain intact on the substrate in circular forms (Figure 3.9). The parameters used are shown in the Table 3.3.

In order to fabricate three dimensional structures, the structured plates were electrochemically etched. Table 3.4 summarizes the electrochemical etching parameters. The lithography and wet etching procedures are described in detail in [*Welsch*, 2010]. As the wet etching process is in general associated with isotropic etching (Figure 3.10b left), the form of the Litho-Pillar is not a perfect cylinder (Figure 3.10a). In order to fabricate ideal, cylindrical pillar forms, an anisotropic etch mechanism is of interest (Fig-

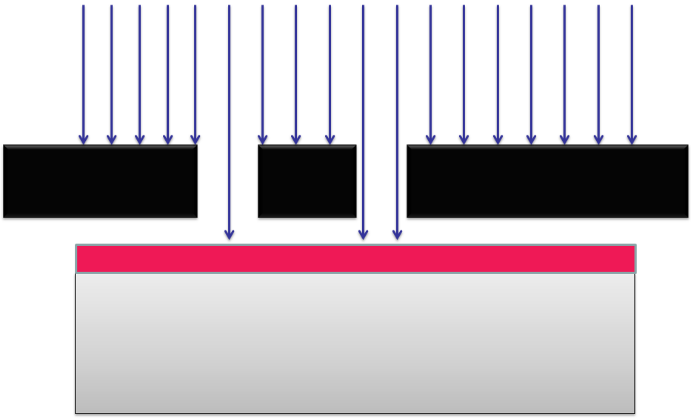

Figure 3.8.: Standard lithography procedure.

Table 3.3.: Lithography parameters in this study.

Parameter	Value
Spin-coater velocity (rpm)	3000
Coating time (s)	60
Exposure time (s)	50
Development time (s)	25

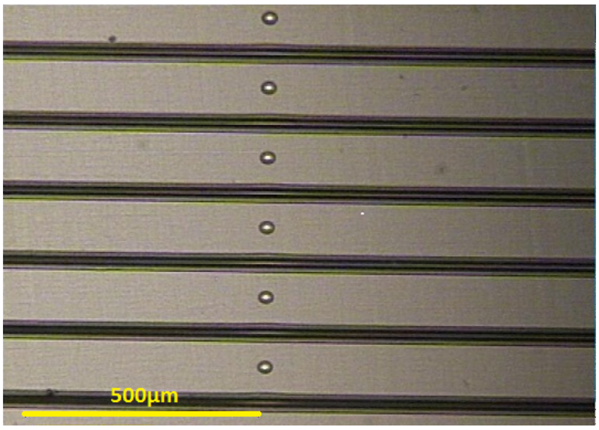

Figure 3.9.: Light microscopy image made by normal contrast of lithographically-produced, structured specimen. The circles are the produced pre-form micropillars.

ure 3.10b right). This is in principle possible by means of dry etching, which is available in three types: physical, chemical, and a combination of both physical and chemical techniques. In these methods, however, ion beams are used, which leads again to ion implantation problems in the same manner as using FIB [*Welsch*, 2010].

Table 3.4.: Electrochemical wet etching process parameters.

Parameter	Value
Etching solution	57 % H_2SO_4
Voltage (V)	5
Etching times (s)	30, 60, 90 and 120

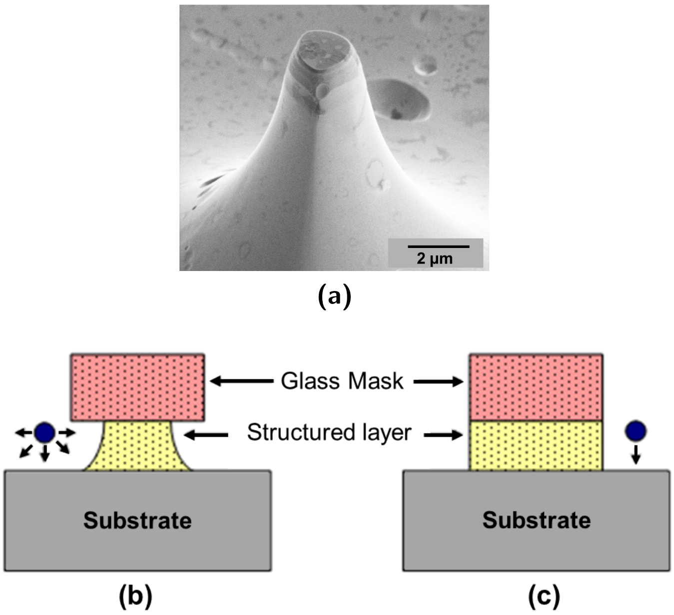

Figure 3.10.: (a) SEM image with SE contrast of a pillar produced by electrochemical etching. The shape of the pillar is a consequence of the (b) isotropic etching of nickel. For a perfectly cylindrical form of the pillars, (c) anisotropic etching is of interest.

As an example, Table 3.5 compares the time and the beam current used for the fabrication of such a FIB-Litho-Pillar with those of a pure FIB-Pillar of 5 μm average diameter. This indicates considerable savings in time, ion beam and money using this new development, especially for large pillars. Figure 3.11 compares these two techniques for a better overview. Only the FIB milling steps are considered.

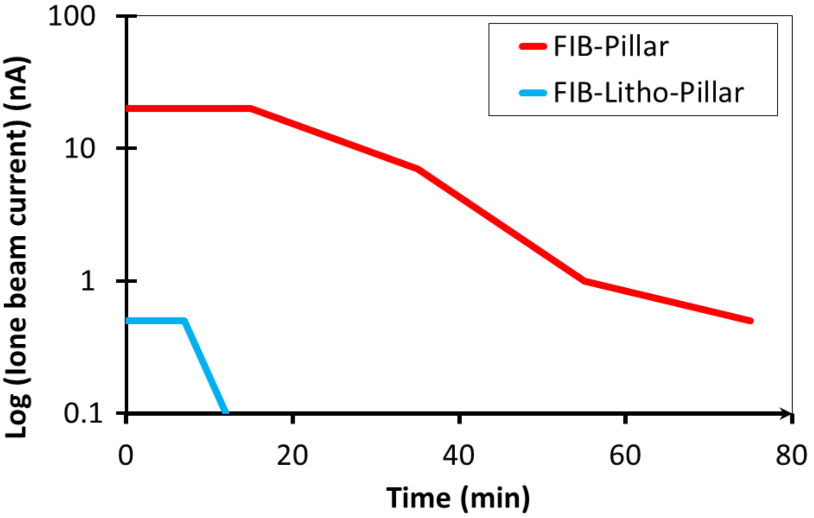

Figure 3.11.: The curves compare the two mentioned fabrication techniques: FIB-Pillars and FIB-Litho-Pillars. The ion current intensity used and the time consumed in FIB are considered.

Table 3.5.: Two 5 μm diameter micropillars, each fabricated with a different technique, are compared in terms of time and beam current intensity.

	FIB-Litho-Pillar	FIB-Pillar
Time requirement	Lithography: 15 min per hundreds of pillars Electrochemical etching: 2 min per hundreds of pillars FIB milling: 12 min per pillar (varies with size)	75 min per pillar
Beam current	0.1-0.5 nA	0.1-20 nA

3.2. Characterization of microscopic samples

For a reproducible interpretation of results, each single pillar has to be characterized before undergoing mechanical testing. However, since the pillars were fabricated in different ways, their characterization was also performed in a different order. Table 3.6 includes the crystallographic orientations of all the micropillars examined in this study and Figure 3.12 shows them on an inverse pole figure.

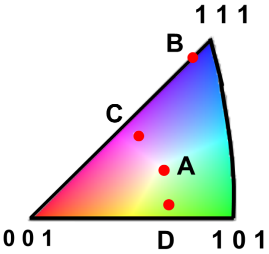

Figure 3.12.: Crystallographic orientation of all the grains used for fabrication of micropillars studied.

3.2.1. FIB-Pillars

Fabrication of FIB-Pillars was performed on an already characterized bulk sample. Therefore, no further characterization in terms of crystallographic orientation was needed. As the pillars were cut selectively on grains with defined crystallographic orientations, and their dimensions were measured directly after the cutting process in FIB by taking SE contrast SEM images, they were assumed to be ready for mechanical testing.

3.2.2. FIB-Litho-Pillars

The characterization of FIB-Litho-Pillars was more complicated than that of the FIB-Pillars, as described below. The macroscopic Ni plate samples for fabrication of Litho-Pillars are polycrystalline with an average grain size of 100 μm. As the grains have random orientations, the etching rate in each grain is different. On the other hand, the structured mask has a predefined distribution of circular patterns at constant distances, which will be transfered to the plate. Hence, micropillars with different orientations and sizes will be fabricated using lithography and subsequent electrochemical etching. These pillars were characterized in SEM to determine their dimensions by direct observation, as well as their orientations by OIM. Through OIM, the local lattice orientation can be measured using backscattered electrons. The resulting diffraction pattern captured from only one point on the pillar's top surface is sufficient to determine the crystallographic orientation of that pillar. For this, the SEM image of the pillar top-view was strongly magnified and the electron beam was directed onto the pillar surface. The obtained

Kikuchi patterns with Euler angle indications were then indexed in the OIM analysis software to obtain the orientations in other forms like $(h\ k\ l)\langle u\ v\ w\rangle$.

Table 3.6.: Crystallographic orientation, Schmidt factor and elastic modulus of the grains included the single and bicrystalline pillars.

Grains	$(h\ k\ l)[u\ v\ w]$	Schmidt Factor		Elastic Modulus
		partial dislocation	perfect dislocation	
A (Single slip)	$(1\ 5\ 3)[1\ \bar{2}\ 3]$	0.48	0.49	182
B (Multiple slip)	$(\bar{6}\ 5\ 5)[\bar{5}\ \overline{17}\ 11]$	0.31	0.27	258
C (Single slip)	$(\overline{12}\ 25\ \bar{9})[\overline{39}\ \overline{18}\ 2]$	0.43	0.46	181
D (Double slip)	$(11\ 1\ 18)[2\ \bar{4}\ \bar{1}]$	0.46 and 0.43	0.49 and 0.47	177

3.3. Micromechanical examinations

Pillars with different diameters were compressed in a Hysitron® TriboIndenter™ nanoindentation system equipped with a diamond flat-ended tip. The tip size was chosen such that it was at least 2 times larger than the pillar diameter, so that the pillar could be positioned centric to the tip for a homogeneous load distribution. Therefore, different sizes of flat-ended tips with 5, 10 and 20 μm in diameters were used. Figure 3.13 shows a schematic view of the TriboIndenter™ in some detail with a macroscopic sample installed on the motion stage. For a better understanding, the SEM images of the indenter tip, here the flat-ended tip, and the microscopic sample, here a typical micropillar, are shown magnified.

3.3.1. Positioning of micropillars under the flat-ended tip

In order to position the micropillar under the flat-ended tip as centrically as possible, the in-situ imaging capability of the nanoindentation system in the TriboIndenter™ was used. By installing the bulk sample on the motion stage and finding the pillar's position with the optical microscope, the chosen pillar, ready to indent, was moved automatically

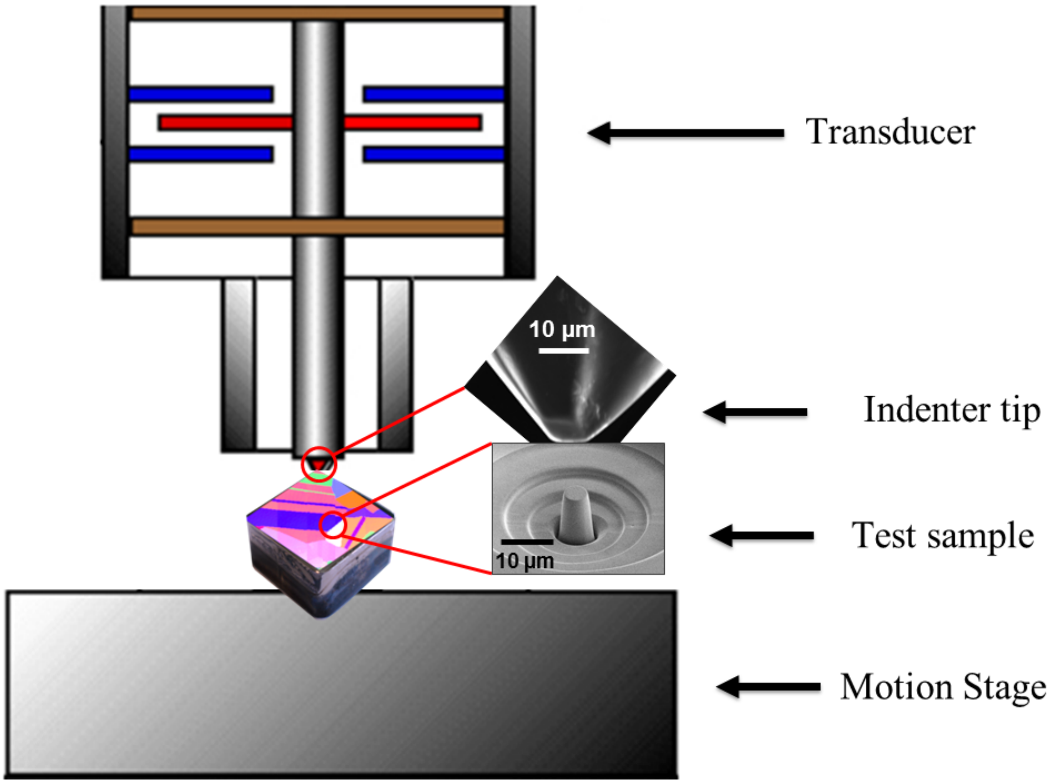

Figure 3.13.: A schematic of the TriboIndenter™ and the bulk sample installed on the stage. The SEM images of a flat-ended tip and a typical micropillar are shown magnified.

under the tip. The tip scanned the top surface of the pillar and provided a topography image with the relative positions of the tip and the pillar. If the position of the pillar was deviated from the center of the image (Figure 3.14a), where the indentation would have been done, it was manually positioned in the center point by moving the stage (Figure 3.14b). Figure 3.14 shows typical topography images of a pillar with a diameter of 1 μm imaged with a 20 μm diameter flat-ended tip. However, the diameter of the imaged micropillar is much larger than the pillar's real diameter. This is because, during the scanning, the flat-ended tip has already been imaged by the pillar due to the small size of the pillar relative to the tip. Therefore, in addition to the pillar diameter (1 μm), the tip diameter (20 μm) is also included in the image.

The reason for the difference between the scan profile and the real surface geometry is the well-known problem in all scanning force microscopy methods, referred to as "tip-sample convolution". Its consideration is important when studying small surface features (of the order of the tip curvature radius). A finite tip dimension results in the lack of ability to probe narrow cavities on the sample surface, thus decreasing their depth and width. Inversely, convex feature images appear wider [NTM]. The convolution phenomenon is best understood from the schematic in Figure 3.15, as the flat-ended tip starts to image the micropillar. The tip trajectory gives the imaging topography shown in Figure 3.14.

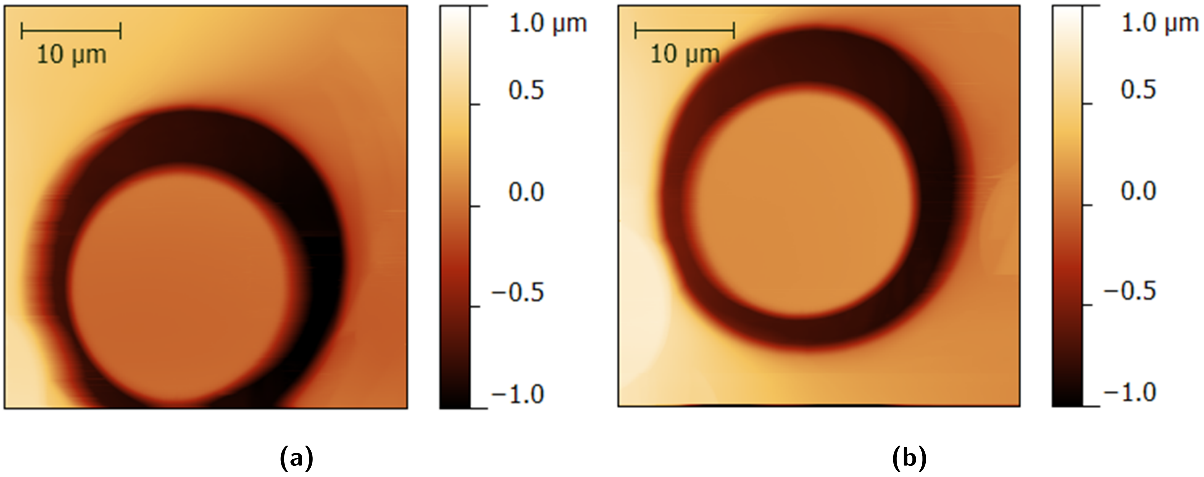

Figure 3.14.: The topography images of the pillar surface scanned by the flat-ended tip (a) before and (b) after centering the position of the micropillar.

3.3.2. Loading procedure

At the beginning of the tests, using periodic load function (Figure 3.16a) the specimens were incrementally loaded in order to measure the yield point precisely. In the obtained load-displacement curve, the yield point is defined as the point at which the unloading curve starts to deviate from a linear relationship (Figure 3.16b).

The Hysitron® nanoindenter transducers are inherently force-controlled and the obtained stress-strain curve is shown in Figure 3.17a. Incremental strain bursts under constant loads during the plastic deformation are due to the load-controlled nature of the test, and are related to the avalanche of dislocations under constant load. This phenomenon hinders our control over the real straining rate of the pillars during the test. In order to control the deformation strain rate during the test, the indenter was equipped with displacement feedback control software. As shown in Figure 3.17b, instead of strain bursts (in load control mode) load drops (in displacement control mode) are observed. This enables the control of the deformation rate, except for cases where the feedback loop is not fast enough to stop the plastic instabilities. Therefore, the feedback gains for displacement controlled compression should be tuned as accurately as possible [*Hysitron*, 2006]. To find the best gain, we used pillars from the pseudo-elastic (superelastic) shape memory alloy CuZnAl (Figure 3.17c). In contrast to Ni, these pillars could be loaded and unloaded several times (Figure 3.17d). Since the austenite to martensite transformation under stress shows the same behavior as the plastic instabilities, the PID control values of the feedback loop extracted from the compression tests on pseudo-elastic pillars were successfully used for micropillars.

We performed the compression test experiments under displacement control with loading rates of 1, 10 and 100 nm/s. For tests under load control we used a loading rate of 100 μN/s.

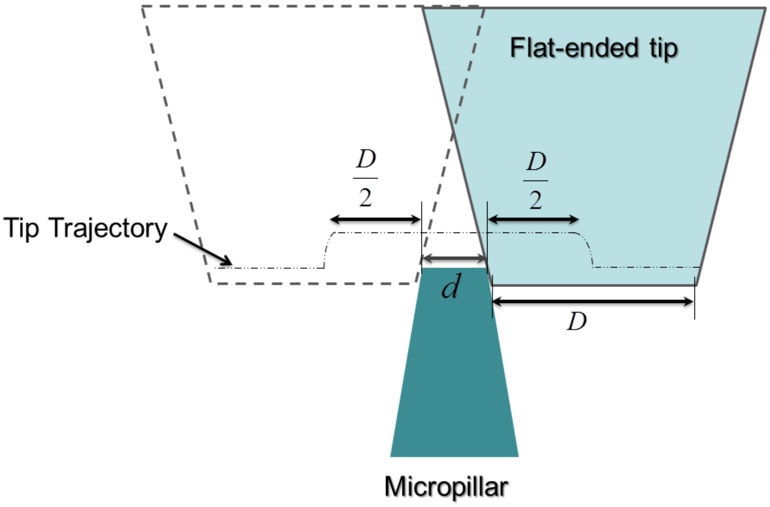

Figure 3.15.: Schematical view of the flat-ended tip and the micropillar during the imaging process.

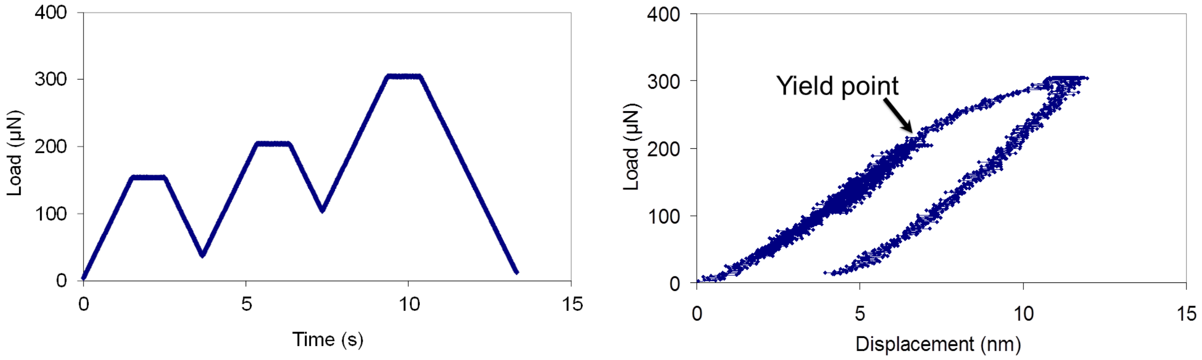

Figure 3.16.: (a) Cyclic load function applied to the pillars at the beginning of the compression test. (b) On the obtained load-displacement curve the yield point is indicated.

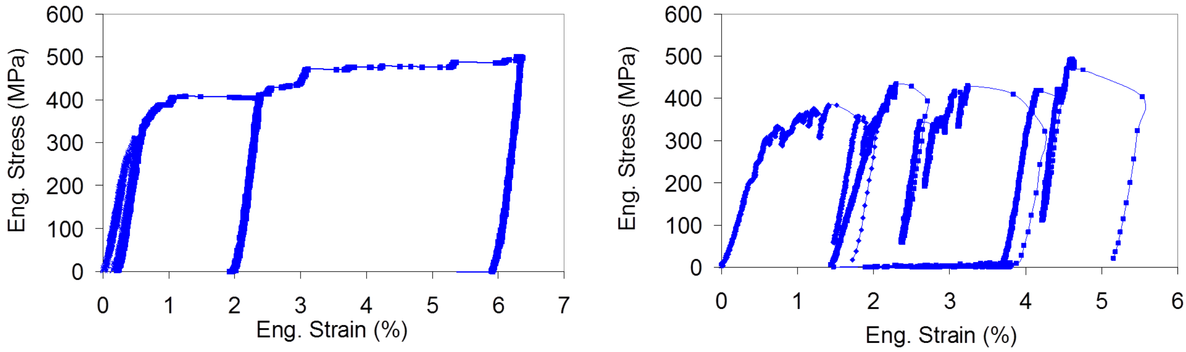

(a) Stress-strain curve obtained from the open-loop compression test.

(b) Stress-strain curve obtained from the displacement-controlled compression test.

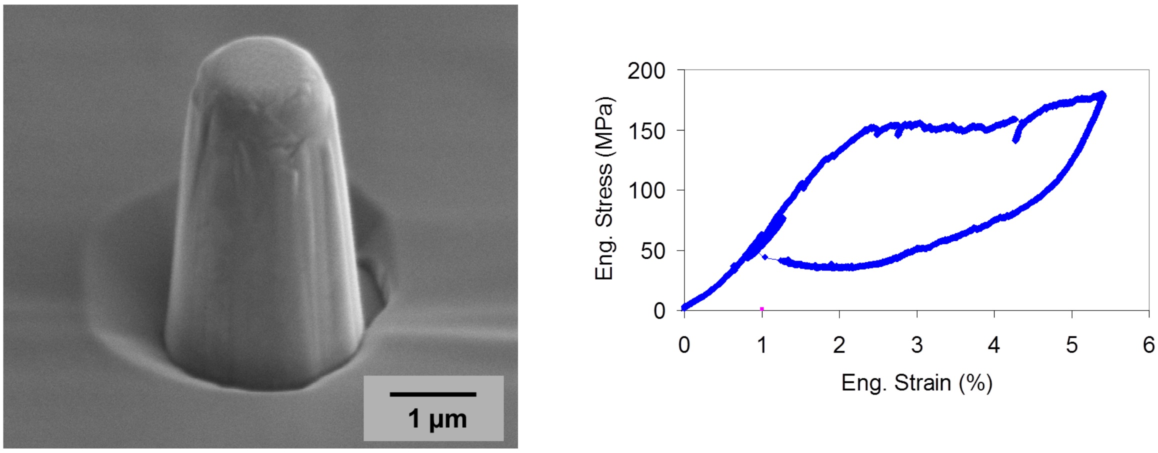

(c) A SE contrast SEM image of a shape memory alloy micropillar of CuZnAl.

(d) Hysteresis stress-strain curve of the shape memory alloy micropillar.

Figure 3.17.

3.4. Microstructural examinations

3.4.1. Micropillar microstructure

In order to study the effect of the grain boundary, the bicrystalline micropillars were compared to the single-crystalline micropillars not only by micromechanical tests, but also by performing microstructural tests. For this, a completely new microstructural characterization technique was used in this work. A film was cut out of the center of the single-crystalline micropillar (referred to as homogeneous medium) as well as the bicrystalline micropillars (referred to as inhomogeneous medium). In other words, the single-crystalline micropillars were used for calibration to observe the behavior of the lattice in the absence of the grain boundary. By characterizing the single-crystalline micropillars with single slip orientation, then with double slip orientation, and finally the bicrystalline micropillars, we tried to complicate the structures under study step by step as follows:

1. A homogeneous medium with easy glide behavior; i.e. a single-crystalline micropillar with single slip orientation as grain C in Table 3.6
2. A homogeneous medium with the presence of non-planar dislocations; i.e. a single-crystalline micropillar with double slip orientation as grain D in Table 3.6
3. An inhomogeneous medium with the presence of a grain boundary; i.e. a bicrystalline micropillar with single slip/multiple slip orientations as grains A/B in Table 3.6

The bicrystalline micropillars were cut parallel to the compression axis and normal to the grain boundary, while the single-crystalline micropillars were cut parallel to the slip direction. To investigate how the size of the micropillar influence the grain boundary effect, large and small bicrystalline micropillars were characterized. These films were finished by FIB in exactly the same way as the preparation of a TEM film, refraining from the last thinning step, since thicker films are required to obtain an EBSD pattern for the further analysis of the film by EBSD. The final thickness of the trimmed films is in the range of 100 nm. In order to protect the pillars from the redeposition of material and ion damage, prior to FIB cutting, they were coated with an amorphous Pt layer. In Figure 3.18 the preparation of a film out of an already deformed bicrystal is shown step by step.

The prepared films were examined in a high-resolution EDAX® OIM® system installed in a JEOL in-lens Schottky field emission cathode SEM. The EBSD measurements were performed by variable step sizes of 10 to 70 nm depending on the size of the micropillar and provided the local orientation of the microstructure.

It is also possible to *remill* the cut film and repeat the EBSD measurement on the new cross sections. In this way, a so-called "Ex-Situ Tomography" of the pillar is possible. However, this procedure is done by manually transferring the film from the FIB to the OIM system, which is an intensely time-consuming investigation method. Figure 3.19 shows the thick film, the SEM images from the two sides and the OIM maps.

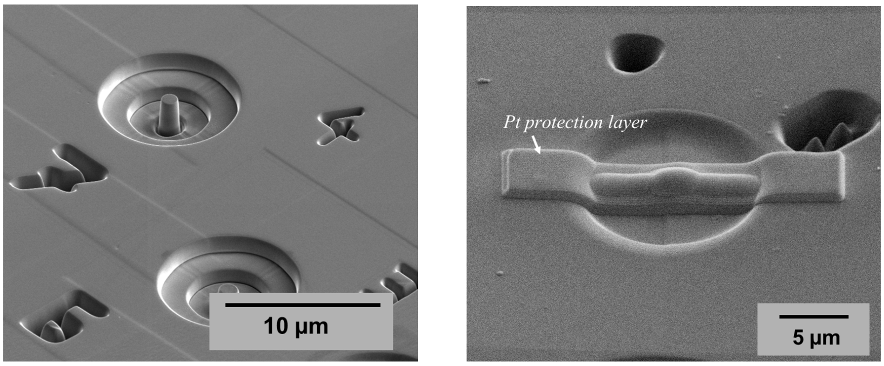

(a) Selection of a micropillar.

(b) The micropillar coated by Pt to protect it from the ion damage as well as the redeposition of material.

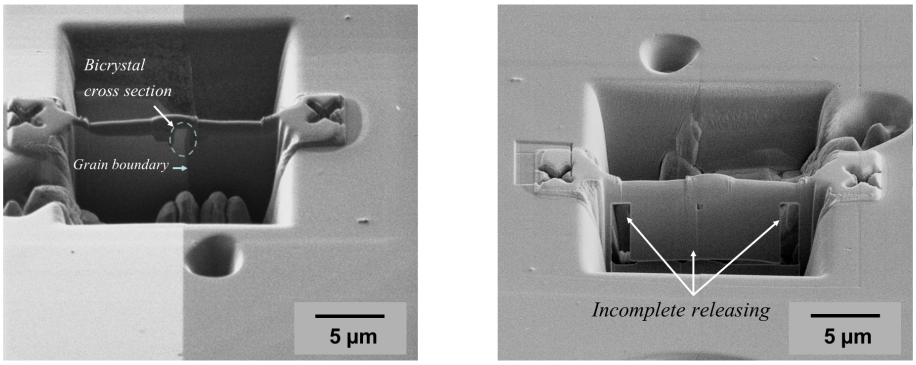

(c) Coarse milling of surrounding material. The bicrystal cross section is observable by orientation contrast.

(d) A pre-step to release the film from the bulk sample. The bottom and the two sides of the film are milled.

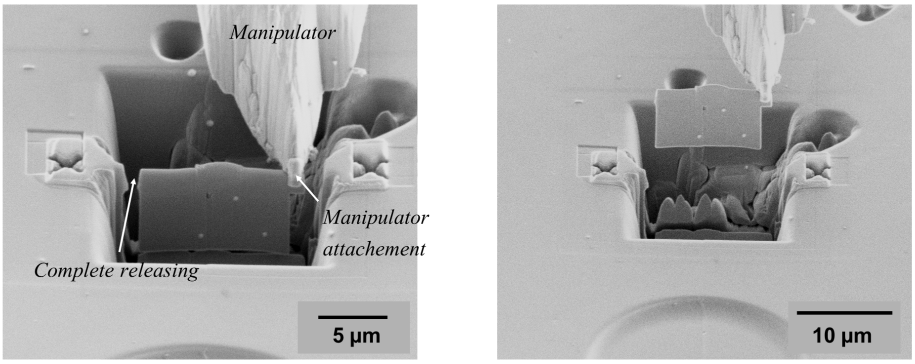

(e) First the manipulator is attached to the film on the right side and then the film is released from the left side. This sequence avoids the film falling down.

(f) The film, including the micropillar, is successfully lifted out.

Figure 3.18.: The film preparation out of a deformed bicrystalline micropillar.

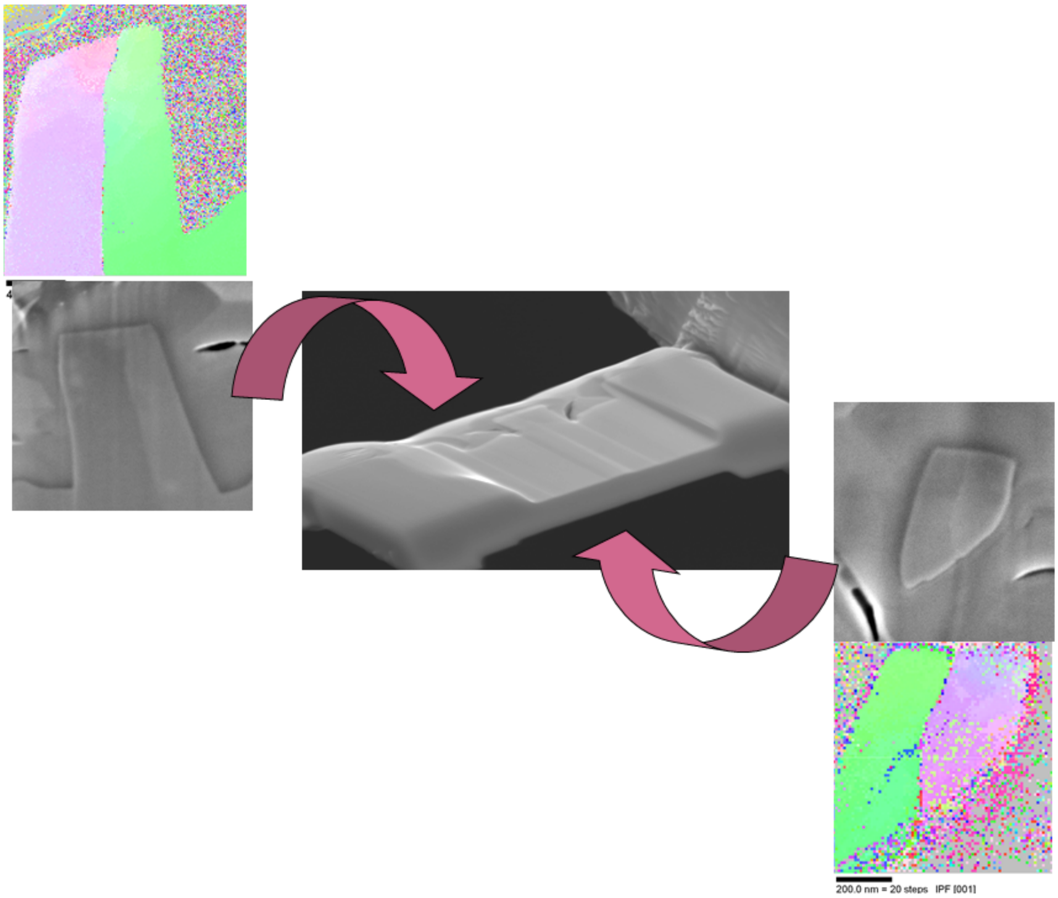

Figure 3.19.: SEM images and corresponding OIM maps of the two sides of a thick film cut out of a deformed bicrystal.

The OIM maps of the pillars cross sections were then analyzed by the following methods: Misorientation Mapping and Orientation Gradient Mapping (OGM). While the former method calculates the lattice misorientation with respect to one reference point defined by the user and gives the local lattice misorientation for each measured point, the OGM analysis determines the lattice misorientation with respect to the first neighbor points. In mathematical words, the OGM is the derivation of the Misorientation Mapping. In the OGM, a software developed in our institute by Dr. Ing. Mark Henning [*Henning and Vehoff*, 2005; *Henning*, 2007], for each measurement point the next neighbor in positive x-direction is determined. The relationship between two orientations can always be expressed by a rotation axis and a rotation angle necessary to rotate the first orientation into the second one (Appendix C). The absolute value of the rotation angle is referred here to as the orientation gradient in x-direction θ_x. The procedure to determine the gradient in y-direction θ_y is equivalent.

3.4.2. Micropillar free surface

The FIB-induced damage on the fabricated pillars is a well-discussed topic for many authors in addition to the observed size effect [*Bei et al.*, 2007, 2008; *Lee et al.*, 2011]. The ion beam interacts with the material, introduces defects and implants in the material. As a result, a damaged layer will be formed at the surface of the milled area (here, the micropillar free surface). We performed EBSD measurements not only to investigate the micropillar microstructure, but also to investigate this damaged layer at the fabricated micropillar free surface according to the fact that the lattice defects introduced by ion beam induce lattice rotation. To study the lattice rotation at the pillar free surface, ion damage in different levels was studied in the micropillars cross sections as listed below.

1. A micropillar fabricated by lithography and subsequent electrochemical etching without the use of an ion beam (Figure 3.20a).
2. A micropillar fabricated by a combination of lithography and FIB milling techniques (Figure 3.20b).
3. A micropillar fabricated only by FIB milling (Figure 3.20c).
4. A micropillar milled by ion beam with a perpendicular incident angle in FIB (Figure 3.20d).

As the information obtained from EBSD measurements is dependent on the step size used [*Field and Alankar*, 2011], the step size was chosen very carefully. It was attempted to use an optimal step size, since a low step size leads to long measurement times and thermal drift, and a large step size leads to information loss about the damaged area. A small area near the free surface was selected for measurement ($\leq 500\,nm \times 500\,nm$) and the step size was set to 5 nm. The scan time was approximately 15 to 20 min.

This EBSD investigation method was one out of three other methods, which were applied within the diploma thesis performed by Dipl. Ing. Christine Welsch [*Welsch*, 2011]. The other two methods to investigate the effect of FIB damage on the mechanical test results were nanoindentation and compression tests of micropillars fabricated by lithography (Litho-Pillars) compared to those fabricated by FIB (FIB-Pillars). The nanoindentation results are partly presented in Appendix D and the results of compression tests of Litho-Pillars compared to FIB-Pillars are presented in her diploma thesis [*Welsch*, 2011].

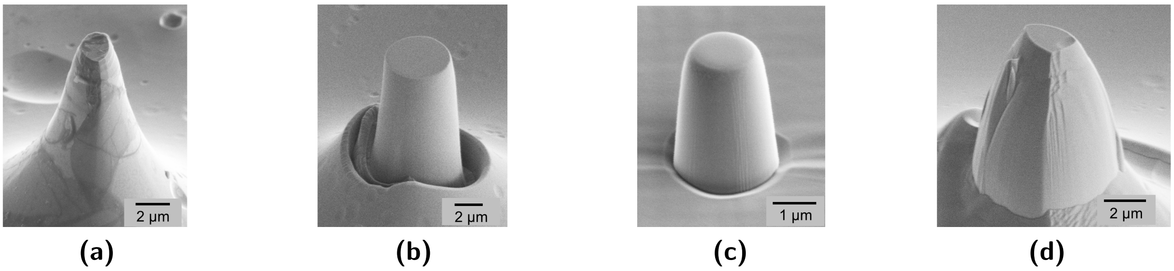

(a) **(b)** **(c)** **(d)**

Figure 3.20.: (a) A micropillar fabricated by lithography and subsequent electrochemical etching without the use of an ion beam. (b) A micropillar fabricated by a combination of lithography and FIB milling techniques. (c) A micropillar fabricated only by FIB milling. (d) A micropillar milled by ion beam with a perpendicular incident angle in FIB.

Chapter 4.

Molecular Dynamics Simulation

There is no doubt that experimental studies deliver more reasonable and faithful results than simulation and computational works. However, in the experimental world, we have to deal with the effect of a real situation, for instance, thermal drifts, machine compliance, insufficient resolution of microscopes, etc. With the help of simulation it is possible to remove such problems and investigate cases which are unachievable by experimental facilities.

Molecular Dynamics (MD) simulation, a method which directly simulates the true dynamics of atoms, can provide unique insights into the mechanistic and quantitative aspects of dislocation mobility. As we aim to study the interaction of dislocations with the grain boundary, this simulation method is the best choice. In this study we took advantage of MD simulation to resolve the slip transmission across the grain boundary and to determine whether it is the responsible mechanism of yielding in bicrystals, as suggested by Livingstone and Chalmers [*Livingstone and Chalmers*, 1957]. This was not possible by SEM observations, since the resolution required to observe the slip lines on the bicrystalline micropillar surface was not attainable. On the other hand, the slip propagation on a potential slip system in the adjacent crystal can be shown more precisely thanks to the atomic scale of MD simulation. In comparison to experimental works, the size of the samples in MD simulation is very small. The samples contain between one million and four million atoms. This is an advantage for our study, since for a direct interaction of dislocations with the grain boundary, we need to minimize the interaction between dislocations. This can be achieved by drastically reducing the size of the bicrystals. Hence, such small dimensions, which can hardly be achieved experimentally, are feasible by MD simulations. The simulation of bicrystalline micropillars was performed in cooperation with Dr. Ing. Afrooz Barnoush of our institute. Bicrystals with the same crystallographic orientations as the experiments were generated by a software developed by Dr. Mao Wen[1]. Figure 4.1 shows a bicrystal containing one million atoms ($\approx 70\,\mathrm{nm}$ diameter), made by the developed software, before a compression test. This bicrystal was compressed using a flat-ended tip specially generated in the software for compression test of micropillars. The time step for all MD simulations is $1\,\mathrm{fs}$ ($10^{-15}\,\mathrm{s}$). In MD simulations, the time step is one of the crucial parameters that determine computational expense. Two criteria must be followed in choosing the value of

---

[1] From the school of Materials Science and Engineering, Shanghai Jiao Tong University, Shanghai 200240, China

the time step. First, the time step should be small enough so that the trajectory of each atom is realistic. Secondly, the time step should be large enough so that the simulation is efficient. The embedded atom method is based upon the effective medium theory, a simplified first-principles method for predicting the binding energy of an interstitial atom to a host (another atom, a molecule, or a solid).

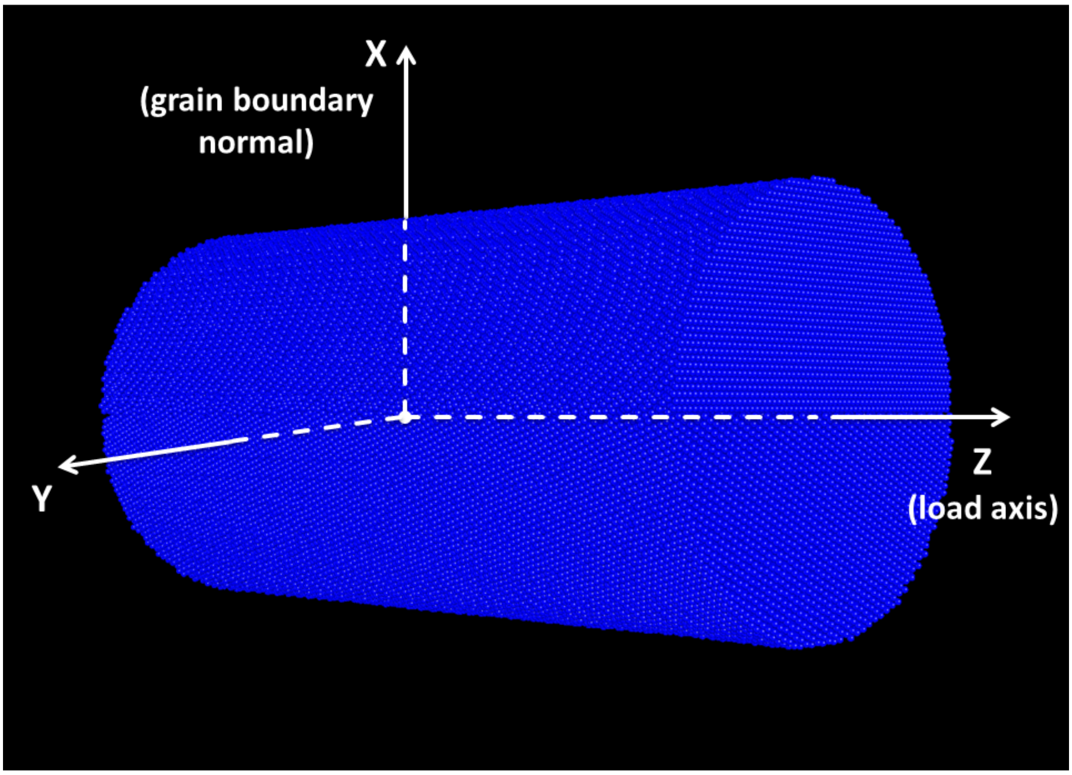

Figure 4.1.: The bicrystal generated in the MD software before deformation. The coordinate system will be used later for different observation views.

Chapter 5.

Results and Discussion

In this chapter, the results of the (i) micromechanical tests, (ii) MD simulation, and (iii) microstructural tests will be presented and discussed, separately. It will be shown that the results obtained from MD simulations are in agreement with the experimental results. A preliminary conclusion is given for the micromechanical tests data obtained by experiment and simulation.

5.1. Results of micromechanical tests

Compression tests of the pillars in the nanoindenter provide load-displacement curves, which were converted to engineering stress-strain curves according to Equations 5.1 and 5.2.

$$\sigma = \frac{F}{\pi(D/2)^2} \tag{5.1}$$

$$\epsilon = \Delta l / l_0 \tag{5.2}$$

where σ is the engineering stress, ϵ the engineering strain, F the applied load, D the micropillar diameter, Δl $(= l_0 - l)$ the displacement and l_0 and l are the micropillar height before and after the compression test, respectively. Due to the inevitable FIB-induced tapering of micropillars[1], the half-height diameter ($\bar{D}$) of the pillar was used to calculate the engineering stress for both single- and bicrystalline pillars (Figures 5.1a and 5.1b). As the bicrystals are non-isoaxial, as discussed in the experimental chapter (see section 3.1.2.1), the milling rates in adjacent grains differ due to the ion channeling effect. Therefore, in order to calculate the engineering strain, the average height ($\bar{H} = \frac{H_1+H_2}{2}$) was applied (Figure 5.1b). Δl and F are automatically registered by the nanoindenter during the compression test as *Displacement* and *Load*, respectively. In these experiments, it was observed that the difference between H_1 and H_2 in large and medium-sized pillars changes from 0.8 to 0.5 μm, and in small pillars this value is below 0.4 μm.

The micromechanical testing results will be presented in three main groups depending on the dimension of the pillars: micropillars with a diameter of 5 μm, referred to as *large*

---

[1] The effect of the tapered form of the micropillars on the stress distribution, compared to an ideal cylindrical micropillar, was investigated by Finite Element Simulation and is given in Appendix F.

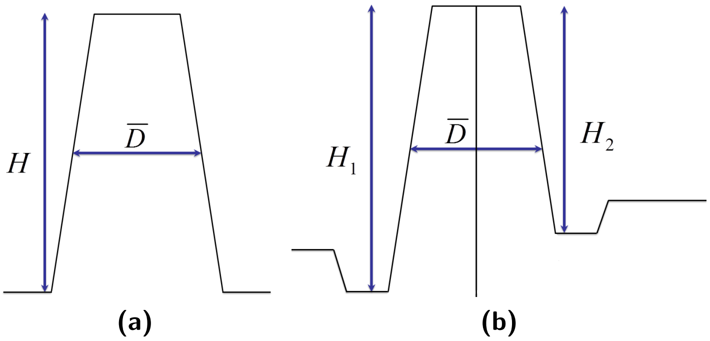

Figure 5.1.: Schematic profile of (a) single-crystalline and (b) bicrystalline micropillars displaying the average diameter and height used for calculations.

pillars; pillars with a diameter of 3 to 2 μm referred to as *medium pillars*; and pillars with diameters of 1.5 to 1 μm, referred to as *small pillars*.

5.1.1. Large pillars

The results of compression tests as well as the SEM images of bicrystals and single crystals of 5 μm diameter are presented here. Stress-strain curves of bicrystals (Figure 5.2a) show more and larger load drops[2] in the first stages of plastic deformation (below 4 %strain) than in strains over 4 %. The same behavior is observed in the stress-strain curves of single crystals with ($\overline{6}$ 5 5) orientation (Figure 5.2b) limited to strains of 3 %. The flow curves of single crystals with (1 5 3) orientation are performed under load control, therefore instead of load drops, strain bursts result (Figure 5.2c). The yield stress of bicrystals varies in the range of 62 to 160 MPa, while for single crystals with multiple slip orientation it is 118 to 130 MPa, and with single slip orientation it is 75 to 97 MPa. For a better comparison, Table 5.1 displays the standard deviation of these values from the average rate. Flow curves of bicrystals and single crystals with ($\overline{6}$ 5 5) orientation show strain hardening in contrast to single crystals with (1 5 3) orientation, i.e. easy slip orientation.

After the compression test, the pillars were imaged in SEM with secondary electron (SE) contrast in order to analyze the slip lines and determine the activated slip systems. Typical micrographs of the bicrystalline and single-crystalline micropillars after the compression test are shown in Figure 5.3. The crystallographic orientations of the adjacent grains of the bicrystalline pillar are marked on the figure. In Figure 5.3a one slip system is activated in the component crystal with single slip orientation and two slip systems are activated in the other crystal. In Figure 5.3b, however, two slip systems are resolved in each component crystal (with single slip and multiple slip orientations), i.e. a sum of four slip systems. In this latter bicrystalline pillar, the grain boundary is identical to the one shown in Figure 5.3a in terms of crystallographic orientation of adjacent grains. However, the misorientation angle of the grains relative to each other is 15 ° different. Nevertheless, the deformation mechanism and the required load for this size were not affected by this difference.

Table 5.1.: Yield stresses of bicrystalline and single-crystalline micropillars of 5 μm diameter.

Type of pillar	Average yield stress ± Standard deviation (MPa)
Bicrystal	122 ± 43
Single crystal (multiple slip)	123 ± 6
Single crystal (single slip)	81 ± 9

---

[2] The appearance of the load drops is explained in section 3.3.2.

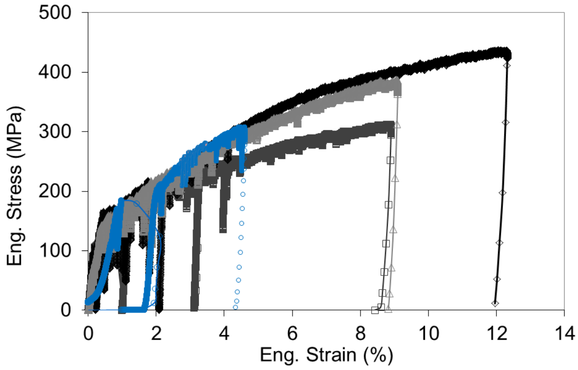

(a) Bicrystals, 5±0.08 μm

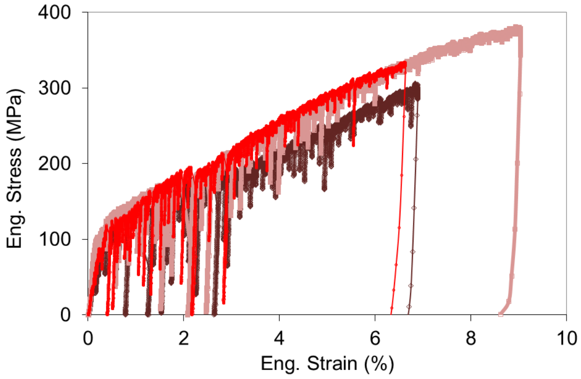

(b) Single crystals, multiple slip, 5.2±0.05 μm

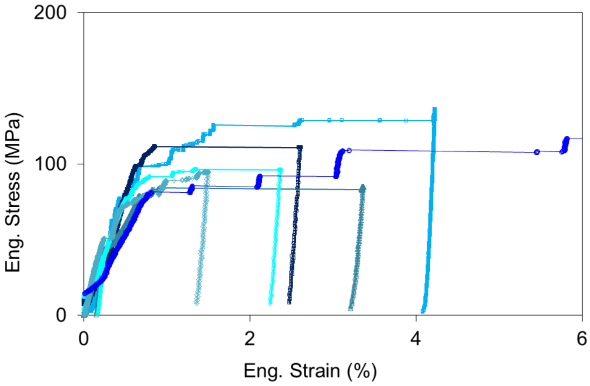

(c) Single crystals, single slip, 5.2±0.5 μm

Figure 5.2.: Engineering stress-strain curves of bicrystals and single crystals of the same diameters (5 μm). The size range of micropillars is presented by the average diameter ± standard deviation.

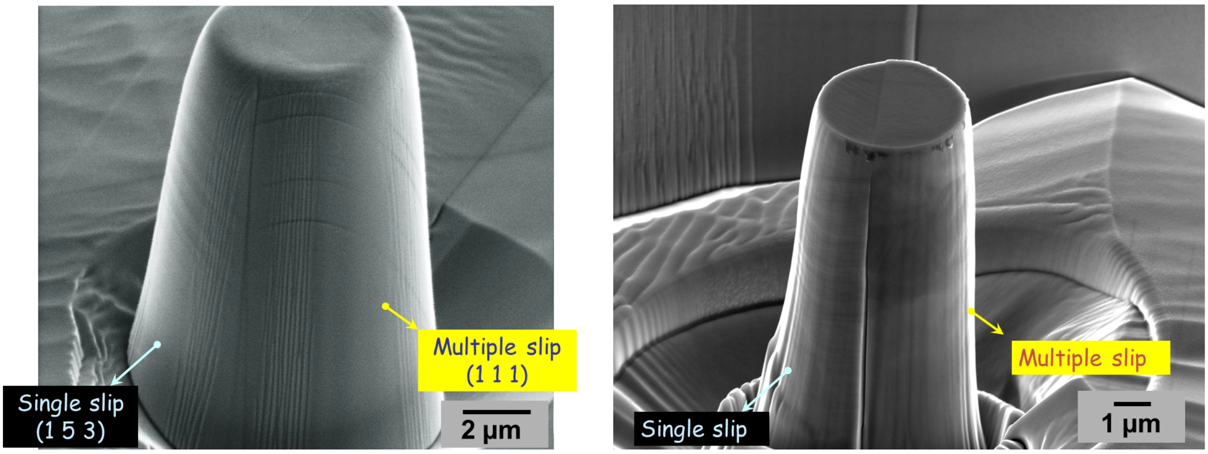

(a) Bicrystal, 5 μm **(b)** Bicrystal, 5 μm

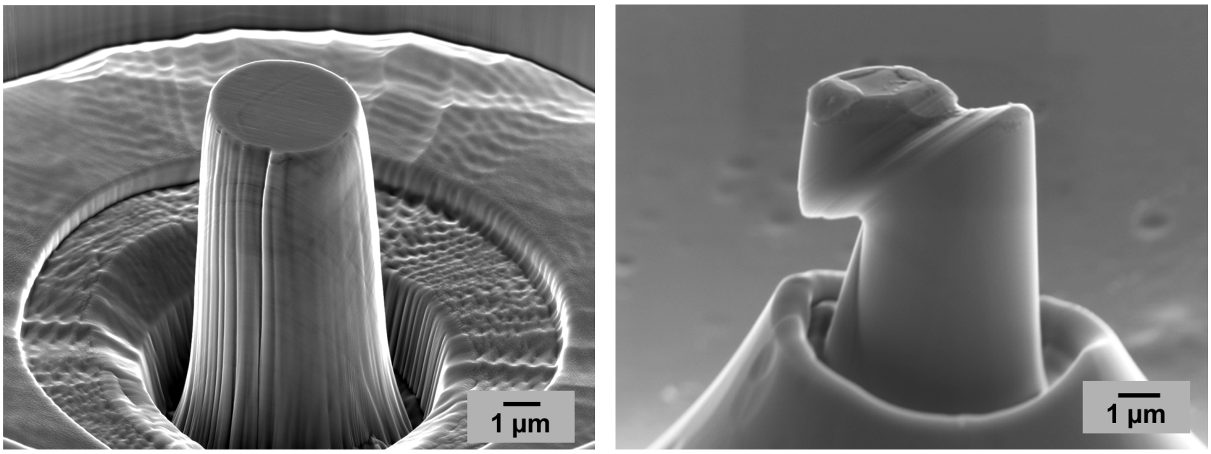

(c) Single crystal, multiple slip, 5 μm **(d)** Single crystal, multiple slip, 4.5 μm

Figure 5.3.: SE contrast SEM images of bicrystals and the single crystals of the same diameters (5 μm) after compression tests.

5.1.2. Medium pillars

Bicrystalline and single-crystalline micropillars with diameters between 2 and 3 μm are grouped in the medium size range. Flow stress curves of bicrystals with a 3 μm diameter are shown in Figure 5.4a and those of bicrystals with a 2 μm diameter are in Figure 5.4b. The compression tests of 3 μm diameter bicrystals are performed under load control feedback, while those of the bicrystals with 2 μm diameter are under displacement control. Therefore, in the latter case, load drops are observable. Flow curves of single crystals with multiple slip orientation and 2 to 3 μm diameters are performed under displacement control (Figures. 5.4c and 5.4d). In Figure 5.4d, two curves end with a drastic jump to higher strains. One curve, the pillar with a 2.5 μm diameter, shows a jump from 1.5 % to 4 % strain and the other pillar, with a 2 μm diameter, jumps from 3 % to 4 % strain. These instabilities in curves occur, when the pillar deformation rate increases abruptly and the flat punch tip follows this instability.

The curves of single crystals with single slip orientation and sizes between 2 to 3 μm are displayed in Figure 5.4e. One pillar, 3.4 μm in diameter, was tested under displacement control. It is important to notice that under load control mode, the loading rate depends on the material's behavior under the indenter. If the material deforms abruptly, the indenter follows the contact surface and thus drives on faster. Hence, a pop-in will result (see section 3.3.2); i.e. the loading rate will vary during the indentation. However, in displacement control mode, the indentation will be performed under a defined and constant loading rate. If the material deforms abruptly and the indenter becomes unstable, the feedback loop software tries to correct the loading rate and keeps it constant (if the feedback control is fast enough, which depends on the pre-defined PID values). This difference in the load control and displacement control feedback modes causes no complexity in terms of deformation loads, since nickel bicrystalline and single-crystalline micropillars show no strain rate sensitivity. We performed some tests for proof which are given in Appendix E.

The yield stress of bicrystals varies in the range of 120 to 232 MPa for a 3 μm diameter and 160 to 200 MPa for a 2 μm diameter. For single crystals with multiple slip orientation it is 108 to 150 MPa for a 3 μm diameter and 100 to 140 MPa for a 2 μm diameter. Single slip orientation single crystals show a yield stress of 95 to 220 MPa for a diameter range of 2 to 3 μm. In Table 5.2 the standard deviation of these values from the average yield stress are presented. Strain hardening is also observed here in bicrystals and single crystals with multiple slip orientation and not in single slip orientation micropillars.

A typical bicrystal in this size range is shown in Figure 5.5a. One activated slip system is detected in the left grain with (1 5 3) orientation, and 3 slip systems are detected in the right grain with ($\overline{6}$ 5 5) orientation. Deformed single-crystalline pillars with multiple slip orientations are shown in Figures 5.5b and 5.5c. In the 3 μm diameter pillars, two activated slip systems are observed (on the top surface in Figure 5.5b). It is possible that the third slip system has already been activated, but the resolution was not high enough to resolve this. Three slip systems can be observed in the 2 μm diameter pillar on its top surface (Figure 5.5c). These slip systems form a triangle on the pillar top surface, as predicted by the Thompson tetrahedron (Figure 5.6). In the pillar with (1 5 3) orientation, the activated single slip system is obvious in Figure 5.5d.

Table 5.2.: Yield stresses of bicrystalline and single-crystalline micropillars with diameter 3 to 2 μm

Type of pillar	Average yield stress ± Standard deviation (MPa)	
	3 μm	2 μm
Bicrystal	153±52	179±20
Single crystal (multiple slip)	121±14	139±35
Single crystal (single slip)	156±51	

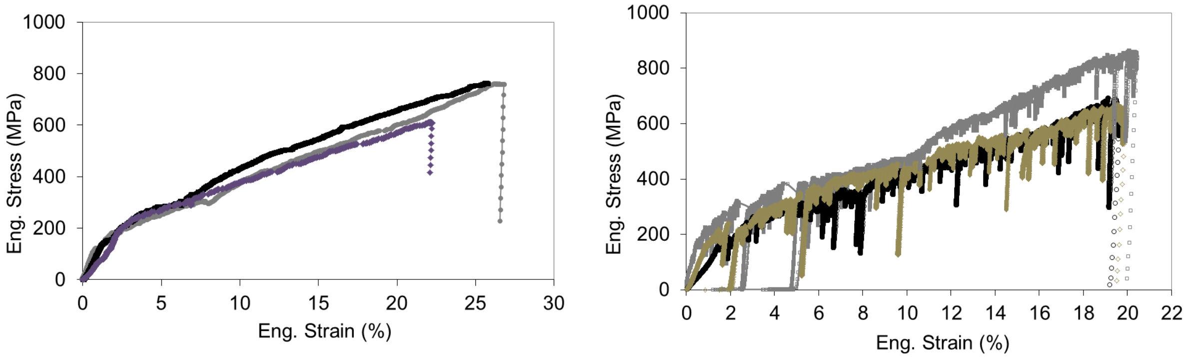

(a) Bicrystals, 2.8±0.2 μm

(b) Bicrystals, 1.8±0.2 μm

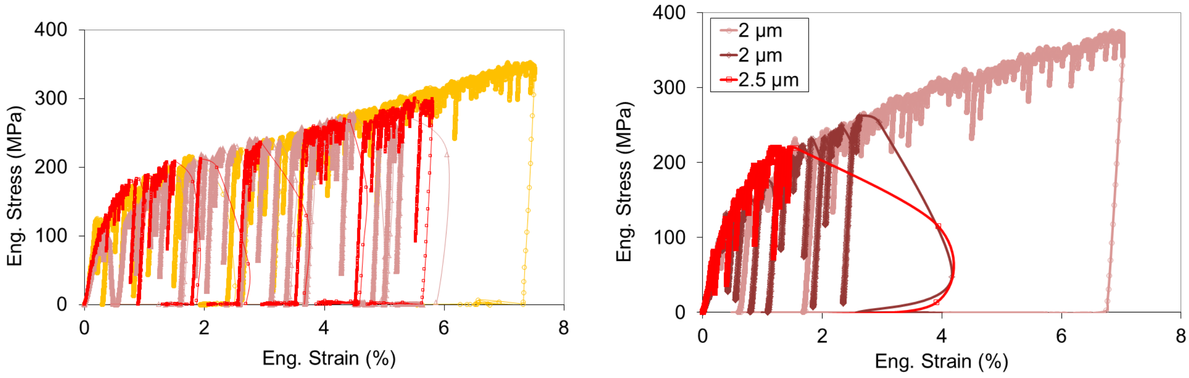

(c) Single crystal, multiple slip, 3.1±0.2 μm

(d) Single crystal, multiple slip, 2.2±0.2 μm

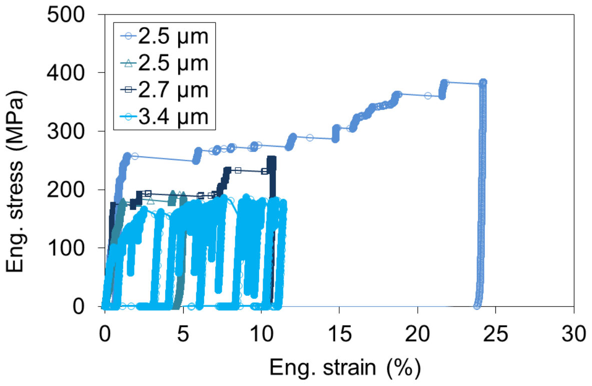

(e) Single crystal, single slip, 2.8±0.4 μm

Figure 5.4.: Engineering stress-strain curves of bicrystals and the single crystals of the same diameters (2 and 3 μm). The size range of micropillars is presented by the average diameter ± standard deviation.

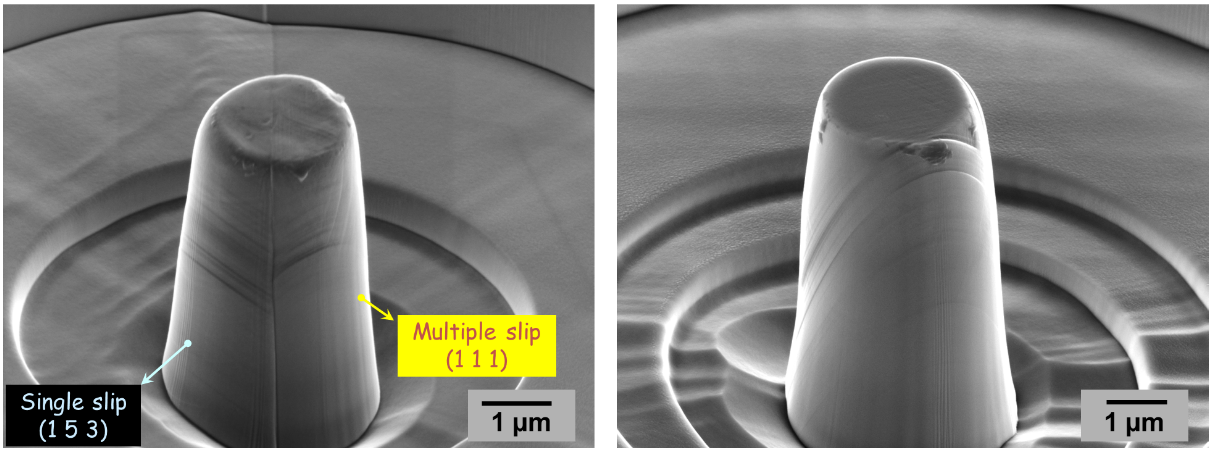

(a) Bicrystal, 3 μm

(b) Single crystal, multiple slip, 3 μm

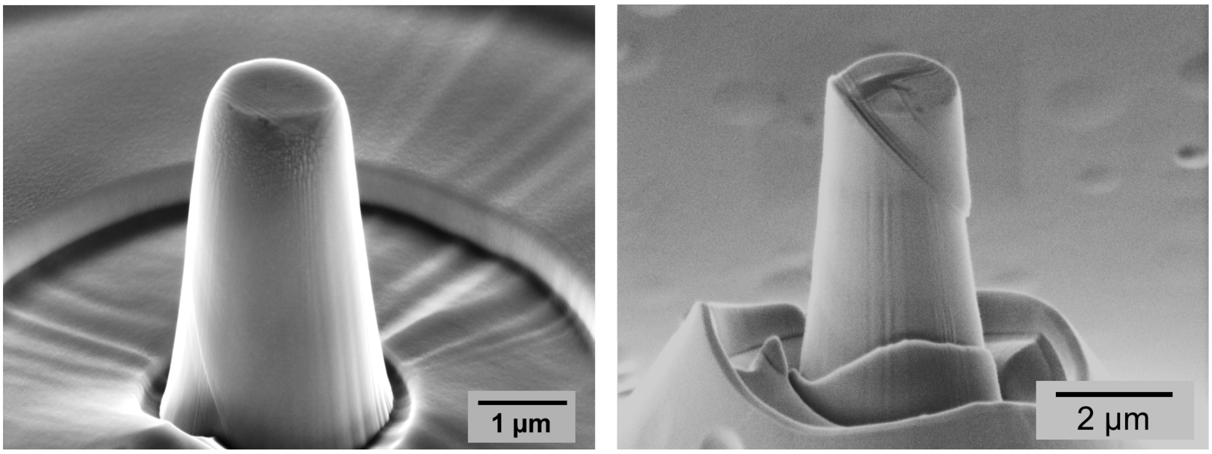

(c) Single crystal, multiple slip, 2 μm

(d) Single crystal, single slip, 2.5 μm

Figure 5.5.: SE contrast SEM images of a bicrystal and single crystals of the same range diameters (2 to 3 μm) after compression tests.

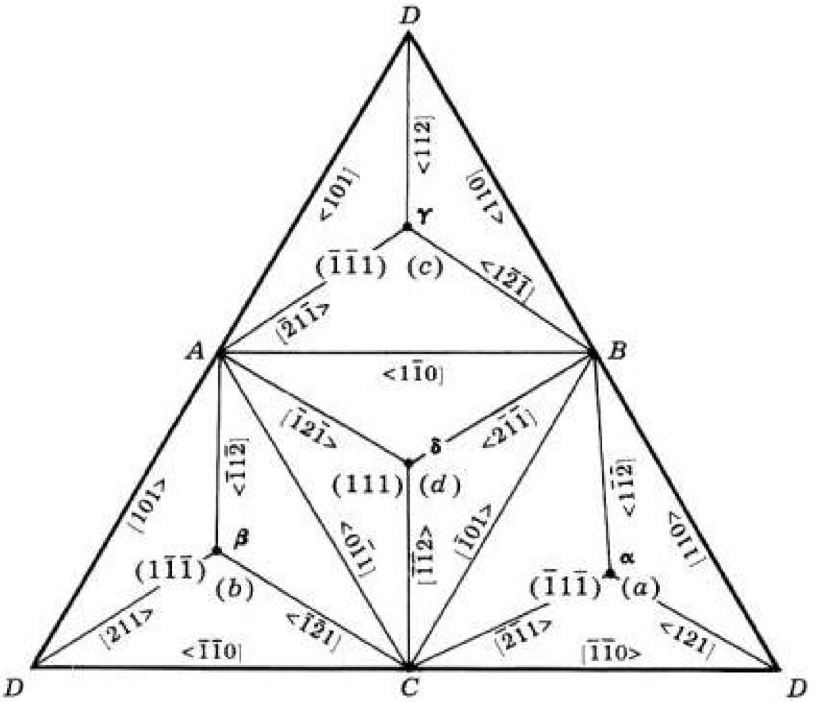

Figure 5.6.: Thompson tetrahedron

5.1.3. Small pillars

Pillars with diameters of 1.4 μm and 1 μm are grouped as small pillars. Flow stress curves of bicrystals with 1.4 μm diameter, are displayed in Figure 5.7a, in addition to those of the single-crystalline pillars with multiple slip orientation in Figure 5.7b and those of the single-crystalline pillars with single slip orientation in Figure 5.7c. From the curves it is seen that the compression tests of all these pillars are performed under displacement control mode. Pronounced strain hardening is observable in single-crystalline pillars with multiple slip orientation in comparison to bicrystalline pillars. Among the bicrystals, the strain hardening reduces from bicrystal 1 (BC1) to bicrystal 2 (BC2). These curves are marked on Figure 5.7a. Single slip orientation pillars continue to show no strain hardening. The yield stress of bicrystals varies in the range of 260 to 410 MPa, while for single crystals with multiple slip orientation this range is 180 to 300 MPa and with single slip orientation it is 165 to 225 MPa. In Table 5.3 the standard deviation of these values from the average yield stress are given.

SE contrast images of typical pillars of this size are given in Figure 5.8. In bicrystals, three activated slip systems are resolved in the left grain and one activated slip system in the right grain (Figures. 5.8a and 5.8b). Figure 5.8a belongs to the curve known as BC1 and Figure5.8b belongs to the curve known as BC2. In Figure 5.8a the grain boundary is bowed while in Figure5.8b it is crossed by slip transmission. Single crystals of the same diameter, with the respective orientations of the bicrystal's adjacent grains, are shown in Figure 5.8c and 5.8d. As expected, multiple slip (see the triangle formed on the pillar top surface in Figure 5.8c) and single slip (Figure 5.8d) were detected.

Table 5.3.: Yield stresses of bicrystalline and single-crystalline micropillars of 1.4 μm diameter

Type of pillar	Average yield stress ± Standard deviation (MPa)
Bicrystals	309±64
Single crystal (multiple slip)	250±57
Single crystal (single slip)	189±24

Engineering stress-strain curves of bicrystals with diameters of 1±0.1 μm are shown in Figure 5.9a. The curves show yield stresses from 160 to 474 MPa and increased work hardening with increasing strain. The curves of multiple slip orientation single crystals of the same size show quite different behaviors. For example, pillars 1 and 2 yield at ≈ 300 MPa, and pillars 3 and 4 at ≈ 200 MPa, i.e. in a range of 188 to 340 MPa. Strain hardening decreases from pillar 1 to 4. SEM images of these pillars shown in Figures 5.11a to 5.11d, explain this irregularity. Two activated slip systems are resolved in pillar 1, three systems in pillars 2 and 3 (see the triangle formed on the top surface of the pillars), and finally in pillar 4, where two activated systems are resolved, the deformation was continued on one favorable slip system. Comparing the curves with the SEM images shows that when deformation continues on all the activated slip systems, the interaction between these slip systems results in strain hardening as observed in the

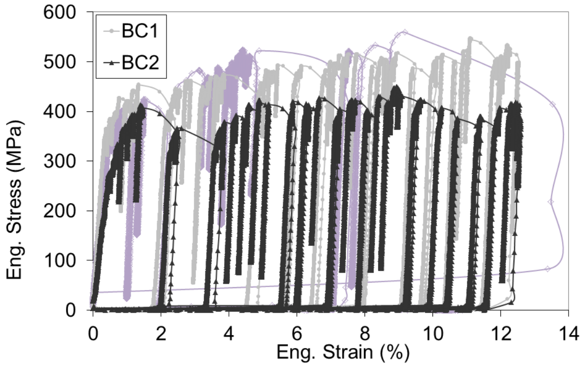

(a) Bicrystals, 1.4±0.04 μm

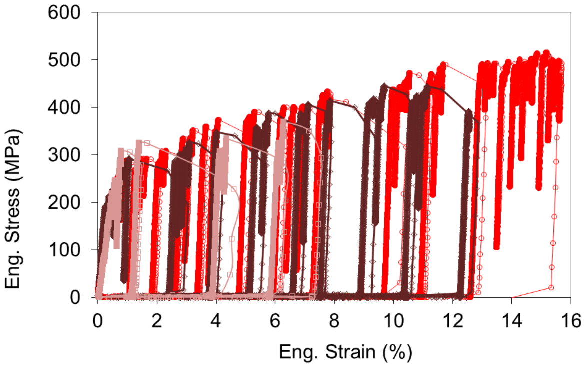

(b) Single crystal, multiple slip, 1.4±0.1 μm

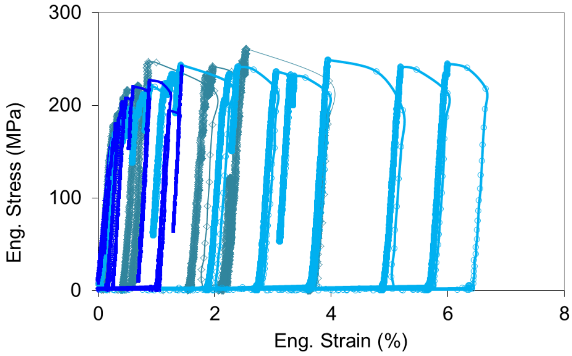

(c) Single crystal, single slip, 1.4±0.1 μm

Figure 5.7.: Engineering stress-strain curves of bicrystals and single crystals of the same diameters (1.4 μm). The size range of micropillars is presented by the average diameter ± standard deviation.

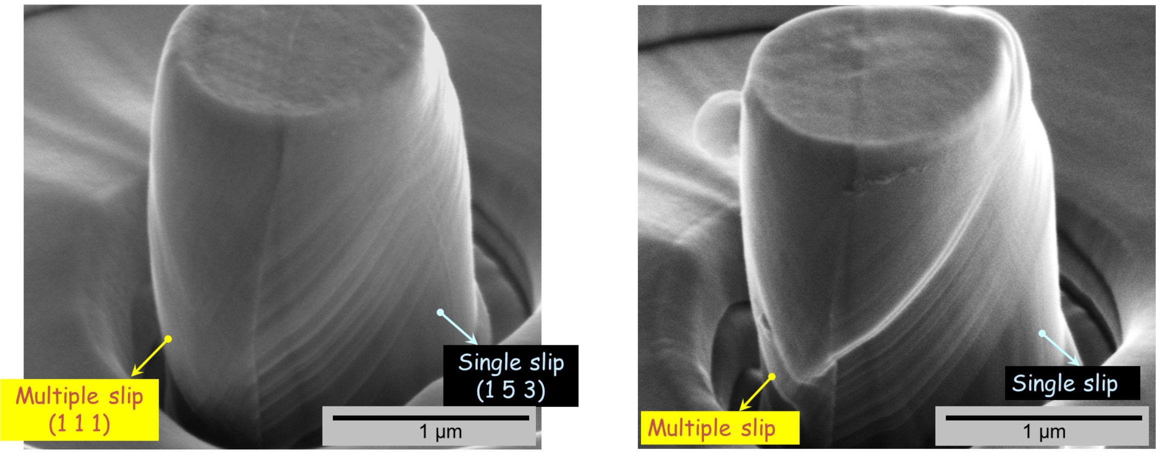

(a) Bicrystal 1 (BC1), 1.4 μm **(b)** Bicrystal 2 (BC2), 1.4 μm

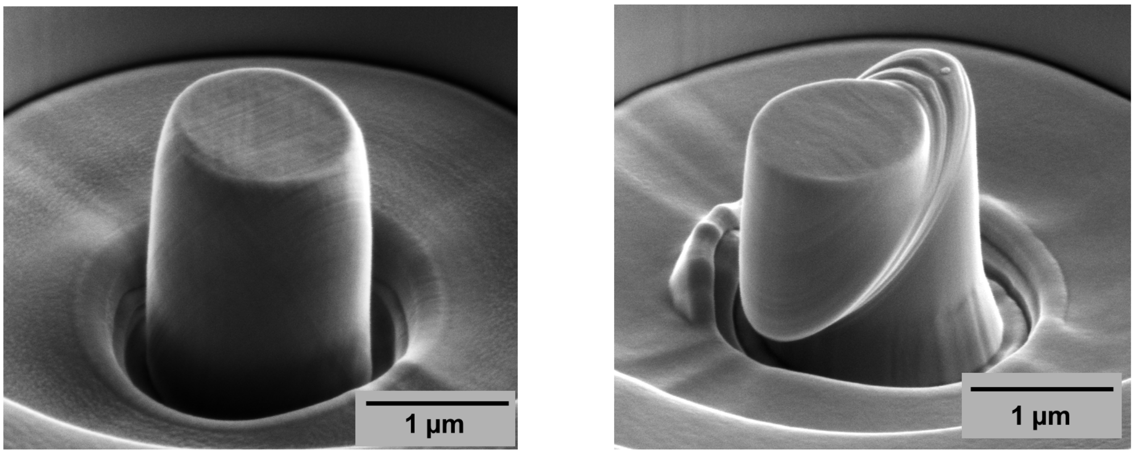

(c) Single crystal, multiple slip, 1.4 μm **(d)** Single crystal, single slip, 1.4 μm

Figure 5.8.: SE contrast SEM images of bicrystals and single crystals of the same diameters (1.4 μm) after compression tests.

curves of pillar 1 and 2 in Figure 5.11d. Once the deformation continues, preferably on one of the slip systems, the deformation occurs faster with no work hardening in the same manner as a single slip orientation as observed in the curve of pillar 4 in Figure 5.11d.

Flow curves of single slip orientation pillars are given in Figure 5.9c. The yield stress of these pillars changes between 130 and 250 MPa. After yield, the deformation on the single slip system caused no strain hardening in curves. Due to the small size of the pillars, they could only be compressed to small strains, since further straining caused the activation of the secondary slip system. The standard deviation from the average yield stress is given in Table 5.4.

Table 5.4.: Yield stresses of bicrystalline and single-crystalline micropillars of 1 μm diameter.

Type of pillar	Average yield stress ± Standard deviation (MPa)
Bicrystals	283±96
Single crystal (multiple slip)	266±68
Single crystal (single slip)	189±39

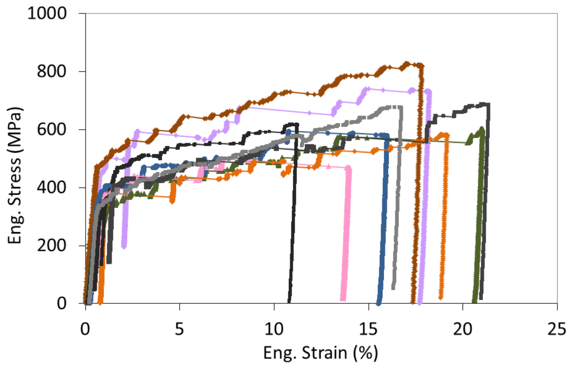

(a) Bicrystals, 1±0.1 μm

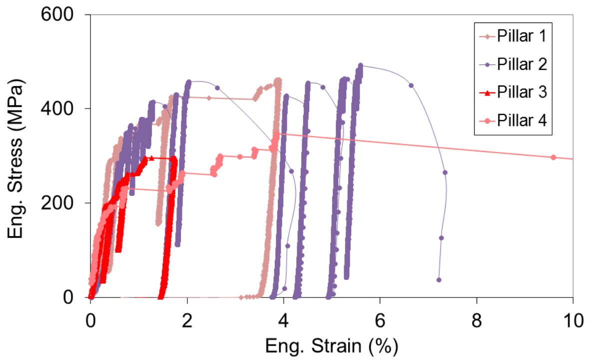

(b) Single crystal, multiple slip, 1±0.1 μm

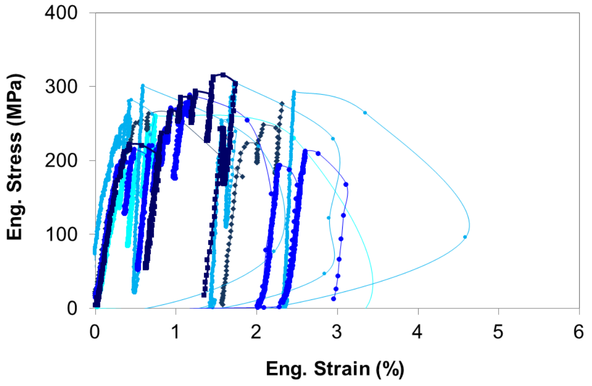

(c) Single crystal, single slip, 1±0.1 μm

Figure 5.9.: Engineering stress-strain curves of bicrystals and single crystals of the same diameters (1 μm). The size range of micropillars is presented by the average diameter ± standard deviation.

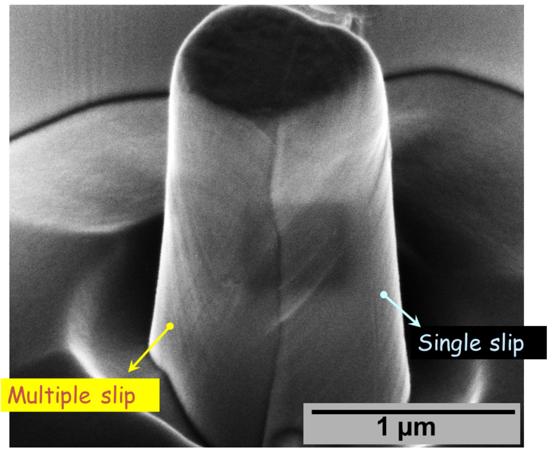

(a) Bicrystal (multiple slip/single slip), 1 μm

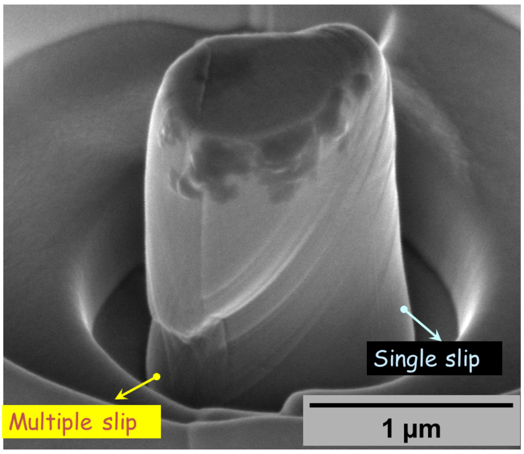

(b) Bicrystal, 1 μm

Figure 5.10.: SE contrast SEM images of bicrystals of the same diameters (1 μm) after compression tests.

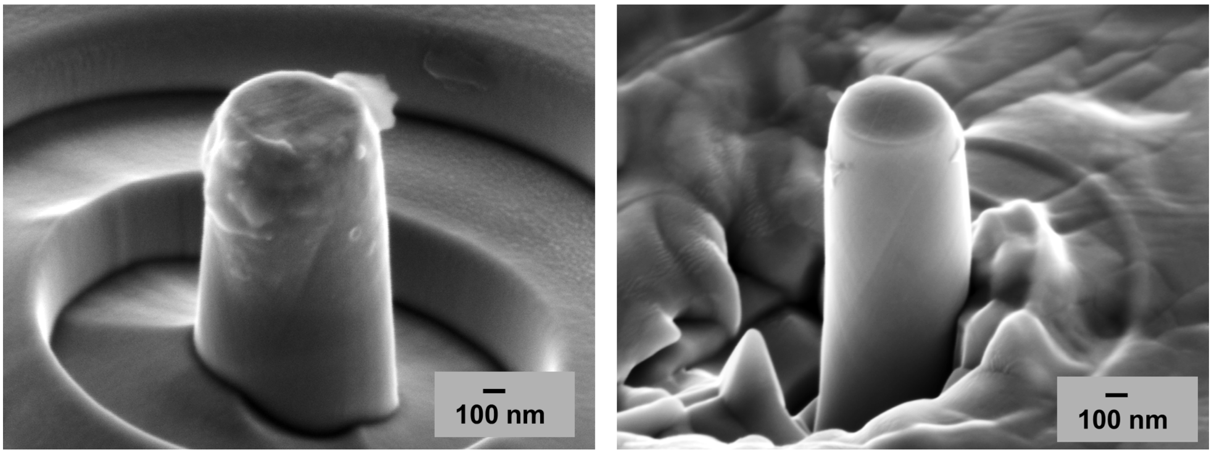

(a) Pillar 1, multiple slip, 1 μm

(b) Pillar 2, multiple slip, 1 μm

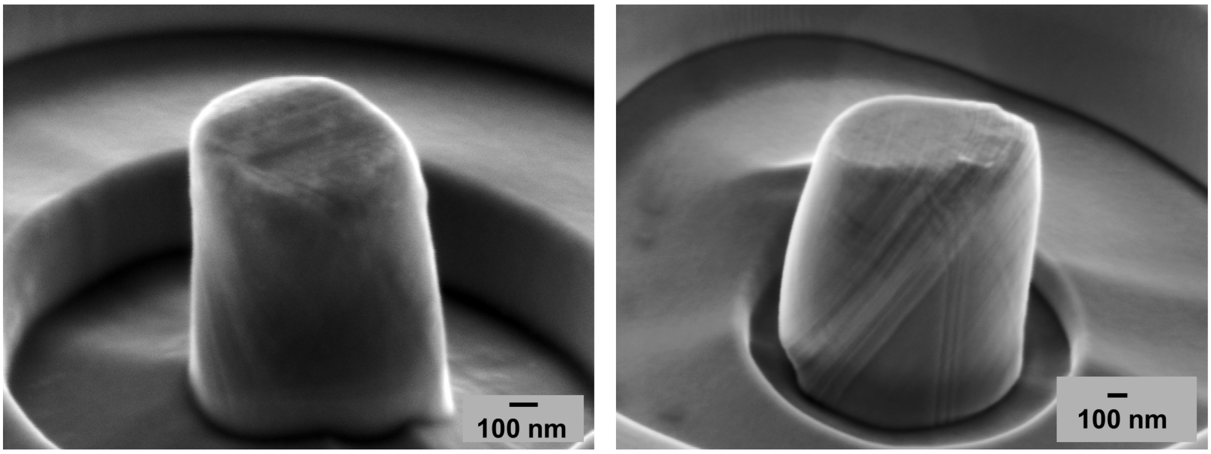

(c) Pillar 3, multiple slip, 1 μm

(d) Pillar 4, multiple slip, 1 μm

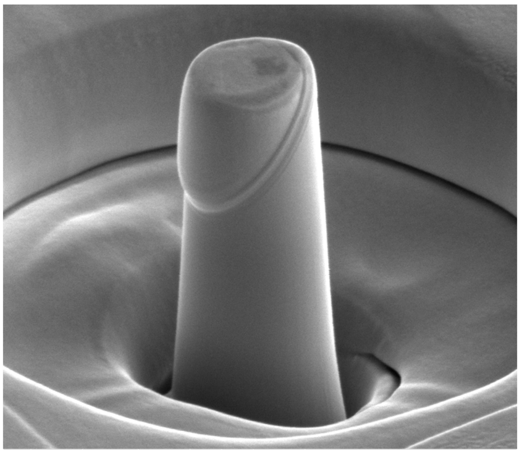

(e) Single crystal, single slip, 1 μm

Figure 5.11.: SE contrast SEM images of single crystals of the same diameters after compression tests.

5.2. Discussion of micromechanical test results

In this chapter, the results of the micromechanical tests presented in the previous section (section 5.1) will be discussed. For discussion, the computational and the experimental slip line analyses are compared. However, one may doubt the reliability of the results, since micropillars are made by FIB milling and the ion beam damage can affect the experimental results. In order to determine the effect of ion milling on the results, we investigated FIB-pillar surface microstructure, as explained in section 3.4.2. Therefore, prior to the discussion of the micromechanical test results, the results of the ion damage effect will be presented and discussed.

5.2.1. FIB damage effect

The results of high-resolution EBSD measurements at the free surface of micropillars (see section 3.4.2) with increasing damage level are shown as listed below. Since no useful information about the lattice rotation could be obtained from the OIM maps, OGM analysis was used further. It was observed, that at the surface of the micropillar the orientation gradient changes abruptly. These observations are in agreement with the theory of lattice rotation induced by ion beam introduced lattice defects.

1. **The Litho-Pillar fabricated with a ion beam damage level of zero** (Figures 5.12a and 5.12b). The OGM analysis shows that, on the free surface, there are some pixels indicating high misorientation gradients and in other areas there are no such pixels. As no FIB was applied in the fabrication of this micropillar, no damaged layer was expected to be observed. Therefore, pixels of high orientation gradients can be related to experimental errors during the fabrication of the Litho-Pillar such as introduction of contaminants during the electrochemical etching step.
2. **The FIB-Litho-Pillar** (Figures 5.12c and 5.12d). A continuous layer composed of pixels with high orientation gradients is observed on the surface of this pillar. This layer has an average thickness of 11 nm. The layer thickness was measured by counting the number of pixels with high orientation gradients in the direction of ion bombardment and multiplying by the step size (5 nm).
3. **The FIB-Pillar** (Figures 5.12e and 5.12f). The thickness of the damaged layer is similar to that of the FIB-Litho-Pillar in micropillars prepared only by FIB. This is 15 nm in average.
4. **The heavily bombarded micropillar** (Figures 5.12g and 5.12h). The maximum damaged layer thickness, observed in this micropillar, had an average thickness of 107 nm.

The layer thickness for each level of damage was measured and is listed in Table 5.5 in increasing order of damage from the Litho-Pillar to the FIB-Litho- and FIB-pillars, and finally to the heavily bombarded pillar. For FIB-Litho-Pillars and FIB-pillars, no

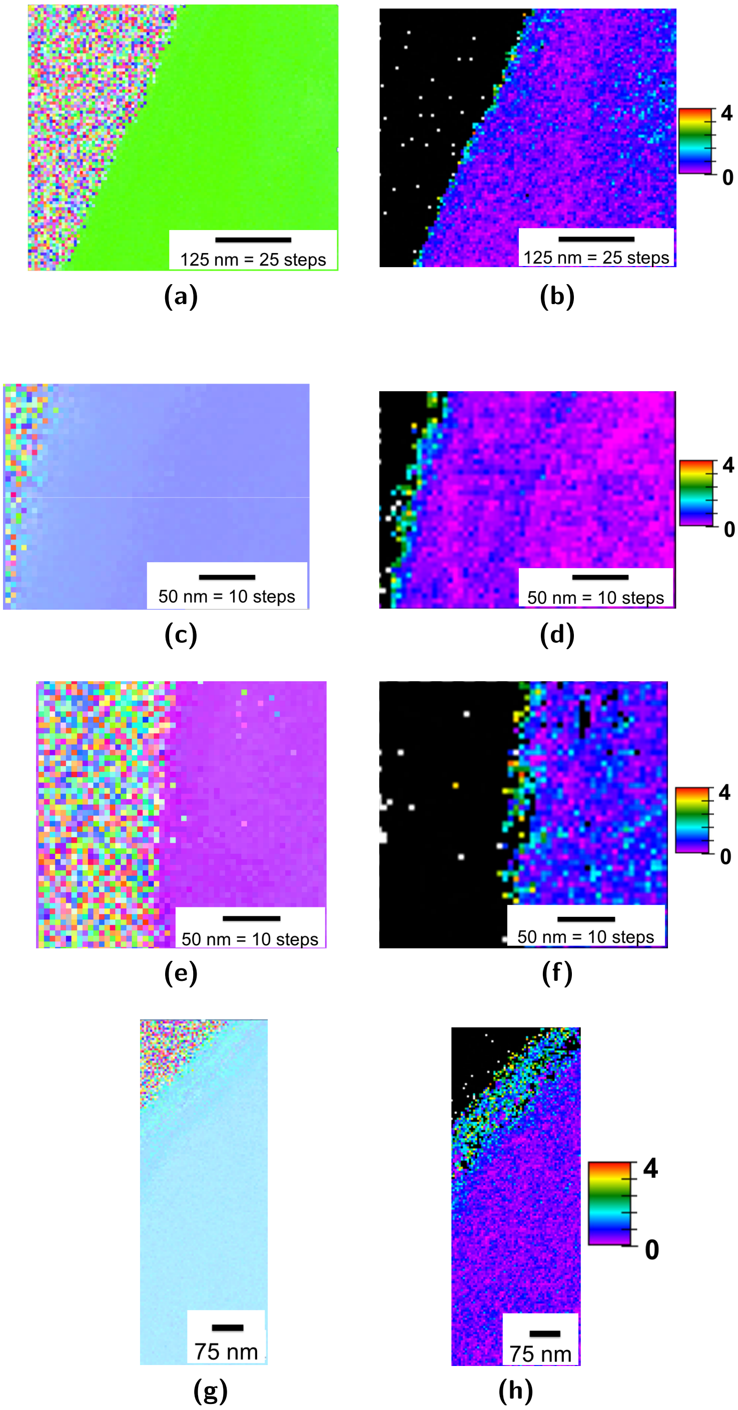

Figure 5.12.: (a) OIM map and (b) OGM analysis at the free surface of a Litho-Pillar prepared without ion damage. (c) OIM map and (d) OGM analysis at the free surface of a FIB-Litho-Pillar with ion damage. (e) OIM map and (f) OGM analysis at the free surface of a micropillar prepared by only fully FIB milling. (g) OIM map and (h) OGM analysis at the free surface of a micropillar heavily bombarded with the ion beam.

matter how the pre-form of the pillar is fabricated (by lithography and subsequent etching or by high-current FIB milling), the damaged layer thickness is similar. This can be explained by the fact that the low ion currents used for fine milling of FIB-pillars remove the damaged layer induced by higher currents used in the previous steps. This implies that the FIB-Litho-Pillars are similar to FIB-pillars in terms of the damage level at the surface. Hence, whatever the effect of ion beam on the mechanical properties of micropillars is, it exists for both of them. A more precise investigation on the mechanical properties of this layer was performed by nanoindentation of surfaces subjected to ion beam with different currents under variable load functions (Appendix D). That study showed that by increasing the ion beam current the damage level increases. The measured nanohardness showed that the hardness of this damaged layer is more than the material in electropolished condition. However, it is not a barrier for dislocations leaving the micropillars, since otherwise the slip lines would not be observable on the micropillar's free surface. However, it was also observed that the ion milling damage depends strongly on the crystallographic orientation of the material, i.e. for two different crystal orientations and a constant ion beam current, damage is higher in the crystal with an easy channeling orientation for ions.

Table 5.5.: The thickness of damaged layer on the free surface of the micropillars with different damage levels.

Damage level	Average value (nm)
Zero (Litho-Pillar)	6
Middle (FIB-Litho-Pillar)	11
Middle (FIB-Pillar)	15
High (heavily bombarded Litho-Pillar)	107

5.2.2. Stress-strain curve analysis

In the previous works on macroscopic bicrystals [*Chalmers*, 1937; *Aust and Chen*, 1954; *Hauser and Chalmers*, 1961] increasing the misorientation angle between the two component crystals resulted in increased incompatibility and, hence, higher stress concentration at the tip of the pile-up, causing higher yield and flow stresses (Figure 2.3). However, this was denied by Miura and Saeki [*Miura and Saeki*, 1978], as they observed no difference between the bicrystal and the single crystal stress-strain curves for any misorientation angle. From the above studies it can be concluded that the type of the grain boundary plays a crucial role in the determination of the deformation behavior. Each grain boundary should be handled individually, which shows the importance of studying bicrystals.

In this work we altered the size of the bicrystals, while the type of grain boundary remained unchanged. Variation of the size of the micropillars should change the flow stress for the same material. Lower stresses at the tip of the pile-up were achieved by decreasing the specimen size, since local stress at the pile-up depends on the number of dislocations in the pile-up (Equation 5.3), which is directly proportional to the grain size (Equation 5.4) [*Hirth and Lothe*, 1982]. Hence, higher extra loads are now required to overcome the grain boundary.

$$\frac{F}{L} = \tau N b \tag{5.3}$$

$$N = \frac{\tau(1-\nu)d}{\mu b} \tag{5.4}$$

$\frac{F}{L}$ is the force per unit length acting on the leading dislocation, τ the resolved external shear stress acting on dislocations in the pile-up, N the number of dislocations in the pile-up, b the Burgers vector, ν the Poisson ratio, d the length of the double ended pile-up (which can be simplified as the grain size) and μ the shear modulus. These equations are valid for edge dislocations. A pile-up of screw or mixed dislocations can be treated in the same way [*Hirth and Lothe*, 1982]. Equation 5.4 can be adjust for screw dislocations by replacing the factor $(1-\nu)$ by 1. Hence, by changing the bicrystalline pillar size, the dislocation pile-up stress for the same boundary can be varied. Bicrystals in the range of 1 to 5 μm were analyzed. To study the effect of the grain boundary on the strength of the material, the engineering stress-strain curves of bicrystalline micropillars were compared to those of the single-crystalline micropillars with the same size and the same crystallographic orientations as the adjacent grains of the bicrystal (Figure 5.13).

Within the studied size range, single crystals with single slip orientation have the highest Schmid factor of 0.48 (see Table 3.6) and therefore, the lowest yield stresses. In pillars with single slip orientation, since the dislocations can freely move to the surface and form pronounced slip steps, there is no work hardening. In contrast, the experiments with pillars oriented for multiple slip (near to (1 1 1)) demonstrate both higher yield stress and work hardening than single crystals with single slip orientation. According to the Thompson tetrahedron (Figure 5.6), three slip systems are expected to be activated simultaneously at the beginning of the yield. However, this crystal with a real orientation of (-5 6 6) is 5° away from the perfect (1 1 1) orientation. Two slip systems have similar Schmid factor values (0.35) and the third Schmid factor (0.24) is different but very close to the others. The activation of the two slip systems with Schmid factors of 0.35 will be energetically favorable, as observed in the case of single-crystalline micropillars with this orientation. These slip systems confine one another during the straining process and form different types of dislocation locks (Hirth locks, coplanar junctions, glissile and sessile junctions) [*Bassani*, 1990], resulting in strain hardening as observed in the curves.

Depending on their size, the bicrystals deform either with the same (Figures 5.13a and 5.13b) or higher (Figures 5.13c, 5.13d and 5.13e) flow stresses than the corresponding single crystals with multiple slip orientation. For the explanation, let us consider a constant dislocation source density in the bulk sample such that, decreasing the size of the pillars results in a decrease of dislocation source numbers (Figure 5.14). Hence, the small bicrystals (1.4 and 1 μm) deform by source-limited plasticity, diminishing dislocation-dislocation interaction, thereby increasing the probability of dislocation-grain boundary interaction. In the large and medium bicrystals, the large number

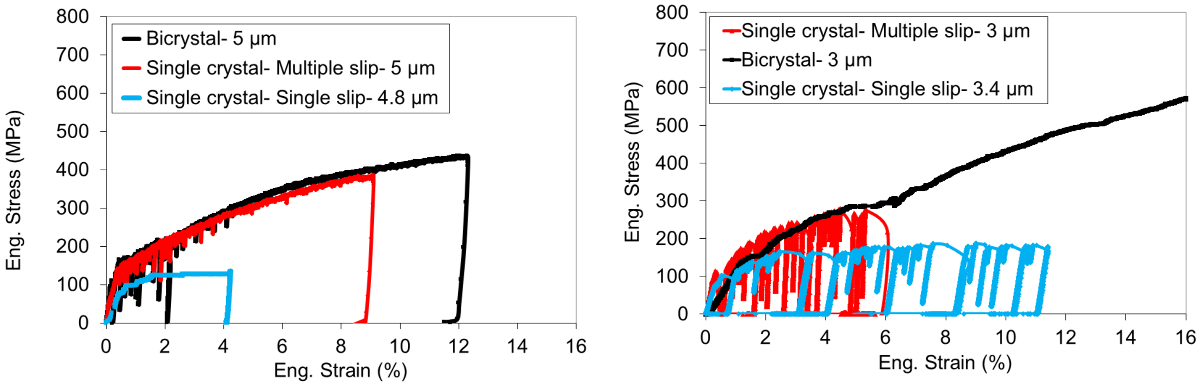

(a) 5 μm **(b)** 3 μm

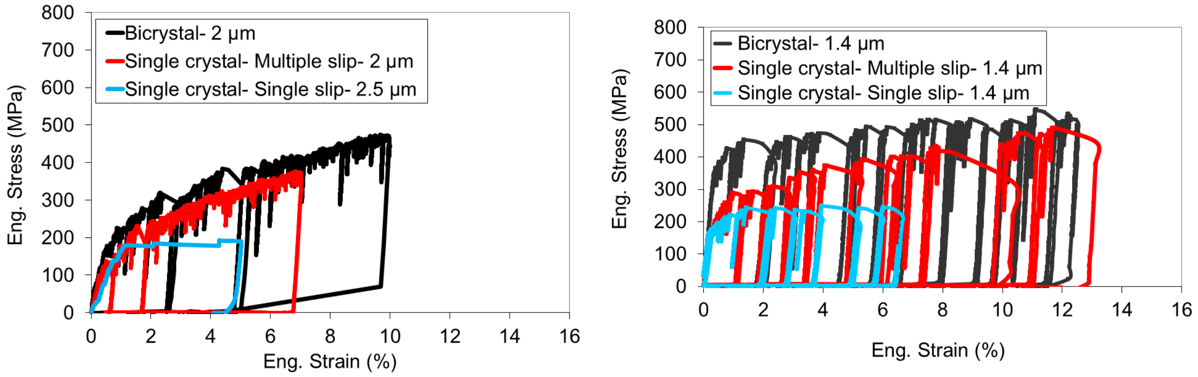

(c) 2 μm **(d)** 1.4 μm

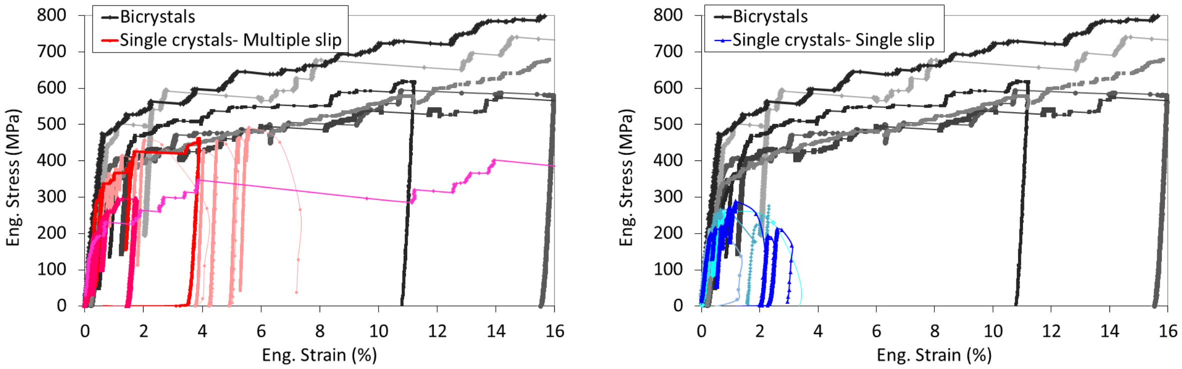

(e) 1 μm **(f)** 1 μm

Figure 5.13.: Engineering stress-strain curves of a bicrystals compared with the two corresponding single crystals for different specimen diameters.

of dislocation sources enhances dislocation-dislocation interaction. Thus, these deform like the two component single crystals connected in parallel, which implies that the strongest component is controlling the deformation behavior and, therefore, the flow stress of bicrystal should resemble that of the multiple slip single crystal. This was observed in bicrystals with diameters from 5 to 2 μm. The bicrystals with diameters of 2 μm show a small increase in the flow stress curves compared to the single crystal with multiple slip orientation. In 1.4 μm bicrystals the flow curves are well above those of the single crystals of both orientations. In the case of 1 μm pillars, the multiple slip orientation single crystals deform with variable stresses. The highest flow stress of these pillars lays on the lowest limit of the bicrystal flow curves. It seems that the strengthening effect of the grain boundary appears in the smaller dimensions.

5.2.3. Correlation between grain boundary effect and size

As previously mentioned, a periodic load function at the beginning of the compression test was used to precisely determine the yield stress of pillars (see section 3.3.2). However, variable yield stresses were detected for pillars of the same size. The stochastic dislocation distribution in the bulk sample causes variable number of dislocation sources in each pillar. This becomes pronounced by decreasing the size of the pillars, i.e. a small variation in the limited number of dislocation sources makes a big difference in the yield stress. On the other hand, the first pop-in (by load control mode) or the first load drop (by displacement control mode) may not always be the real plastic deformation onset, but rather the point at which a pinned dislocation line at the surface may be activated, exit the system thereby making it starved of dislocations. This is the famous “dislocation starvation” model to explain the size effect of single-crystalline micropillars [*Greer et al.*, 2005; *Greer and Nix*, 2006].

In addition, the parallelism of the flat-ended tip surface with the pillar surface plays an important role in the beginning of the deformation. When these surfaces have a small degree of declination, the data acquisition starts with the first contact of the flat punch

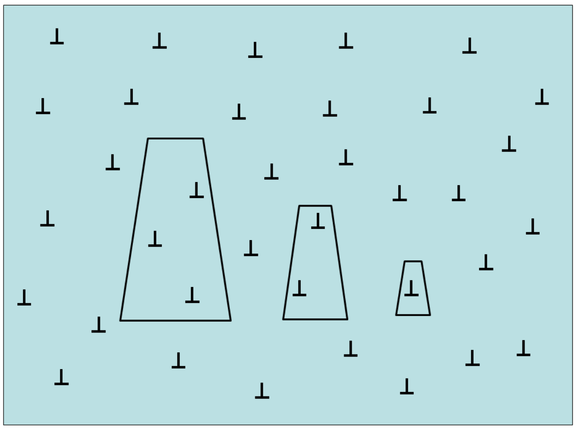

Figure 5.14.: Schematic drawing of the source distribution in specimens with different sizes.

with the declined sample surface. The inhomogeneous stress distribution, in addition to a high concentration of the load on the top of the pillar, leads to the squeezing of the pillar top area. As a result, the load-displacement curve at the beginning shows the behavior of a soft material. At the deformation onset, different mechanisms, such as loss of dislocations at the free surface by image forces [*Volkert and Lilleodden*, 2006] and/or dislocation multiplication, change the dislocation structure of the pillars and the deformation becomes stable. Therefore, same size pillars can yield at different stresses, while showing the same strain hardening stress. Therefore, one can talk about the yield stress size effect and strain hardening size effect. According to aforementioned problems, there is no clear criterion to determine the yield stress, although we tried to determine it by a periodic loading function at the beginning (see chapter 3.3.2). Hence, we compared the pillars by flow stresses at 0.5 % strain ($\sigma_{0.5\,\%}$) for a better explanation of the grain boundary effect (Figure 5.15). These stresses were measured in single crystals by considering the elastic anisotropic property of nickel and different elastic moduli of pillar crystallographic orientations, and excluding the elastic strain part; i.e. a line was drawn with the x-axis (strain axis) intercept of 0.5 %. The slope of the line was the elastic modulus given for that orientation. For bicrystals, the average of the elastic moduli of the two component crystals (assumed as a parallel system) was used for the slope. The figure (Figure 5.15) indicates the flow stress at 0.5 % strain for pillar diameters 5, 3, 2, 1.4 and 1 μm. Single crytsals of both orientations as well as the bicrystals show an increase in the average flow stress by decreasing the pillar size. For each individual size group the bicrystals are compared to the single crystals with the same orientation as the bicrystal adjacent grains. Bicrystalline micropillar sizes of 5 μm, 3 μm and 2 μm show no huge difference to the single-crystalline pillars with multiple slip orientations. This difference is more pronounced in pillar sizes of 1.4 μm and 1 μm. The higher flow stresses of bicrytsals in this size range are explanined by the dominance of dislocations-grain boundary interactions rather than dislocation-dislocation interactions. A high scatter is observed in single crystals with multiple slip orientation and 1 μm in diameter, which is explained in section 5.1.3.

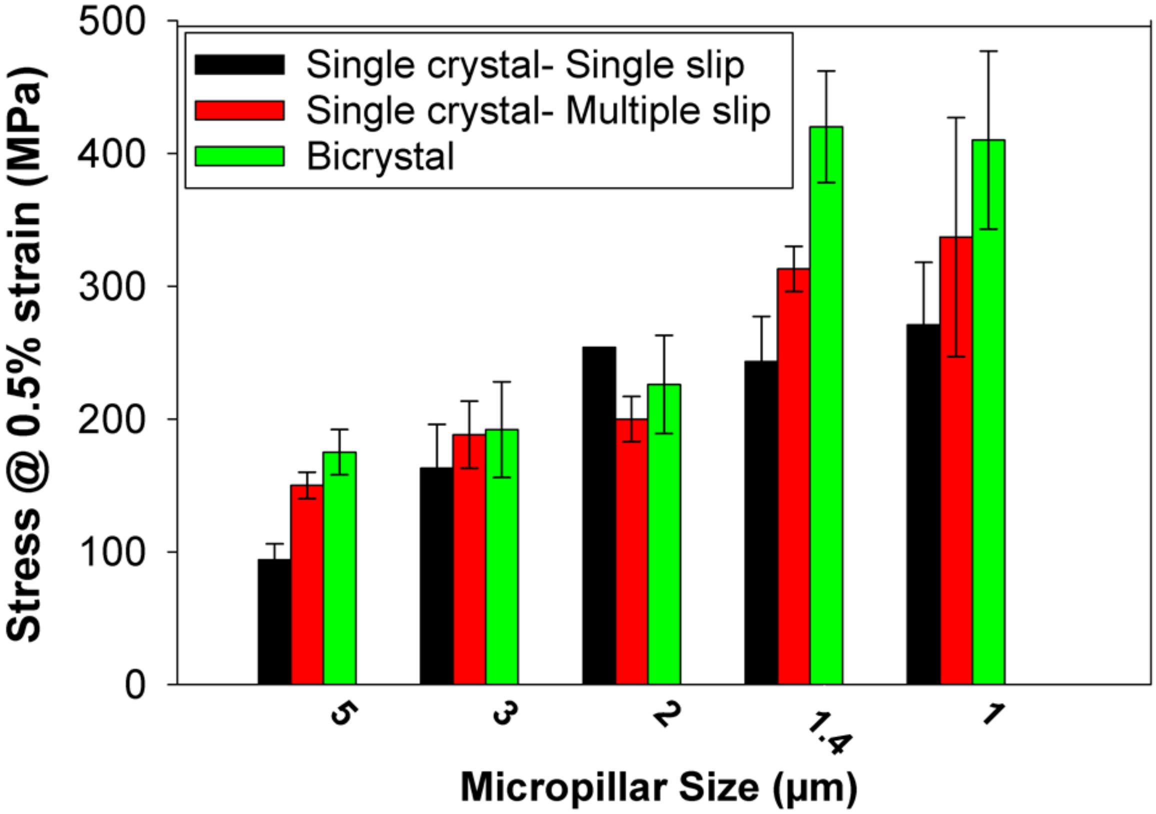

Figure 5.15.: Stress at 0.5 % strain vs. pillar diameter. In each size group the bicrystal deformation is compared with single crystals of the same size and the same orientation as the component crystals.

5.2.4. Slip line analysis

With the knowledge of the crystallographic orientations $(h\ k\ l)\ \langle u\ v\ w\rangle$ of the component crystals, the potential slip systems and the grain boundary normal can be calculated for each component crystal. By application of geometric rules, it is possible to determine the activated slip systems in individual component crystals. On the other hand, examination of such miniaturized bicrystalline micropillars provides observation of the slip lines both on the pillar top surface and on the lateral surface. Hence, a perfect comparison between the computational prediction and the experimentally observed slip systems is possible. The prediction of the activated slip system is simple in the component crystal with single slip orientation, since the slip system with the highest Schmid factor is supposed to be activated, as given in Table 5.6. However, this is more complicated in the component crystal with multiple slip orientation, since there are three possible slip systems to be activated. The activated slip systems were precisely determined by calculating the angles between the intersection lines of the slip planes and the grain boundary line on the pillar top surface, by considering the Thompson tetrahedron and by comparing with SEM observations. These angles are referred to as angle α_i and the subscript i determines the number of the activated slip system (as in Figure 5.16c). The same calculations were applied to determine the angles between the intersection lines of the slip planes between each other on the grain boundary plane, in order to predict the potential slip system on which the slip transmission occurs. These angles are referred to as angle θ_i and the subscript i determines the number of the activated slip system (as in Figure 5.16b). θ_1 is not seen on the figure, since it refers to the angle between the slip system number 1 with itself, which is zero. These information are summarized in Table 5.6. The intersection lines were calculated according to Equations 5.5 and 5.6.

$$\vec{L}_i(\text{on the top surface}) = \vec{n}_{\text{slip plane}} \times \vec{n}_{\text{top surface}} \tag{5.5}$$

$$\vec{L}'_i(\text{on the grain boundary plane}) = \vec{n}_{\text{slip plane}} \times \vec{n}_{\text{grain boundary}} \tag{5.6}$$

$\vec{L}_i$ is the intersection line of the slip plane with the pillar top surface, $\vec{L}'_i$ the intersection line of the slip plane with the grain boundary plane, i the number of the activated slip systems, $\vec{n}_{\text{slip plane}}$ the slip plane normal, $\vec{n}_{\text{top surface}}$ the bicrystal top surface normal, which is identical to $(h\ k\ l)$, and $\vec{n}_{\text{grain boundary}}$ the grain boundary normal.

The characterized slip systems are displayed schematically in Figure 5.16 in comparison to an experimentally deformed bicrystal. The schemes are drawn from two different views: from the top and from the lateral view of the pillar. The top view contains the intersection lines of the slip planes and the grain boundary with the pillar top surface (Figure 5.16c) and the lateral view shows the intersection lines of the slip planes with the grain boundary plane (Figure 5.16b). As supposed by [*Clark et al.*, 1992] the slip transmission occurs on the slip system with the minimum angle between the incoming and the potential outgoing slip plane. According to our calculations, the incoming slip plane in grain A has a minimum angle of 18° with the $(\bar{1}\ 1\ \bar{1})$ slip plane among all of the slip systems in grain B. Within this slip plane, the most likely resolved shear stress is the one with the maximum Schmid factor with a value of 0.35 in the $[1\ \bar{1}\ \bar{2}]$ direction.

As a result, it can be predicted that the slip system $(1\ \bar{1}\ \bar{1})[2\ 1\ 1]$ from grain A (slip system 1) transmits on the slip system $(\bar{1}\ 1\ \bar{1})[1\ \bar{1}\ \bar{2}]$ in grain B (slip system 2). The predicted slip system is the slip system number 2 in Table 5.6 which has an angle of 6° with the grain boundary line viewed from the pillar's top surface.

According to the criterion suggested by Livingstone and Chalmers, due to the incompatibility and fulfilling the continuity conditions at the grain boundary, a bicrystal requires at least four independent slip systems to yield [*Livingstone and Chalmers*, 1957] (Appendix A). Our bicrystals are compressed over the yield point so that the four expected slip systems activated in bicrystals were detected. Figure 5.16a shows the activated slip systems in a bicrystalline micropillar with a distribution of 3 to 1. A 3D schematic view of the activated slip planes in bicrystals according to theoretical predictions and experimental observations is given in Figure 5.17.

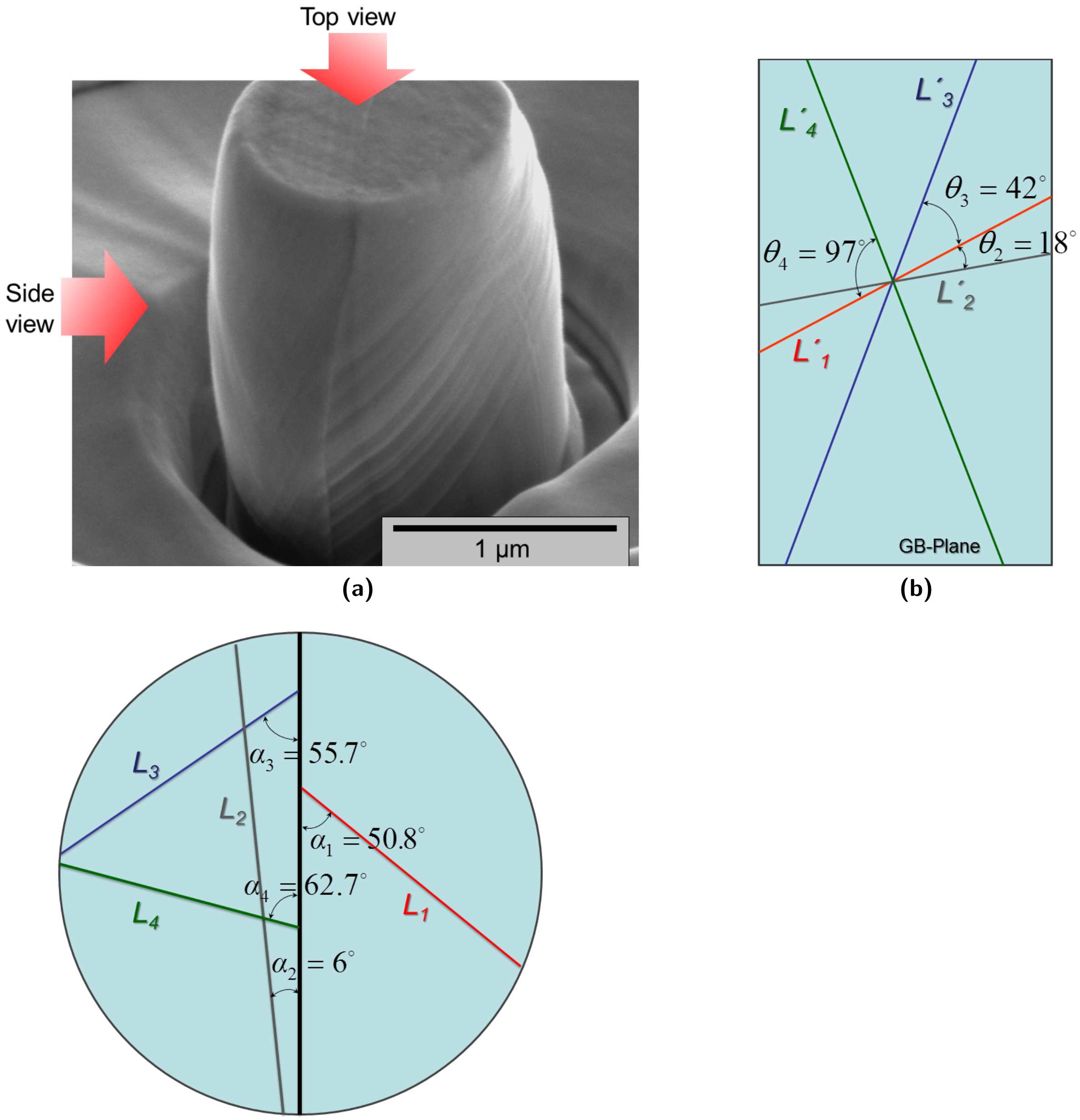

(a) **(b)**

(c)

Figure 5.16.: (a) A typical deformed bicrystalline pillar. In (b), the lateral view, the intersection lines of the slip planes on the grain boundary plane and the θ values are indicated. $\vec{L}'_1$ demonstrates the incoming slip system and the $\vec{L}'_2$, $\vec{L}'_3$ and $\vec{L}'_4$ are the potential outgoing slip systems. In (c), the top view, the intersection lines of the same slip systems with the grain boundary on the pillar top surface and the α values are shown. $\vec{L}_1$ demonstrates the incoming slip system and the $\vec{L}_2$, $\vec{L}_3$ and $\vec{L}_4$ are the potential outgoing slip systems.

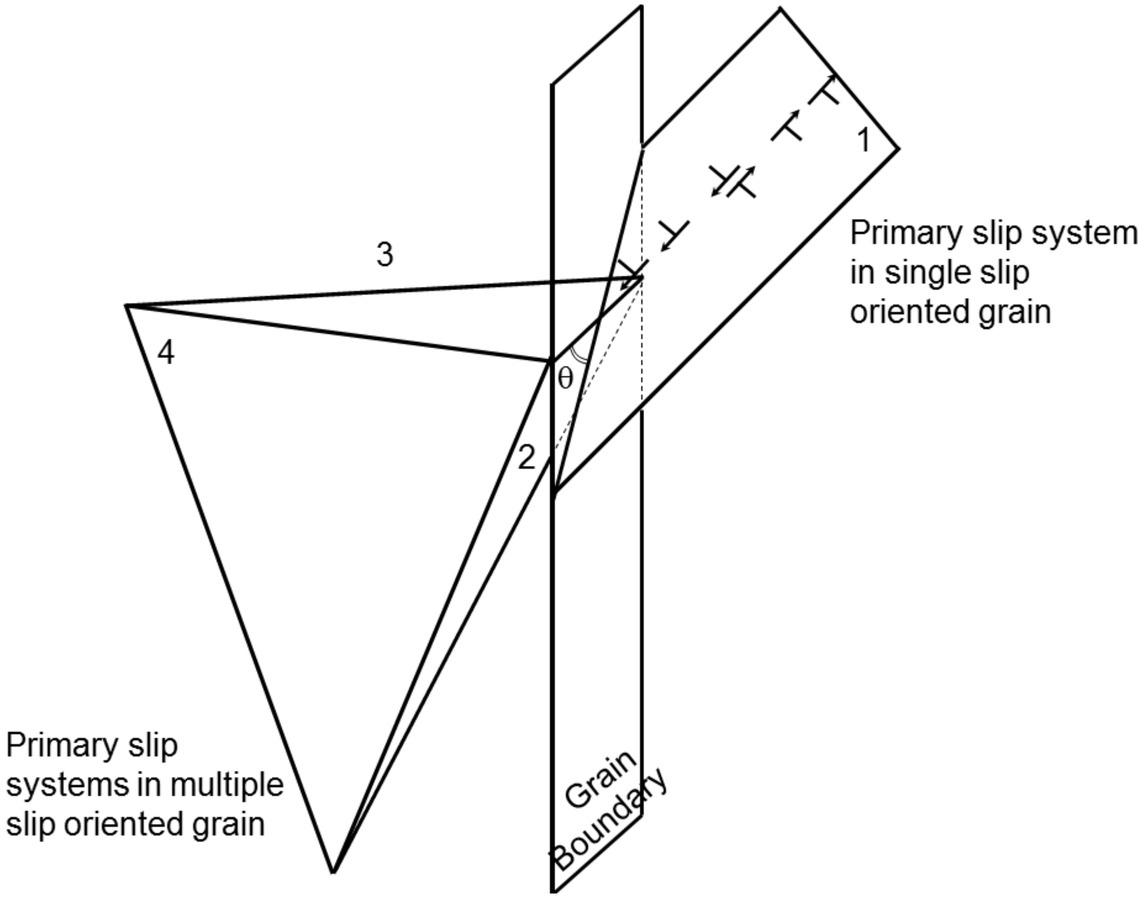

Figure 5.17.: The schematic view of four slip systems activated in a typical bicrystal in this study.

Table 5.6.: Incoming slip system in grain A and potential outgoing slip systems in grain B, Schmid factor, angle α between the intersection lines of the slip planes and the grain boundary line on the bicrystal top surface as well as the angle θ between the incoming slip plane in grain A (slip system 1) and potential slip planes in the grain boundary plane (slip systems 2, 3 and 4).

Grain	(hkl)[uvw]	Slip systems	Slip systems (partial dislocation)	Schmid Factor	α (in degrees)	θ (in degrees)
A	$(1\ 5\ 3)[1\ \bar{2}\ 3]$	1	$(1\ \bar{1}\ \bar{1})\ [2\ 1\ 1]$	0.48	50.8	0
B	$(\bar{6}\ 5\ 5)[\bar{5}\ \overline{17}\ 11]$	2	$(\bar{1}\ 1\ \bar{1})\ [1\ \bar{1}\ \bar{2}]$	0.35	6	18
		3	$(1\ 1\ 1)\ [2\ \bar{1}\ \bar{1}]$	0.24	55.7	42
		4	$(\bar{1}\ \bar{1}\ 1)\ [1\ \bar{2}\ \bar{1}]$	0.35	62.7	97

5.2.5. Slip Transmission

In bicrystals, the stress concentration arisen from the elastic and plastic incompatibilities will be relieved by the activation of secondary slip systems, independently of the primary slip systems, which would be activated in the component crystals if they were free [*Hook and Hirth*, 1967a]. This is called multiple slip [*Livingstone and Chalmers*, 1957] (Figure 5.18). It was also suggested that a bicrystal requires at least four independent slip systems to yield [*Livingstone and Chalmers*, 1957]. This is due to the incompatibility and fulfilling the continuity conditions at the grain boundary (Appendix A). These secondary slip systems always nucleate at the grain boundary in contrast to the primary slip, which has no preferred nucleation site. Primary slip was observed to nucleate at the grain boundary, at the free surface and within the individual component crystals [*Hook and Hirth*, 1967a]. The resolved shear stress on the secondary slip systems is very important. No matter what mechanism prevails in the bicrystal deformation, it is only necessary to raise the shear stress from the tensile resolved shear stress up to the critical resolved shear stress (the resolved shear stress required for the activation of that secondary system) [*Hauser and Chalmers*, 1961]. This phenomenon was referred to as *Slip Transmission* and was studied in the literature. Here, a brief discussion is given of the slip transmission in our experiments by means of direct observation of deformed bicrystals in the high-resolution SEM.

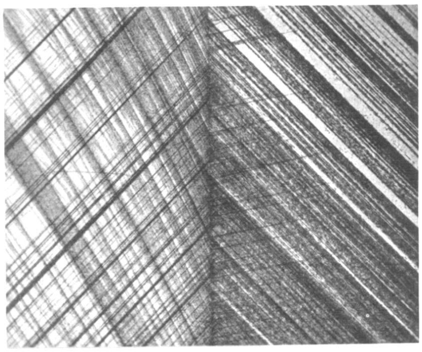

Figure 5.18.: Activation of secondary slip systems at the grain boundary in a bicrystal with the presence of primary slip systems (× 150) [*Hook and Hirth*, 1967a].

In previous studies, the macroscopic bicrystals were composed of grains, in which only one primary slip system would be activated if they were free. However, multiple slip (secondary slip systems in addition to primary slip systems) was observed in those macroscopic bicrystals. The measured yield stress of the macroscopic bicrystals was proposed to be controlled by the pile-up stress, which activates dislocation sources on these secondary slip systems in the adjacent grain [*Livingstone and Chalmers*, 1957]. In other words, bicrystal yielding occurs when the slip transfers from one grain to the next one.

In our study, the situation is somewhat different. The component crystals are chosen in such a manner that in one grain one primary slip system would be activated, and in the other grain three primary slip systems would be activated, if they were single crystals. This was observed in our experiments on single-crystalline micropillars (see section 5.1). Thus, any further secondary slip systems would not be required to fulfill the compatibility conditions, which implies that no slip transmission is going to take place. However, in SEM observations of small bicrystalline micropillars, those below 1.5 μm in diameter, four activated slip systems were observed, and along the grain boundary, a one to one alignment of slip system 1 and slip system 2 was detected (Figures 5.19). It is believed that in these alignment points the density of slip is so high, that there is a fairly high degree of slip band continuity across the grain boundary [*Hook and Hirth*, 1967a]. Assuming the slip transmission has occurred at these points, one can say that in small bicrystalline micropillars the primary slip system 2 is activated by slip transmission in the same manner as the activation of a secondary slip system. The limited number of dislocation sources in the bicrystal comes to a prompt interaction with the grain boundary. The high misorientation angle of the adjacent grains results in the dislocation accumulation at the boundary. The incoming dislocations at the boundary must rotate their line direction by the angle θ (defined in section 5.2.4), so that they match their slip plane with one potential slip system in the next grain and cross the grain boundary. The slip line analysis in section 5.2.4 also confirmed that the angle between the slip plane of slip system 2 and the slip plane 1 (the incoming slip plane) on the grain boundary plane is minimum (18° in comparison to other slip systems with angles 42° and 97°). By further increasing the load, the stress at the tip of the pile-up achieves the critical resolved shear stress of a new slip system in the adjacent grain [*Hauser and Chalmers*, 1961]. The slip transmission can occur by activation of new dislocations on the new slip system or by transmission of the already piled up dislocations at the boundary. Once slip transmission has occurred, dislocations can move through the boundary and the strain hardening decreases, observed in the form of pop-ins within stress-strain curves of the small bicrystalline micropillars (Figures 5.7a and 5.9a).

Whether this phenomenon controls the yield of small bicrystals cannot be answered here, since there is no experimental evidence for that. We tried to perform compression tests on small bicrystalline micropillars step by step until the stages *before*, *at* and *after* the yield point, in order to determine the relation between slip transmission and the yield stress. However, our efforts failed, since the limited resolution of the SEM equipment did not allow us to observe the slip lines, especially at small strains. Another possibility for finding the relationship could be to perform in-situ compression test of bicrystalline micropillars with high spatial and time resolutions (see outlook 6.2.2). In this way the slip transmission can be captured more precisely. At this point, the experimental limitations hindered us from explaining the slip transmission and its influence on deformation mechanisms. Therefore, we used the advantages of MD simulation. In section 5.3 the simulation results give us a better understanding of this.

The activated slip systems after 3 % strain are shown in Figure 5.20 for bicrystals with a diameter of 5 μm. With the achieved resolution in the SEM systems (better than 10 nm), slip systems 1, 3 and 4 were easily resolved (Figure 5.20a), however slip system 2 was a bit more difficult to resolve (Figures 5.20b and 5.20c). In contrast to the small bicrystalline micropillars, a one to one alignment of the incoming slip

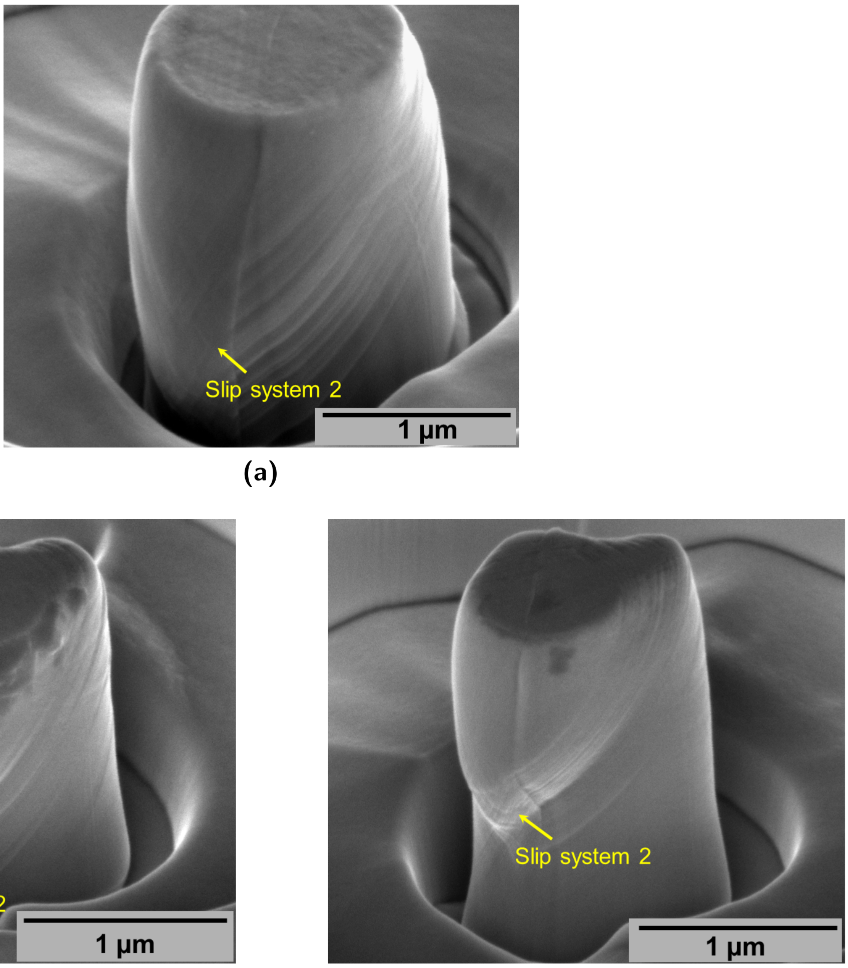

(a)

(b) **(c)**

Figure 5.19.: Activation of slip system 2 in different small bicrystalline micropillars.(a) 1.4 μm diameter after 12% straining, (b) 1 μm diameter after 16% straining and (c) 1 μm diameter after 20% straining.

system (no. 1) and the outgoing slip systems (no. 2) was not regulary observed as an evidence for slip transmission (Figure 5.5a). In another bicrystalline micropillar with a similar grain boundary, two slip systems were obserevd in each of the component crystals (Figure 5.20d). This implies that the large bicrystalline micropillars were deformed by activaion of at least four slip systems with a distribution of 3 to 1 as well as 2 to 2 in the component crystals.

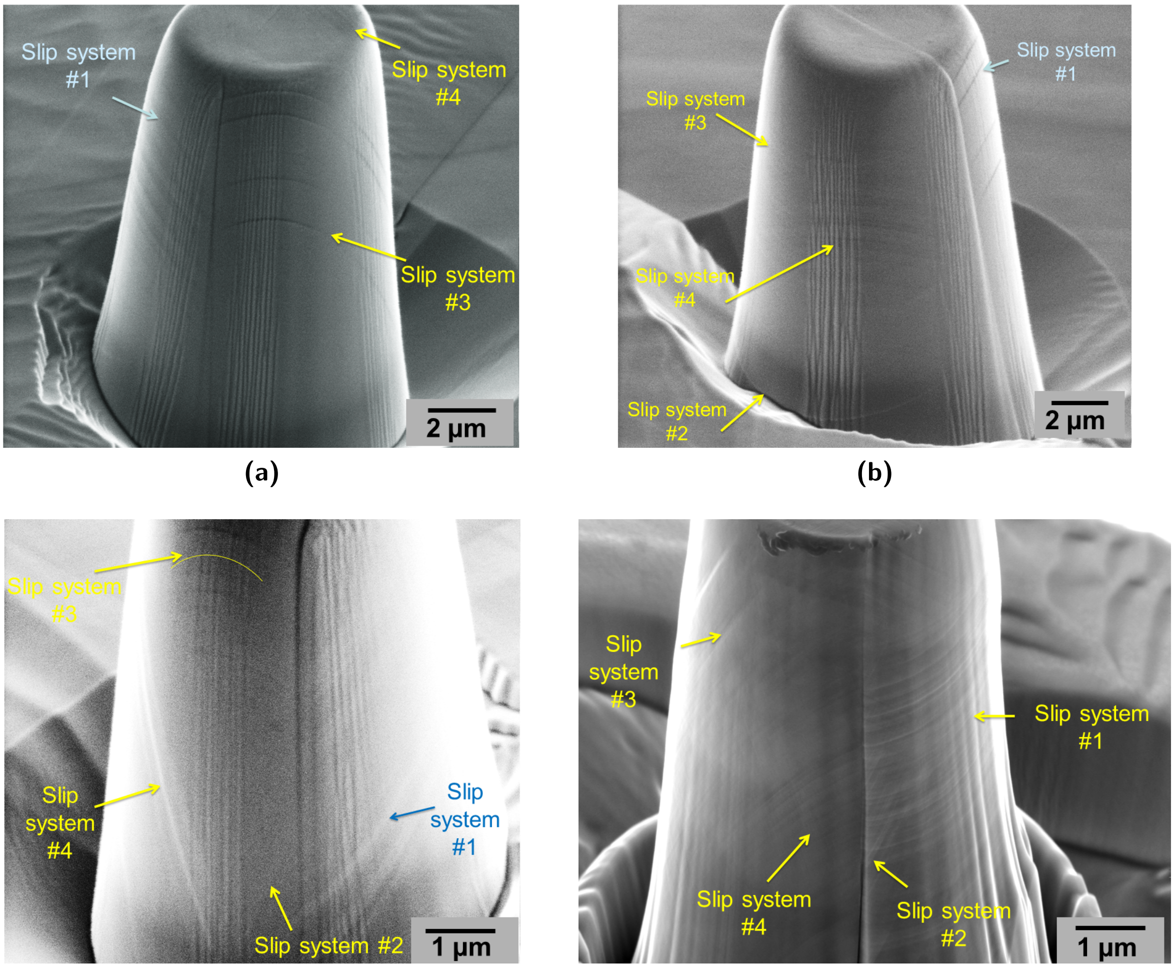

(a) **(b)**

(c) **(d)**

Figure 5.20.: Activation of slip systems in a bicrystals with 5 μm diameters. (a), (b) and (c) SE contrast images of one bicrystal from different views after 3 % straining. (d) SE contrast image of another bicrystal with a similar grain boundary after 12 % straining.

These results are in agreement with the observations of macroscopic bicrystals in the literature ([*Livingstone and Chalmers*, 1957], [*Hauser and Chalmers*, 1961] and [*Hook and Hirth*, 1967a]) and of Miura and Saeki [*Miura and Saeki*, 1978], who showed that the stress-strain curves of the isoaxial symmetric bicrystals, having low (4° and 14°) and high misorientation (37°) boundaries, show similar stress-strain curves to that of the single crystals (Figure 2.5). They suggested that the piled-up dislocations pass the low angle misoriented grain boundary through prominent cross slip, while for the 37° boundary, which has a large misorientation, clustered slip cannot pass the boundary and multiple slip (activation of secondary slip systems in addition to primary one to fulfill compatibility conditions) is introduced at the boundary at the beginning of the deformation, which is the main effect of the grain boundary on the flow stress. They exclude the contribution of the pile-up back stress as well as the grain boundary dislocation formation. The Burgers vector of a grain boundary dislocation, $\vec{b}_{\text{grain boundary}}$, which is formed when a dislocation passes through the boundary, depends on the misorientation between $\vec{b}_A$ and $\vec{b}_B$, where $\vec{b}_A$ and $\vec{b}_B$ are the Burgers vectors when a dislocation lies on grain A and B, respectively. With a large misorientation, a boundary dislocation with a large Burgers vector is required to form and is energetically unfavorable. It is energetically more favorable when a dislocation with a Burgers vector $\vec{b}_A$ in grain A passes to a dislocation on the slip system of grain B with a Burgers vector $\vec{b}_B$ which has a smaller misorientation than $\vec{b}_A$.

5.2.6. Consideration of elastic anisotropy

The bicrystals studied here are non-isoaxial. This means for nickel, as an elastic anisotropic material, there are different elastic moduli for the two component crystals, as given in Table 5.7. Under a condition of uniform axial elastic strain, the component crystals of the bicrystals are not equally stressed, resulting in elastic incompatibilities at the grain boundary. The ratio of the applied stress is proportional to the ratio of elastic moduli of the two component crystals in the axial direction. The stress distribution applied on the component crystals (called crystals A and B) by the bicrystal during the elastic deformation are given by Equations 5.7 and 5.8 [*Hook and Hirth*, 1967b].

$$\sigma_A = \frac{\sigma_T A_T}{A_A + \frac{E_B A_B}{E_A}} \tag{5.7}$$

$$\sigma_B = \frac{\sigma_T A_T}{A_B + \frac{E_A A_A}{E_B}} \tag{5.8}$$

where σ_T is the total applied stress and A_T is the total surface of the bicrystal. A_A and A_B are the surfaces, and E_A and E_B are the elastic moduli of component crystals A and B. Since the volume fractions of component crystals A and B are the same, by substituting the elastic modulus of each component crystal in Equations 5.7 and 5.8, the stress distribution in the bicrystal will be obtained as given in Table 5.7.

Table 5.7.: Stress distribution of the component crystals.

Grains (i=A or B)	Elastic modulus	σ_i
A (Single slip orientation)	182	0.83 σ_T
B (Multiple slip orientation)	258	1.17 σ_T

The above results are evidence that the component crystal having the higher modulus (grain B), will be stressed to a higher level than the component crystal with the lower modulus (grain A), at the same level of total load. According to Schmid's law, $\vec{\tau} = m \cdot \vec{\sigma}$, the grain with the higher Schmid factor (m) starts yielding, if it would be free.

Substitution the Equation 5.7 and 5.8 into the Schmid law yields the following relations for crystals A and B (Equation 5.9 and 5.10).

$$\tau_A = m_A \cdot (\frac{\sigma_T A_T}{A_A + \frac{E_B A_B}{E_A}}) \tag{5.9}$$

$$\tau_B = m_B \cdot (\frac{\sigma_T A_T}{A_B + \frac{E_A A_A}{E_B}}) \tag{5.10}$$

By inserting the largest Schmid factors of the two component crystals, m_A and m_B, as well as the elastic moduli values, E_A and E_B, into Equations 5.9 and 5.10 (from Table 3.6, section 3.2), the applied shear stress distribution on the primary slip systems in the component crystals will be obtained (Table 5.8). This shows that the primary slip systems in crystal A (single slip orientation), with a factor of $0.39\sigma_T$, will be more highly stressed than crystal B (multiple slip orientation), with a factor of $0.36\sigma_T$.

Table 5.8.: Applied shear stresses on the primary slip systems in the component crystals of the bicrystal using Equations 5.9 and 5.10.

Grains	Schmid factor (m)	τ
A	0.48	0.39 σ_T
B	0.31	0.36 σ_T

5.2.7. Consideration of source properties

In many cases, particularly for pile-ups containing a large number of dislocations, the approximation of a continuous distribution in a pile-up is about as good of an approximation as the discrete model [*Hirth and Lothe*, 1982]. Despite the apparent success of the continuum models, there are non-empirical intuitive reasons to modify them. Chief among these reasons is that the continuum models fail to take into account dislocation source characteristics, specifically the critical source activation stress and the source position. When decreasing the experimental scales, it is important to consider these critical parameters; i.e. source position and source activation energy. Friedman and Chrzan [*Friedman and Chrzan*, 1998] modified the standard continuum theory of dislocation pile-up to include the source characteristics. The new model will be referred to as the *modified continuum theory*, and the earlier continuum theories will be referred to as *standard continuum theories* or source-independent theories. The applied stress in the new model is given in Equation 5.11.

$$\sigma_A = (\frac{\mu b \sigma_B}{\pi d} + \sigma_c^2)^{1/2} \tag{5.11}$$

where σ_A is the applied stress, μ the shear modulus, b the Burgers vector, σ_B the pile-up back stress or grain boundary strength, d the grain size and σ_c the source activation stress. Depending on the position of the dislocation source, we should differentiate between two cases: the double-ended pile-up (Figure 5.21a) and the single-ended pile-up (Figure 5.21b). Applying this to our bicrystalline micropillars, it should be noticed that the component crystals of the bicrystalline pillars are free on one side, so the dislocations can exit the crystal from the free surface. Hence, no matter where the dislocation source is situated, on the surface, in the crystal interior or on the grain boundary, we are dealing with a single-ended pile-up (Figure 5.22). As more dislocations are introduced into the pile-up, the tail of the pile-up approaches the source. The tail is separated from the source by a dislocation-free region. At the limit $d \to \infty$, the dislocations at the end are far away from the source, and the back stress at the source is negligible. Consequently, any number of dislocations can be produced at stresses which are marginally above the source activation stress [*Friedman and Chrzan*, 1998]. In contrast, when d decreases, the tail of the pile-up approaches the source faster and the number of dislocations in the pile-up will be limited. Thus, the local force acting on the dislocation pile-up decreases due to the following relation $\frac{F}{L} = \tau N b$. As a result, it is necessary to increase the external load to compensate for the required local stress and promote slip transmission.

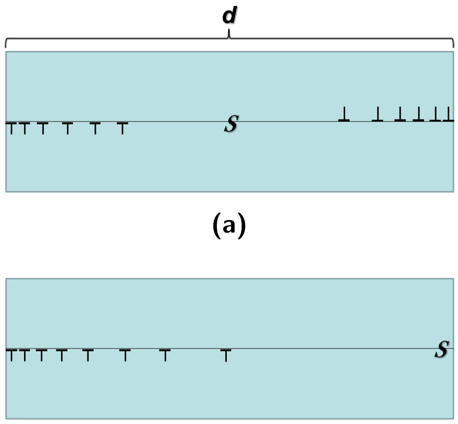

(a)

(b)

Figure 5.21.: (a) Double-ended and (b) single-ended pile-ups for two different positions of the Frank-Read source as proposed by Friedman and Chrzan [*Friedman and Chrzan*, 1998]. $\boldsymbol{S}$ represents a Frank-Read dislocation source and d the grain size.

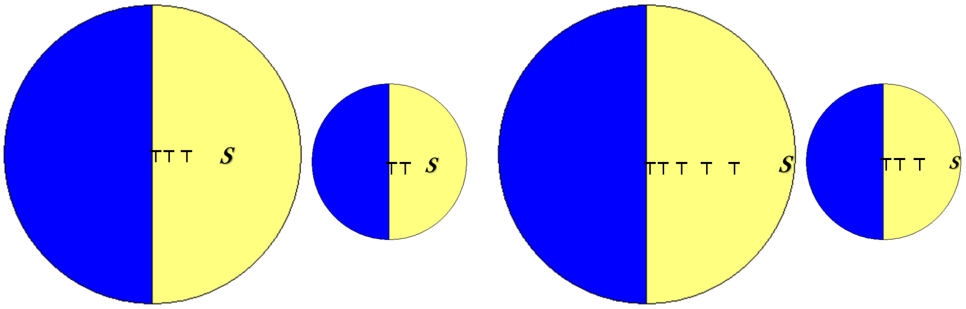

(a)

(b)

Figure 5.22.: Single-ended pile-up for two different positions of the Frank-Read source: (a) in the crystal interior and (b) on the crystal surface. $\boldsymbol{S}$ represents a Frank-Read dislocation source. It is shown that the crystal size affects the number of dislocations in the pile-up.

5.2.8. Consideration of size effect hypothesis

A review of the literature may raise the question of whether there exists any other explanation for the different deformation behavior of large and small bicrystals. One can claim that the proposed theory regarding the strengthening effect of the grain boundary in small bicrystals is only due to the parallel compression of the two single-crystalline pillars which are smaller and therefore stronger. In general, size effects in dislocation-mediated plasticity can be classified in two types. The first class of size effect occurs when a microstructural or external size interferes with some characteristic length intrinsic to the dislocation-mediated plastic process going on. Such interference originates a *size-induced transition* [*Sevillano et al.*, 2001], for example the ductile-whisker behavior transition, as well as other anomalous effects that are relevant for micro-systems e.g. single-crystalline micropillars. For single-crystalline micropillars, a source-limited plasticity behavior is proposed by [*Volkert and Lilleodden*, 2006; *Greer et al.*, 2005; *Greer and Nix*, 2006] to describe the higher stresses obtained by scaling down the sample size. The second class of size effect is linked to the development of mesoscopic plastic strain gradients induced by microstructural heterogeneities or by boundary conditions. The effect of the diameter on the torsional plastic response of plain cylinders and the bending of a beam, the indentation size effect, the deformation of plastic crystals containing hard, nondeforming particles and the plastic deformation of polycrystals are well-known phenomena of this type.

In our experiments, the variation of the flow stress in different *single crystal pillar* sizes is explained by the first class size effect. The flow curves of single crystals oriented for single slip show higher stresses by decreasing the size of the pillars (Figure 5.23a). The 1 μm pillars show extremely higher stresses than the other larger samples at yield point as well as during the straining. In the case of the multiple slip orientation, the flow stress curves indicate higher stresses at yield and work hardening with decreasing sample size. However, the small-scale pillars with 1 μm diameter show different behaviors, as discussed previously in section 5.1.3. Two examples are shown here and are marked in Figure 5.23b as “Multiple slip activation” and “Single slip activation”, depending on how the deformation proceeds.

Similar to single-crystalline micropillars, bicrystalline micropillars also showed increasing flow stress by decreasing the size (as observed in Figure 5.13). This behaviour can be explained by the size effect of the first class. Though, in contrast to single crystals, bicrystals are heterogeneous systems. Assuming the applied stress is homogeneous, due to the different crystallographic orientation of their component crystals, their deformation is elastically and plastically incompatible (Appendix A). Thus, in addition to the size effect firs class, they fulfill the the second class size effect, which predicts the greater the imposed strain gradient is, the greater the degree of hardening will be. The degree of strain hardening depends directly on a characteristic length scale. Strain gradient effect diminishes rapidly by increasing this length scale [*Fleck et al.*, 1994]. For example, hardness, when measured on a micron scale, is greater than that at the millimeter scale. In bicrystalline micropillars, the near-boundary-area straining is much more restricted to deformation than the near-surface area, which leads to the strain gradients. This

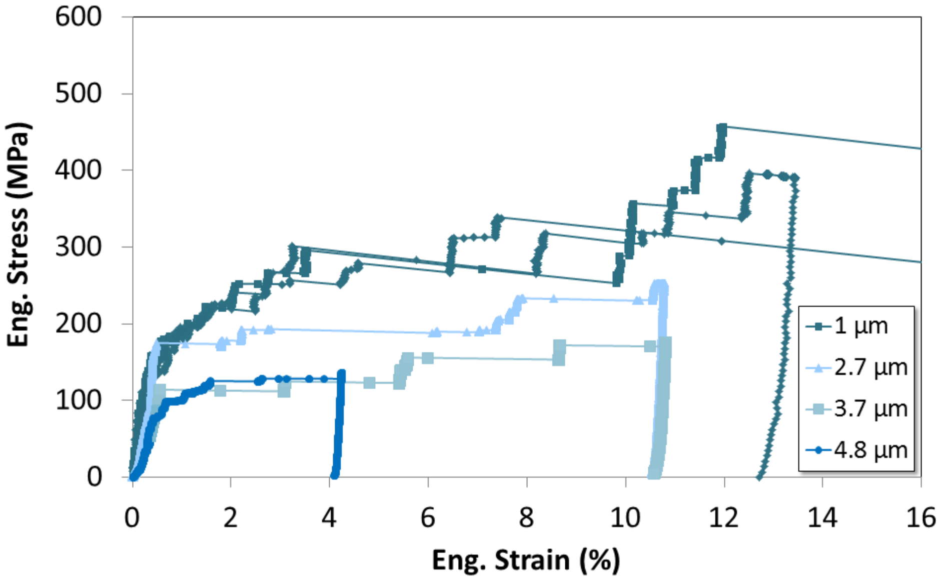

(a)

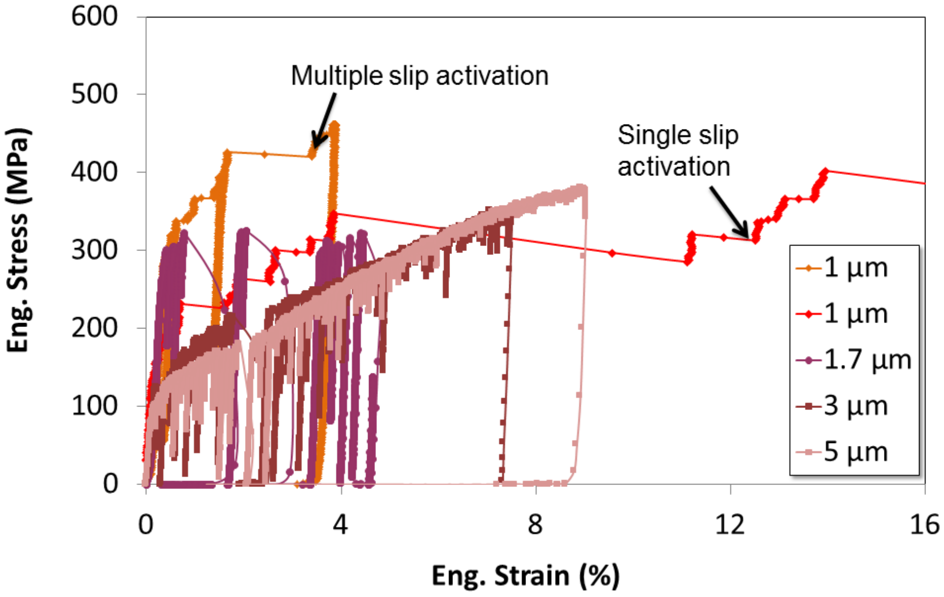

(b)

Figure 5.23.: Size effect of single-crystalline pillars with (a) single slip orientation and (b) multiple slip orientation.

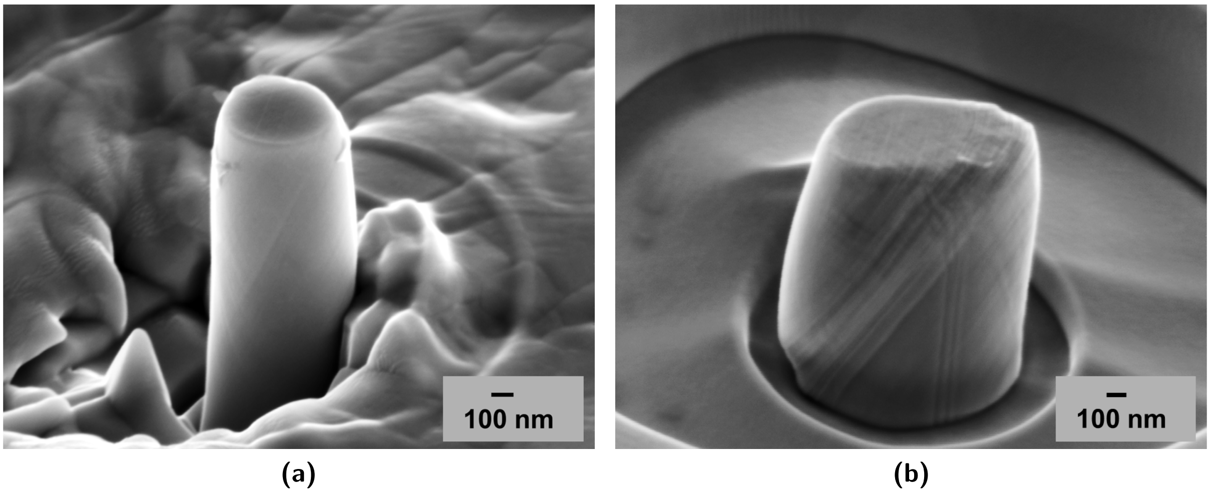

Figure 5.24.: Post-deformation SEM images of 1 μm diameter single crystals oriented for ≈ (1 1 1). The single-crystalline micropillars after compression test with (a) multiple slip activation and with (b) single slip activation according to the marked curves in Figure 5.23b are shown.

strain gradient increases by decreasing the size of the bicrystalline micropillar. For a compatible deformation, GNDs must be formed in addition to statistically stored dislocations, and the total number of these two types of dislocations will determine the hardening.

It may be thought that the higher stress of bicrystals is a result of the *class 1 size effect* and not an effect of the grain boundary. For the explanation, let us assume that the grain boundary divides the micropillar exactly in two halves; the bicrystal with the surface A is now composed of two single crystals with the same surface portions, A_1 and A_2, respectively (Figure 5.25). Now, suppose that instead of the bicrystal, two smaller single-crystalline micropillars are compressed, which are connected in parallel (Figure 5.26). Thereby, we have the following relation: $A = A_1 + A_2$, where $A_1 = A_2$, then $A = 2A_1 = 2A_2$. By substitution we have $\pi R^2 = 2\pi r^2$, where R is the radius of the bicrystal and r the radius of the two component single crystals. This means that instead of compressing a bicrystal with diameter R, two single crystals of diameter r, with values according to the relation $r = R/\sqrt{2}$, are deformed. This comparison is listed in Table 5.9. Therefore, it is allowed to suppose that the flow stress of the bicrystal is equal to the flow stress of the component single crystal which yields later, i.e. the component crystal with multiple slip orientation controls the flow stress of the bicrystal.

Applying this theory to the flow stresses (at 0.5 %) of all the bicrystals and comparing the flow stress of bicrystals of diameter R with the multiple slip oriented single crystals of diameter r leads to the following results (Figure 5.27). In large and medium-sized bicrystals (5 to 2 μm), single crystals show higher stresses than bicrystals. In bicrystals with 1.4 μm diameters, the situation is different. Bicrystals deform with higher stresses than single crystals. If the bicrystals deform with the same stresses as the single crystals (as per the radius relationship $r = R/\sqrt{2}$), then we could talk about the size effect

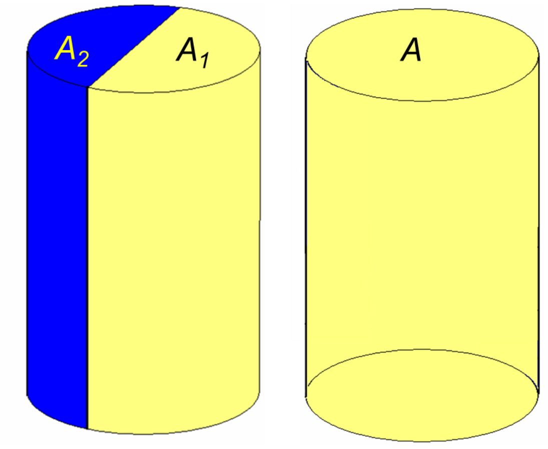

Figure 5.25.: Schematic comparison of two micropillars the same size with and without the grain boundary.

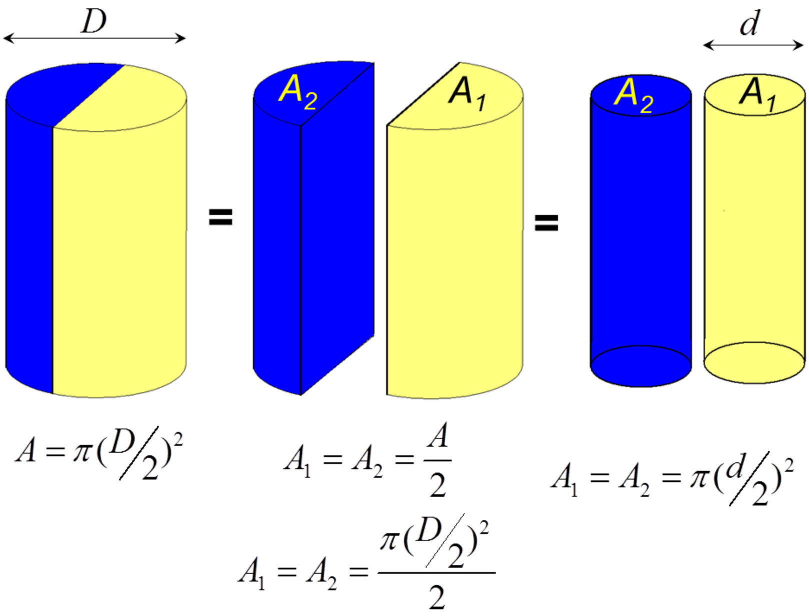

Figure 5.26.: The relation between radii of the assumed two single crystals and the corresponding bicrystal.

Table 5.9.: The bicrystal and single crystal diameters with the relationship $r = R/\sqrt{2}$.

Bicrystal diameter (R in μm)	Single crystal diameter (r in μm)
5	3.5
3	2
2	1.4
1.4	1

as the main effective phenomenon. However, this is observed only in the large and medium sizes. This means that the grain boundary hardening appears first by decreasing the grain size, which is a confirmation of the first explanation (see section 5.2). In small bicrystalline micropillars it was proposed that the dislocaion-grain boundary interaction controls the deformation mechanism rather than the interaction between the dislocations, which leads to the higher stresses required for deformation.

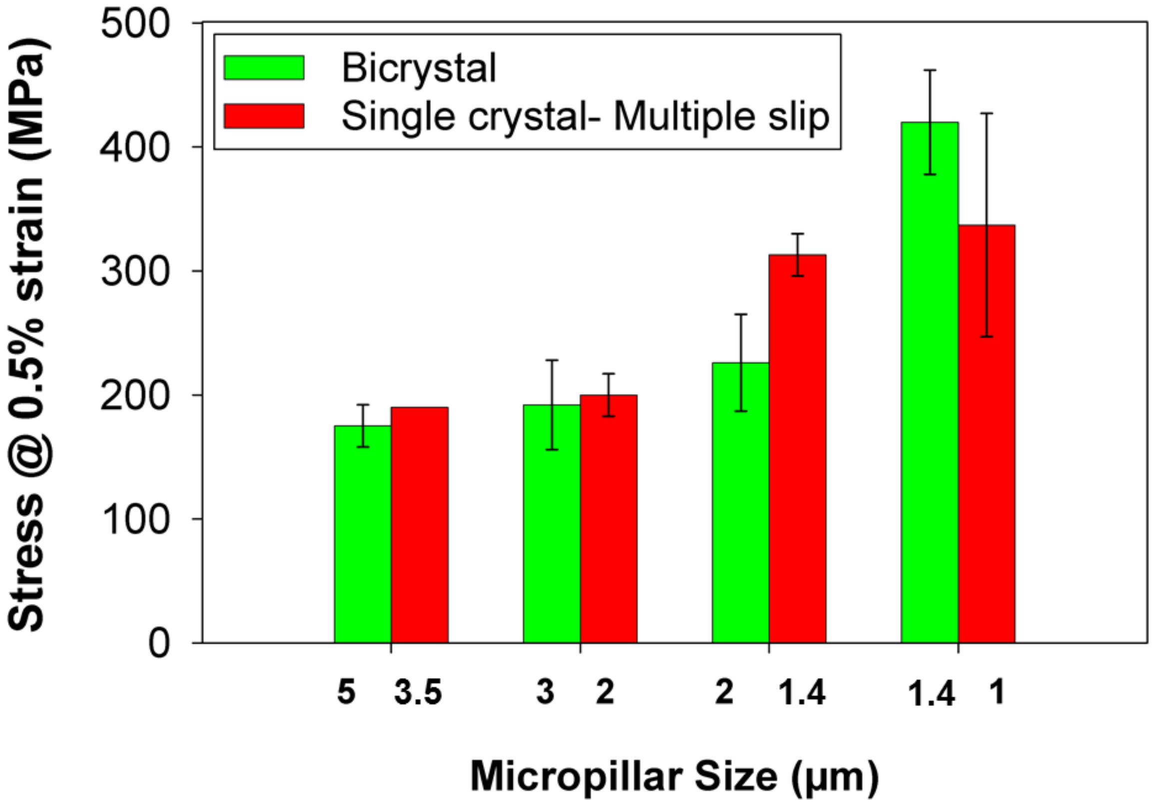

Figure 5.27.: Bicrystals with diameter R are compared with the multiple slip oriented single crystals of diameter r, where $R = \sqrt{2}\, r$.

5.3. Results of MD Simulation

MD simulation was performed to demonstrate the deformation at higher resolution. The stress-strain curve obtained from simulation is shown in Figure 5.28. At the marked points on the curve, the simulation sectional views are given in Figure 5.29.

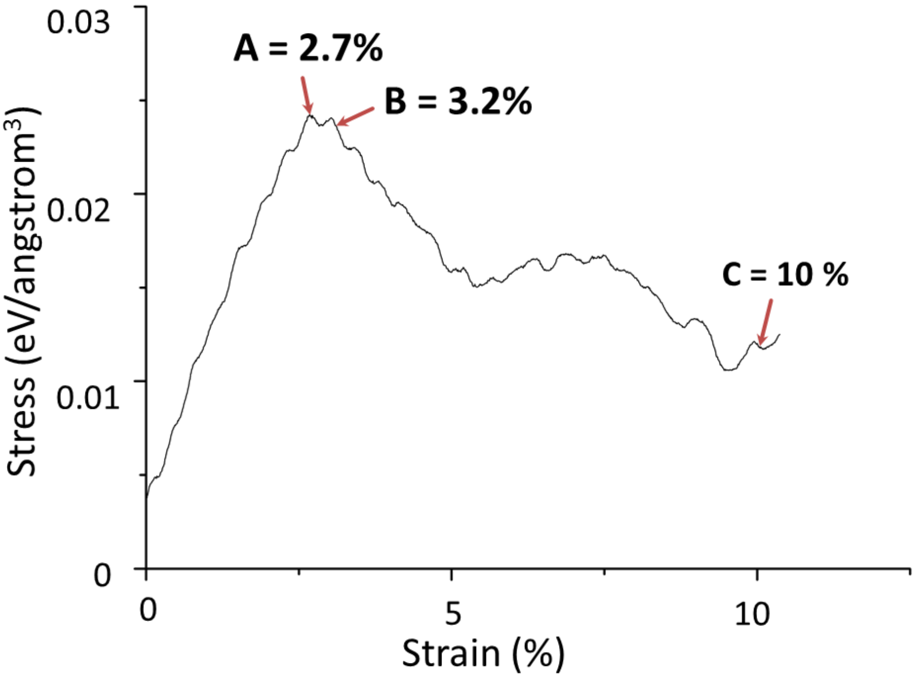

Figure 5.28.: Stress-strain curve obtained from the simulation of a bicrystal under compression testing.

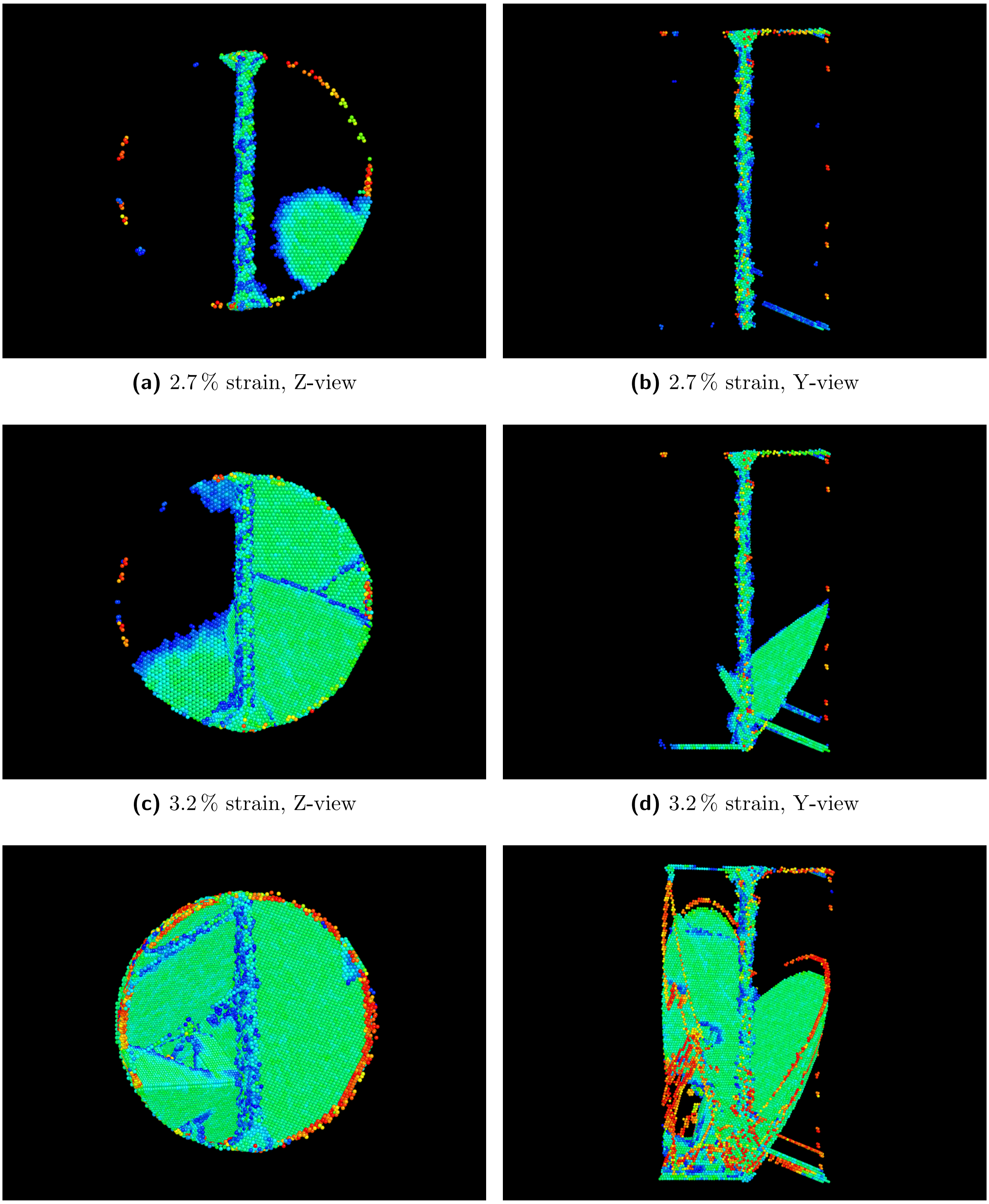

(a) 2.7 % strain, Z-view

(b) 2.7 % strain, Y-view

(c) 3.2 % strain, Z-view

(d) 3.2 % strain, Y-view

(e) 10 % strain, Z-view

(f) 10 % strain, Y-view

Figure 5.29.: Sectional views from Y and Z directions at different strains shown by points A, B and C in Figure 5.28.

5.4. Discussion on MD simulation results

Three critical and interesting points of pillar deformation were selected. Point A at the yield point, where the stress-strain curve changes from elastic to plastic deformation. Point B at 3.2 %, where the stress reduces. The final point C was taken at the end of deformation procedure at 10 % strain.

At 2.7 % strain the Z and Y views (Figures 5.29a and 5.29b) show that the plastic deformation has already started, however, only in one crystal. The deformation starts at the edge of the pillar in direct contact with the flat-ended tip[3]. On this area the stress concentration is so high and inhomogeneously distributed that secondary slip systems will be activated as observed in experiments of this study and of Kiener et al. [*Kiener et al.*, 2008b].

The magnified view (Figure 5.30b) shows that in some areas along the boundary, the order of atoms has changed compared to the initial state of the boundary (Figure 5.30a). It shows that, before the boundary contributed to the deformation, the deformation was in elastic regime. The plastic deformation starts once the grain boundary starts to deform.

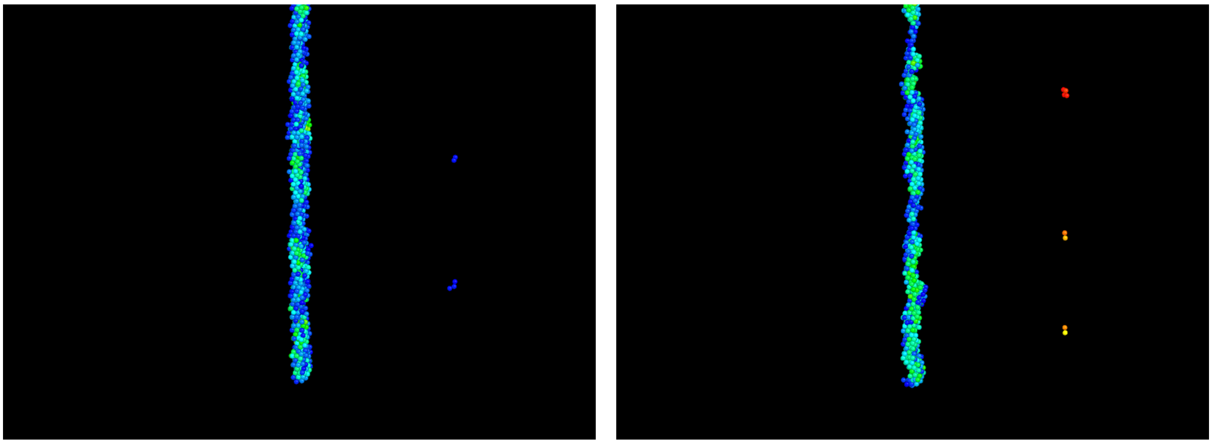

(a) 0 %, Y-view **(b)** 2.7 %, Y-view

Figure 5.30.: (a) Grain boundary at initial state (0 % strains) compared to (b) the yield point (2.7 % strains).

At strains of 3.2 % the stress decreases on the curve. Figures 5.29c and 5.29d show that at this strain yield has already started in both component crystals. In the component crystal with single slip orientation (on the right), the slip reaches the grain boundary from one side, and the free surface from the other side. A focused observation of the grain boundary shows the slip transmission from the crystal with single slip orientation to the crystal with multiple slip orientation (from the right to the left) (Figure 5.31). A comparison with the slip line analysis data shows that the slip is transmitted on the similar slip plane with the minimum angle with the incoming slip plane as predicted by

---

[3] In the simulation images the micropillars are compressed by the flat-ended tip from the bottom up.

the calculation (see section 5.2.4). The reduction of stress can be explained by the fact that before slip transmission, the dislocation motion was hindered by the boundary. By increasing the load, the stress concentration at the tip of the pile-up achieves the critical resolved shear stress of the slip system in the adjacent crystal. This leads to stress relief and the bicrystal requires lower stresses to continue the deformation.

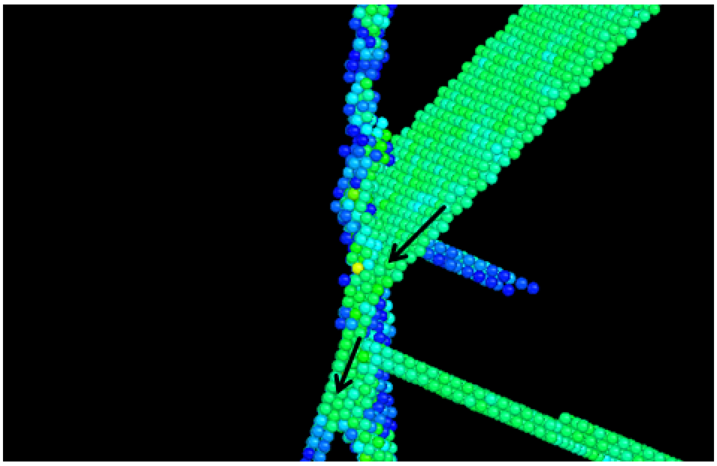

Figure 5.31.: A magnified view of the deformed pillar shows the slip transmission.

At relatively high strains (10 %), three slip systems in the crystal with multiple slip orientation and one slip system in the crystal with single slip orientation are activated in correlation with experimental observations (Figure 5.32).

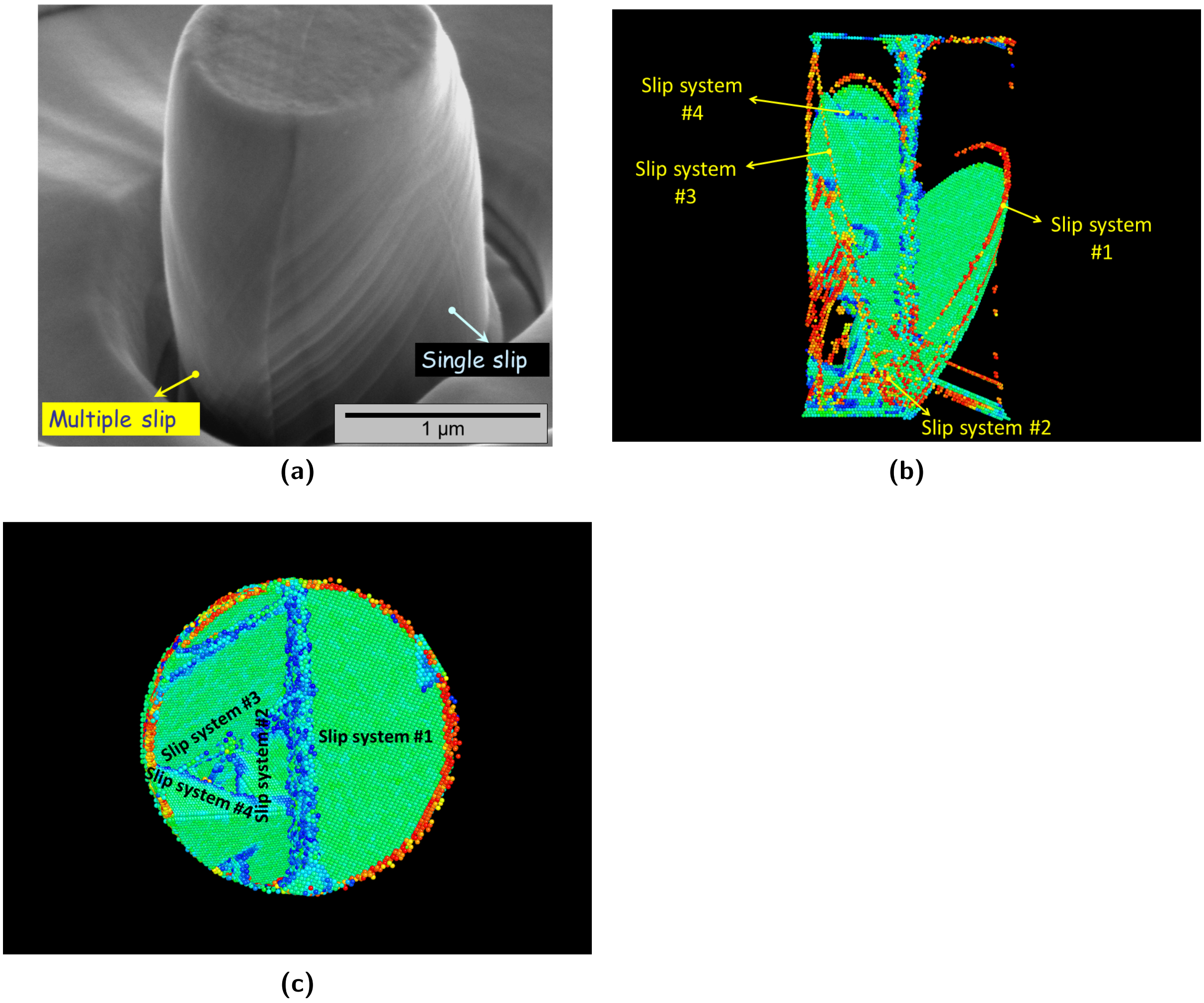

(a)

(b)

(c)

Figure 5.32.: MD simulation predicts the activation of identical slip systems as observed in experiments. (a) A bicrystal experimentally deformed to 12 % strain. MD simulations of a bicrystal with the same properties deformed to 10 % viewed from (b) Y and from (c) Z directions.

5.5. Preliminary conclusion

Stress-strain curves from the compression test of bicrystals in mesoscopic scale, with diameters between 1 and 5 μm, show a clear size effect on the flow stresses measured at 0.5 %. The large bicrystalline micropillars (5 μm) show no difference with the single-crystalline micropillars of the same size with multiple slip orientation. Compression of the large-sized bicrystals resembles the compression of two smaller single-crytsalline pillars connected in parallel, so that the grain boundary has no inherent effect. The component crystal with the single slip orientation (1 5 3) starts to yield earlier, since with a stress distribution factor of $0.39\sigma_T$, it is stressed to a higher extent than the component crystal with (1 1 1) orientation with a factor of $0.36\sigma_T$. However, the bicrystal as a unique system, starts to deform when the component crystal with crystallographic orientation of (1 1 1) starts yielding. Hence, the latter controls the flow stress. From the 2 μm diameter pillars, higher stresses were obtained for bicrystals, which increased with decreasing micropillar diameter. This change was explained by the pronounced effect of the grain boundary in small bicrystalline micropillars. The number of dislocation sources and the interaction of dislocations with the grain boundary controls the deformation. The motion of the dislocations will be constrained by the grain boundary and they will pile up there. It should be noted that the accumulated dislocations are from both statistically stored dislocations and the GND type. Strain gradient plasticity in bicrystalline micropillars, as inhomogeneous systems, results in accommodation of GNDs.

Once the stress concentration at the tip of the pile-up reaches the critical resolved shear stress of a slip system in the adjacent grain, the bicrystal starts yielding. In the small-sized bicrystals the stress at the pile-up decreases. Therefore, higher external loads are required for crossing the grain boundary and slip transmission from one grain to the next one. Slip transmission can occur on a primary or a secondary slip system in the next grain depending on the relative misorientation of the two component crystals adjacent to the grain boundary; i.e. the relative position of the intersection lines of the slip planes on the grain boundary. It is important that the incoming slip system match itself on a more energetically favorable *potential slip system* in the adjacent grain. The slip line analysis, with the help of SEM observations and the geometric rules, showed that this potential slip system slip has a minimum angle of 18° with the incoming slip system, and is a primary slip system (out of three primary slip systems) in the next component crystals. It was also observed that under elastic and plastic incompatibility conditions the bicrystals requires at least four slip systems for compatible deformation in agreement with the literature [*Livingstone and Chalmers*, 1957; *Hook and Hirth*, 1967b]. As the component crystals were oriented, so that three primary slip systems in one grain and one primary slip system in the other grain would be activated (if they were single crystals), any secondary slip system was observed to be activated in these bicrystals. Hence, higher stresses obtained in small sizes bicrystals is a result of grain boundary strengthening effect.

It was shown computationally that, the higher stresses achieved in smaller bicrystals is a results of both types of size effects. The size-induced transition and the plastic strain gradients, which are induced by microstructural heterogeneities. A question was still unanswered due to the experimental limitations: whether the slip transmission occurs at the yield point. In order to answer this question, we performed MD simulation of bicrystalline micropillars with similar properties to the experiments. The simulation results show slip transmission on the same slip systems as observed in the bicrystals in the experiments. At yield point, the grain boundary starts to be unstable and the obvious slip transmission was detected at strains slightly higher than the yield point by +0.5 %. The results of simutation were in agreement with the experiments in terms of the types of activated slip systems.

5.6. Results of microstructural tests

As explained in section 3.4.1, we characterized three different deformed microstructures:

1. A homogeneous medium with easy glide behavior
2. A homogeneous medium with the presence of non-planar dislocations
3. An inhomogeneous medium with the presence of a grain boundary

In the following section, the results of EBSD measurements and the consequent misorientation and OGM analyses of OIM maps are presented.

5.6.1. Homogeneous medium with easy glide behavior

The SE contrast image of the single-crystalline micropillar (Figure 5.33a) and the corresponding stress-strain curve (Figure 5.33b) show that the pillar was deformed to small strain values (≈5 %). The pillar is embedded in an amorphous Pt protection layer, which is marked on the figure (Figure 5.33c). The OIM map (Figure 5.33d), the misorientation analysis with respect to an undeformed point (Figure 5.33e) and the OGM analyis (Figure 5.33f) are also provided.

5.6.2. Homogeneous medium with the presence of non-planar dislocations

In another single-crystalline micropillar, with double slip orientation, two slip systems are activated (Figure 5.35a). By stepwise compression of the sample, it was observed that the first and the second strain bursts on the flow curve are in accordance with the activation of the two slip systems (Figure 5.34). The SE contrast image of the pillar from a view perpendicular to slip direction (Figure 5.35a), the SE image of its cross section (Figure 5.35b), the OIM map (Figure 5.35b) and the misorientation analysis with respect to an undeformed point (Figure 5.35d), as well as the OGM analysis (Figure 5.35e), are shown.

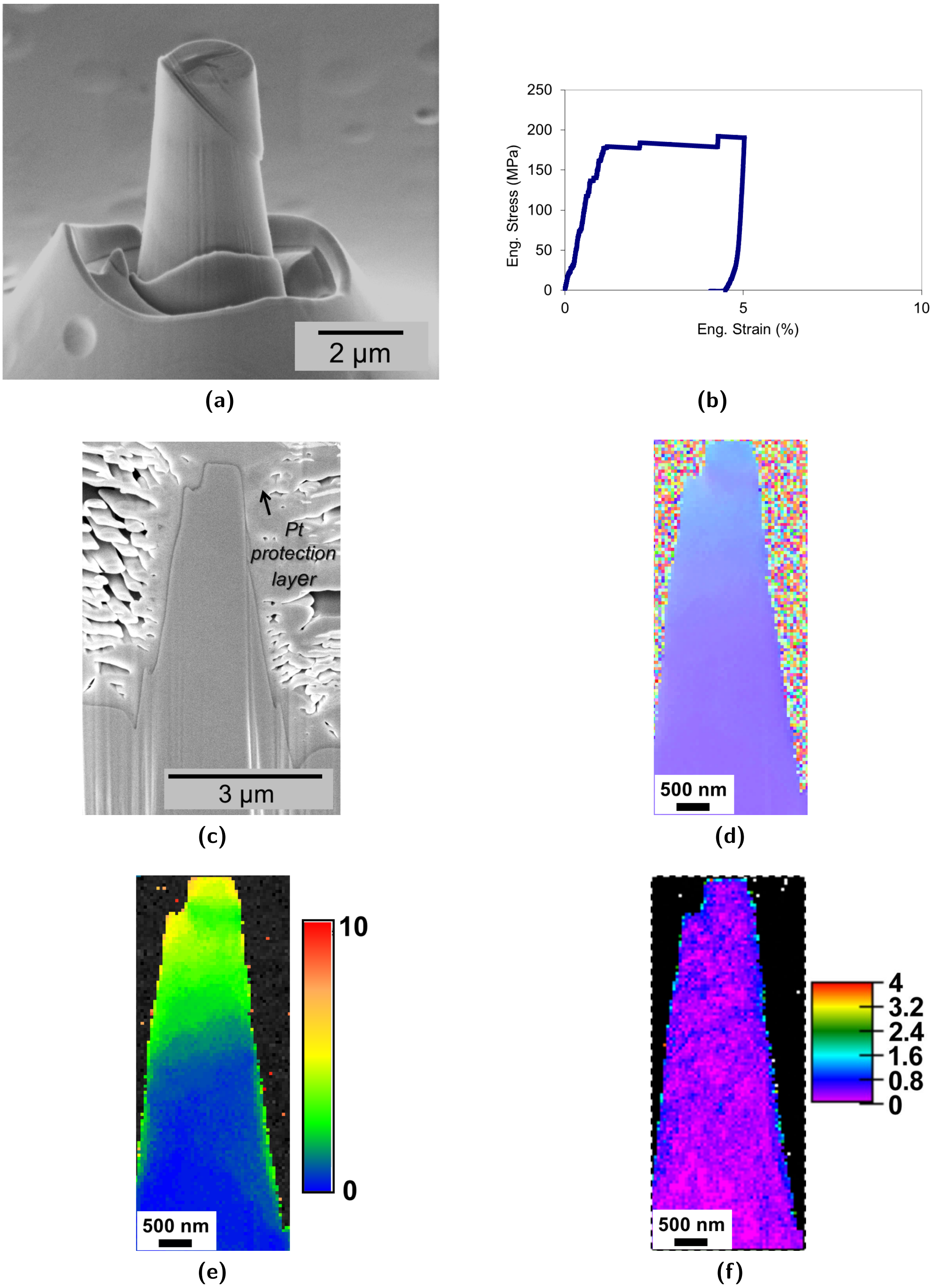

(a) (b) (c) (d) (e) (f)

Figure 5.33.: Misorientation analysis of the perfect shear. (a) SEM image of a single-crystalline micropillar with single slip orientation. (b) The engineering stress-strain curve of the pillar. (c) SEM image of the pillar cross section. (e) Misorientation analysis with respect to a reference point . (f) OGM analysis of the OIM map.

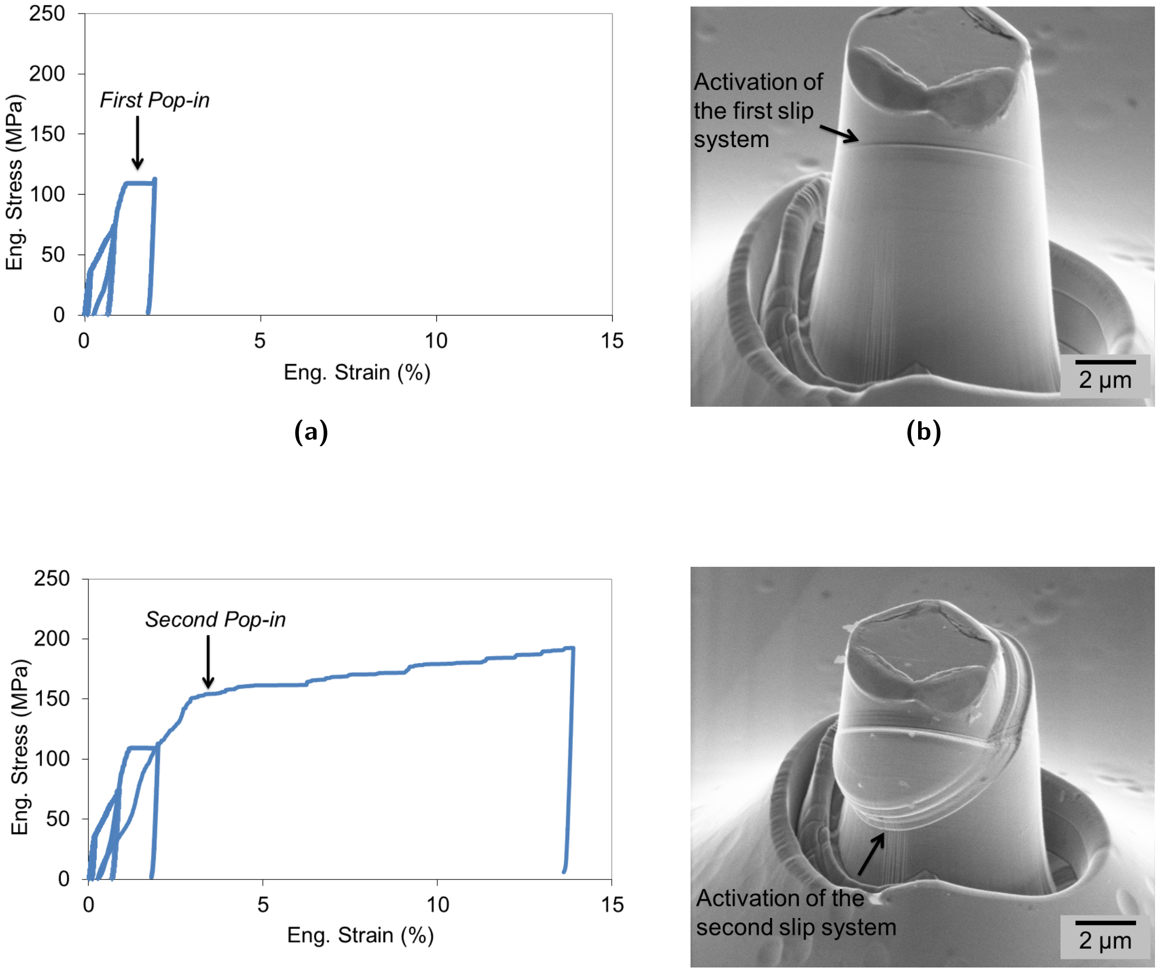

(a) **(b)**

(c) **(d)**

Figure 5.34.: Stepwise compression test of the single-crystalline pillar with double slip orientation shows that the first and the second pop-ins observed in the flow curve ((a) and (c)) are related to the activation of the two slip systems ((b) and (d)).

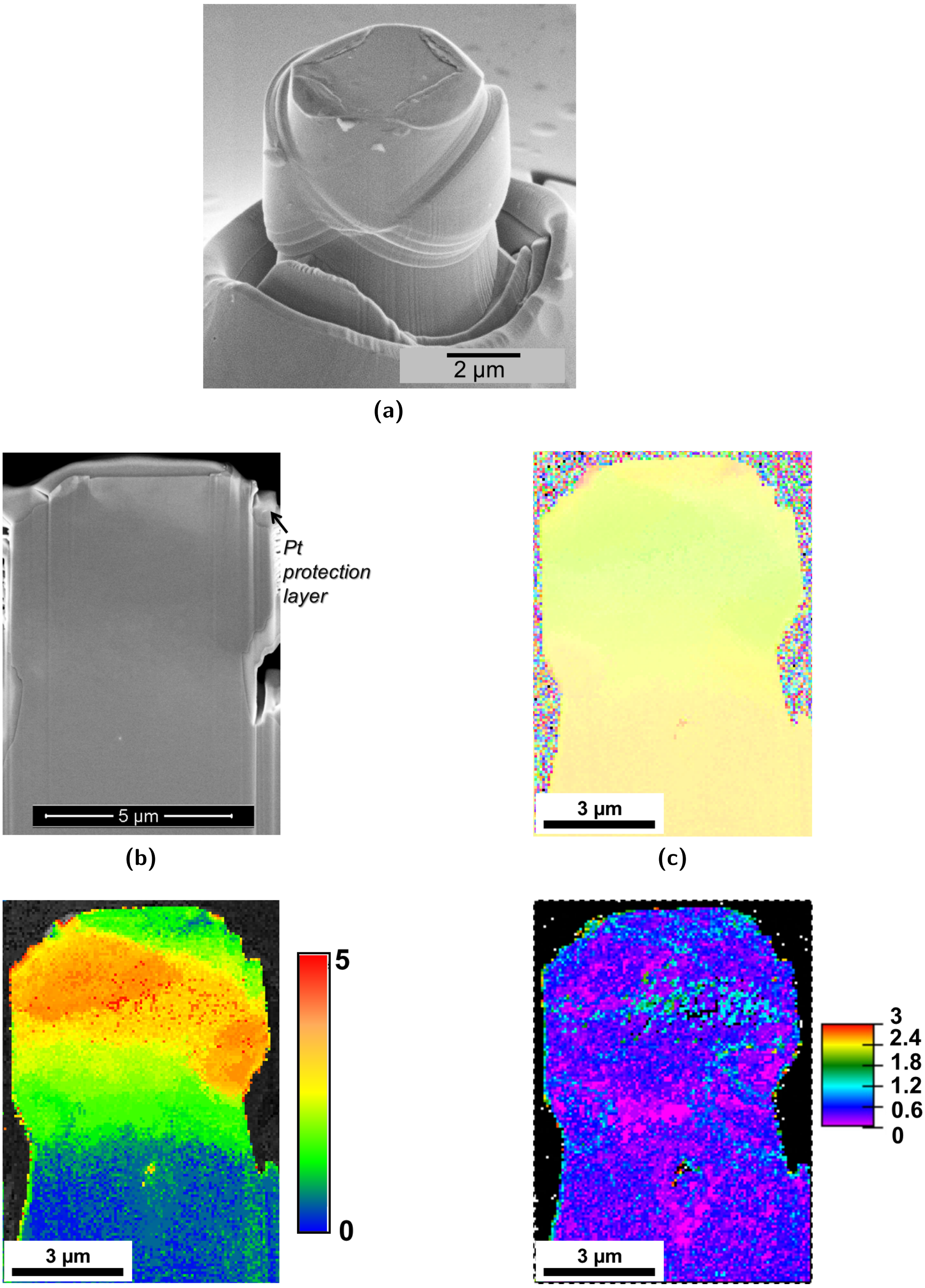

Figure 5.35.: Misorientation analysis of slip system interaction. (a) SEM image of a single-crystalline micropillar oriented for double slip. (b) SEM image of the pillar cross section. (c) OIM map of the cross section. (d) Misorientation analysis with respect to a reference point. (e) OGM analysis.

5.6.3. Inhomogeneous medium with the presence of a grain boundary

Large and small bicrystalline micropillars with diameters of 5 μm and 1 μm were analyzed for grain boundary-induced lattice rotation (Table 5.10). Two small bicrystals were highly deformed (35 and 21 %) and one small bicrystal was less deformed (0.5 %). In the latter bicrystal, the deformation was stopped directly after yielding.

Table 5.10.: Four bicrystals analyzed for grain boundary-induced lattice rotation in details.

Bicrystal (A/B)	$(h\ k\ l)_A/(h\ k\ l)_B$	Average Diameter/Length (μm)	Straining (%)
1	(1 5 3)/(-6 5 5)	5/13	12 %
2		1.1/2.6	35 %
3		0.95/2.2	21 %
4		1.3/2.6	0.5 %

1. Large bicrystal

   This bicrystal (Figure 5.36a) was deformed to 12 % strain (Figure 5.36b). The SE contrast image of the pillar cross section (Figure 5.36c), the OIM map (Figure 5.36d), the misorientation analysis with respect to an undeformed point (Figure 5.36e) as well as the OGM analysis (Figure 5.36f), are presented.

2. Small bicrystal 1

   This bicrystal (Figure 5.37a) was deformed to 35 % strain (Figure 5.37b). The SE contrast image of the pillar cross section (Figure 5.37c), the OIM map (Figure 5.37d) and the misorientation as well as OGM analysis (Figures 5.37e and 5.37f) are presented.

3. Small bicrystal 2

   This bicrystal (Figure 5.38a) was deformed to 21 % strain (Figure 5.38c). The SE contrast image of the pillar cross section (Figure 5.38b) and the OIM map (Figures 5.38d) of the pillar are presented. On the OIM map of this bicrystal, some pixels are not indexed correctly in the highly deformed areas due to the low pattern quality. These points are invalid and mislead the data analysis. The Confidence Indexes (CI) of these points are zero, so that a correction of these points by the “Neighbor CI Correlation” clean-up method is reasonable for a correct misorientation analysis. For our correction we defined the minimum CI to be 0.1. Further misorientation (Figure 5.38f) and the OGM analyses (Figure 5.38g) were performed on this corrected OIM map (Figure 5.38e).

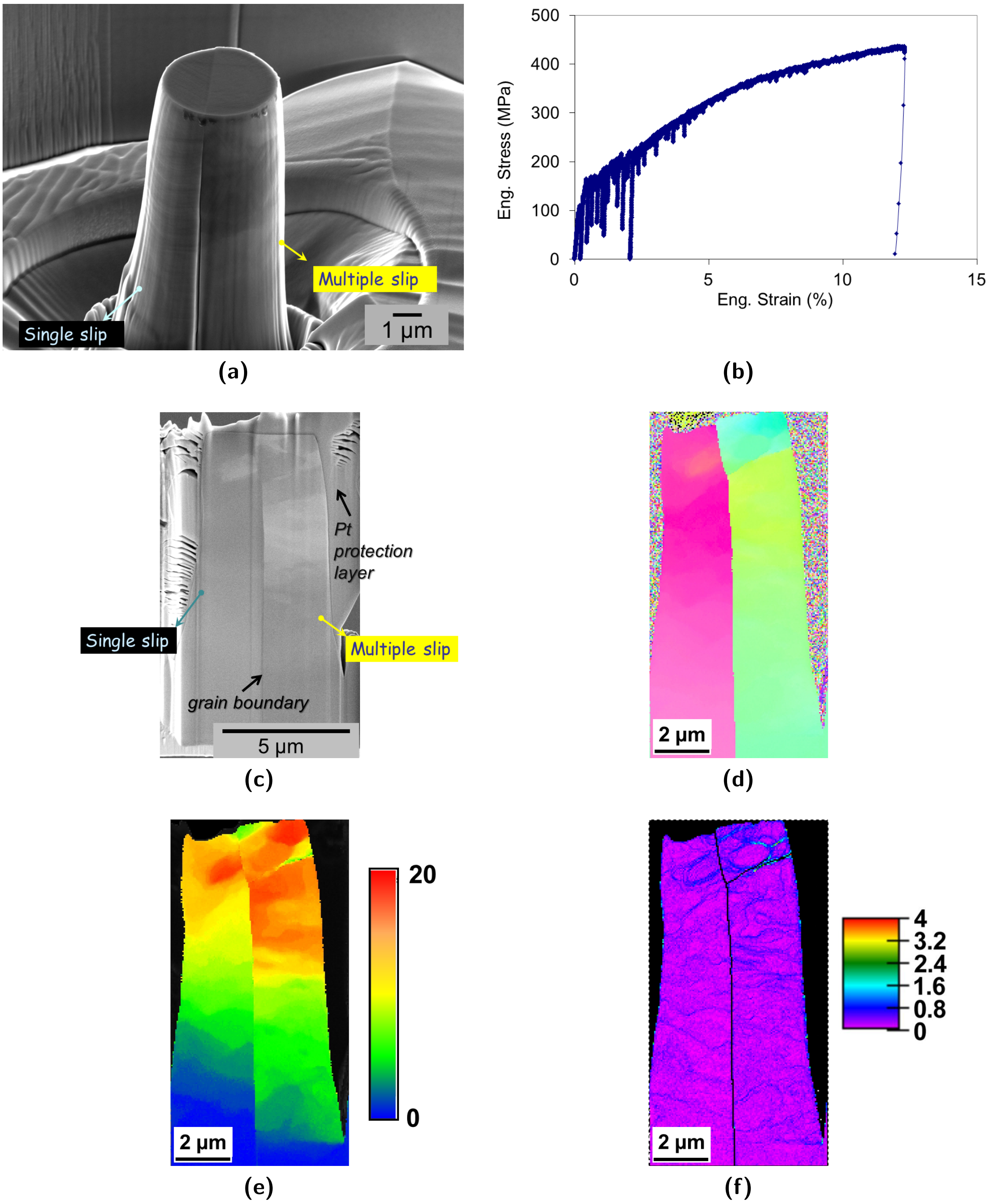

Figure 5.36.: (a) SEM image of the bicrystalline micropillar of 5 μm diameter. (c) SEM image of the pillar cross section. (b) The engineering stress-strain curve of the micropillar. (d) OIM map of the cross section. (e) Misorientation analysis with respect to a reference point. (f) OGM analysis.

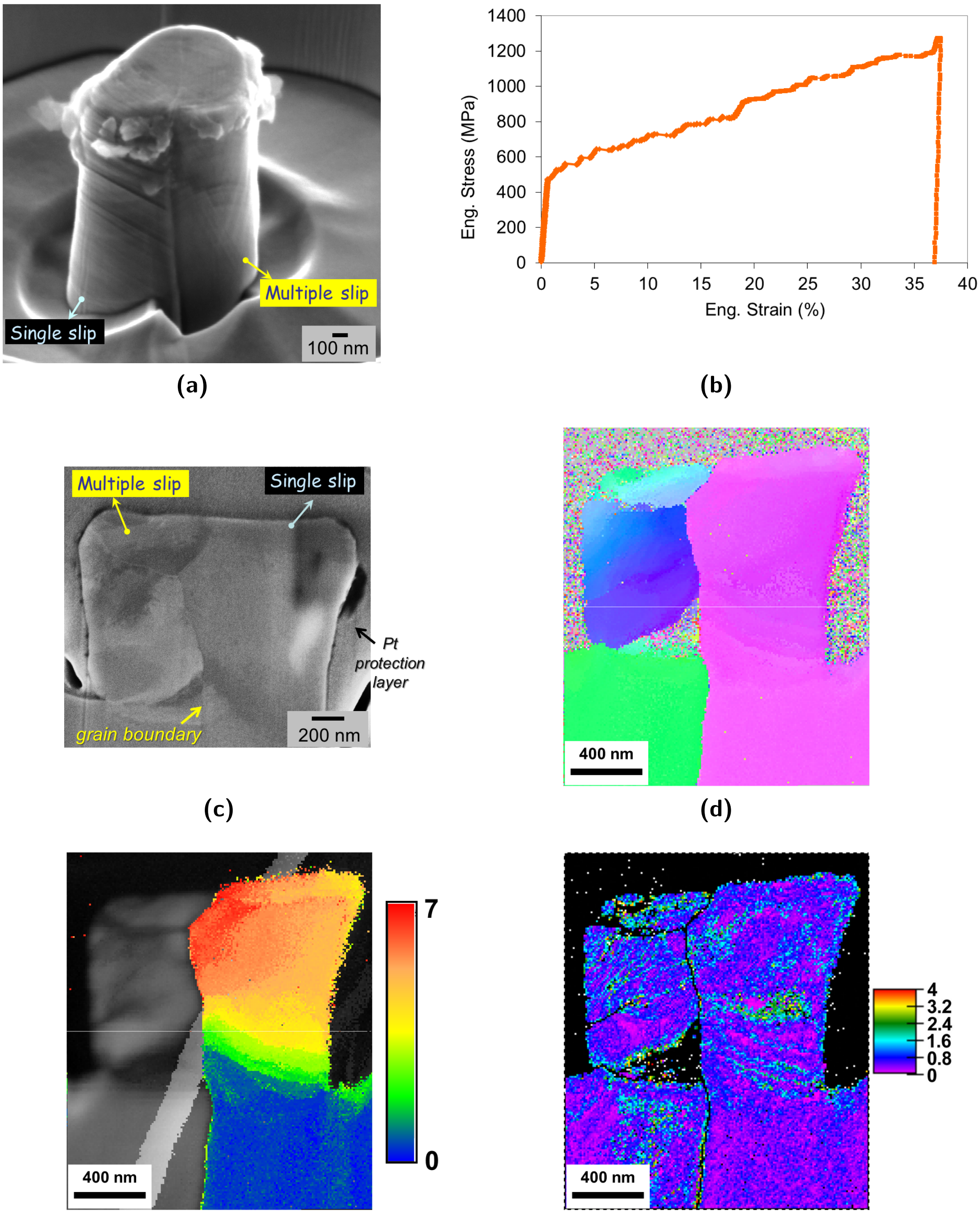

(a) **(b)**

(c) **(d)**

(e) **(f)**

Figure 5.37.: Investigation of dislocation-grain boundary interaction in small bicrystal 1. (a) SE contrast SEM image of a bicrystalline micropillar of 1 μm diameter. (b) The engineering stress-strain curve of the pillar. (c) SEM image of the pillar cross section . (d) OIM map of the cross section. (e) Misorientation analysis. (f) OGM analysis.

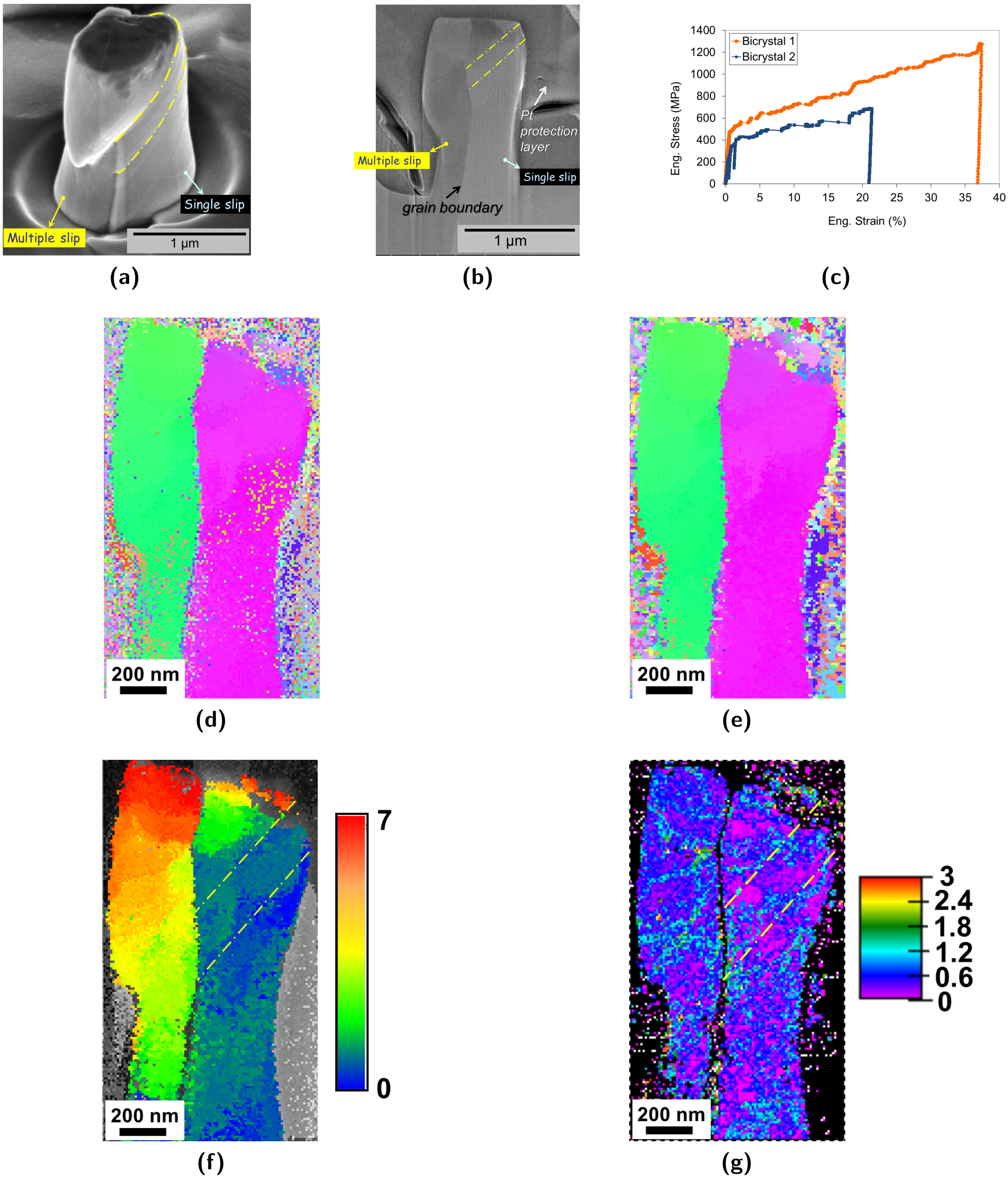

Figure 5.38.: (a) SEM image of the small bicrystal 2, of 1 μm diameter. The slip lines are indicated by dashed lines. (b) SEM image of the cross section from the film cut out of the pillar. (c) The engineering stress-strain compared to the small bicrystal 1. (d) OIM map of the cross section. (e) Corrected OIM map of the cross section. (f) Misorientation analysis with respect to a reference point. (g) OGM analysis.

4. Small bicrystal 3

   The final example of small bicrystalline micropillars (Figure 5.39) was deformed to only 0.5 % strain (Figure 5.39b). The SE contrast image of the pillar cross section (Figure 5.39c), the OIM map (Figures 5.39d) and the misorientation as well as OGM analysis (Figures 5.39e and 5.39f) are presented.

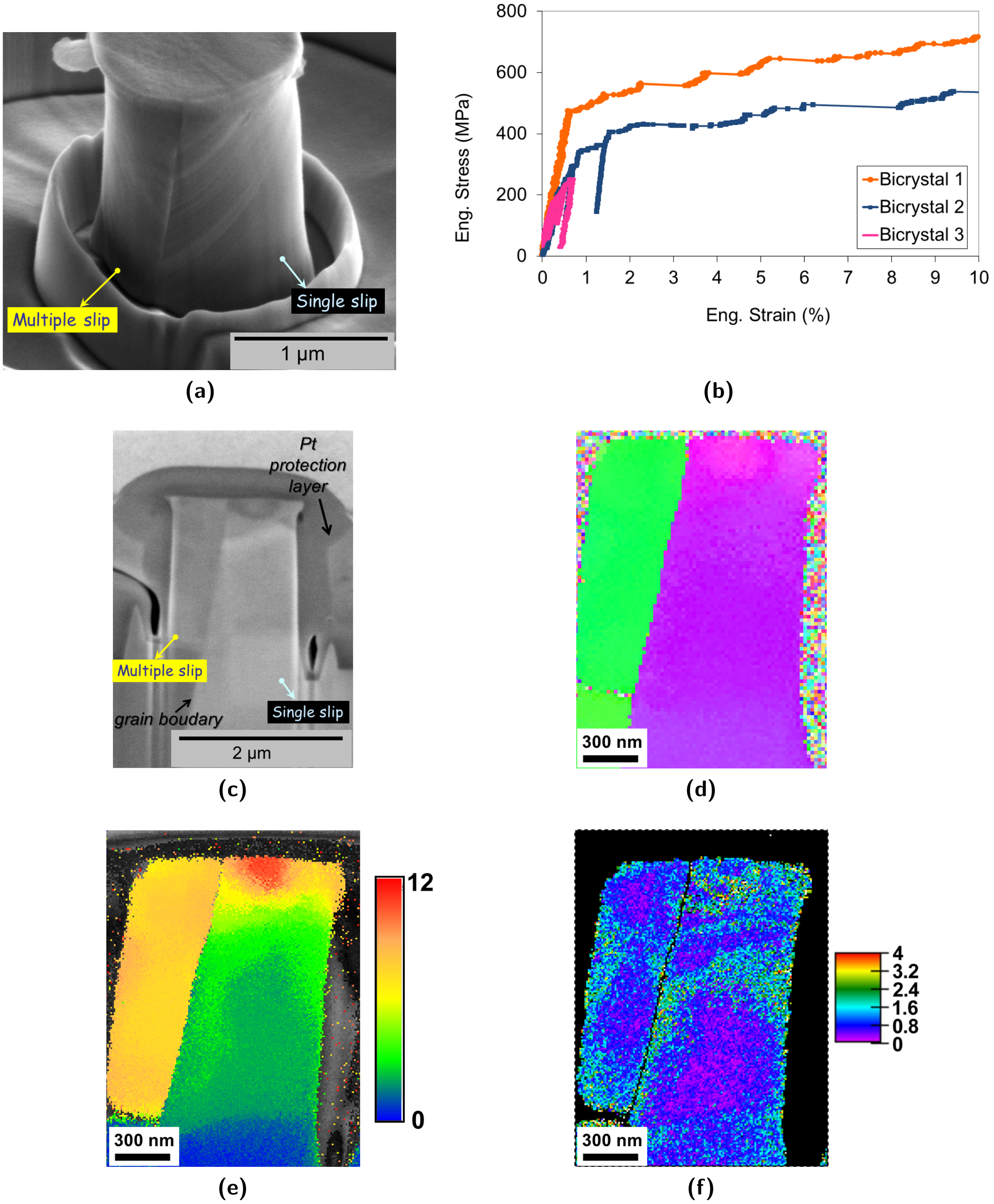

(a) (b)

(c) (d)

(e) (f)

Figure 5.39.: (a) SEM image of small bicrystal 3, of 1.3 μm diameter. (c) SEM image of the cross section from the film cut out of the pillar. (b) The engineering stress-strain curve compared to small bicrystals 1 and 2. (d) OIM map of the cross section. (e) Misorientation analysis with respect to a reference point. (f) OGM analysis.

5.7. Discussion on microstructural test results

Two component crystals of a bicrystal subjected to a load deform differently. One component crystal deforms plastically more than the other, so that gradients of deformation build up [*Ashby*, 1970]. Therefore, such a bicrystal is not only elastically incompatible (Appendix A), but also plastically incompatible. It was shown by Ashby that the gradients of deformation require GNDs be stored, that their arrangement and density can be calculated and that they contributed to the work-hardening of the bicrystal [*Ashby*, 1970]. The internal stress, averaged over a large distance compared with the separation of GNDs, is zero. GNDs or excess dislocations are required to support a particular curvature in the crystallographic lattice at any given point in a deformed structure. This array of dislocations is of one sign, in contrast to close pairs of dislocations, the statistically stored dislocations, which are of opposite sign and produce no curvature [*Nye*, 1953]. In the uniform deformation of a pure single crystal, the dislocations are not geometrically necessary [*Ashby*, 1970]. However, when a single crystal deforms by slip on a single set of parallel planes in such a way that the amount of slip is unevenly distributed over the slip planes the slip plane becomes curved [*Nye*, 1953]. This situation occurs by non-uniformly applied stress (e.g. bending test) or a non-homogeneous testing medium (e.g. existence of grain boundary or precipitations). In the absence of long-range elastic stress fields, Nye calculated an original formulation of the dislocation tensor:

$$\alpha_{ij} = e_{ikl} g_{jl,k} \tag{5.12}$$

where α_{ij} is the dislocation tensor, e_{ikl} are components of the permutation tensor and $g_{jl,k}$ the gradient in lattice orientation. From the Equation 5.12 a direct relationship between the measured crystallographic orientation gradient and the dislocation tensor is provided.

The different modes of deformation in homogeneous and inhomogeneous mediums were investigated and are discussed separately as follows.

5.7.1. Homogeneous medium with easy glide behavior

In a homogeneous medium (single crystal) and in the absence of a macroscopic strain gradient (uniaxial compression test), no GND-induced lattice rotation should be detected, since the dislocations can easily glide on their slip planes and exit the sample (Figure 5.33a). As a result, the top part of the pillar slips on the bottom part and the pillar has a new form with a larger diameter. Therefore, this single-crystalline micropillar was strained to only 5 % (Figure 5.33b), because above this strain range the compression test is actually performed on a new pillar. No strain hardening was observed in the flow stress curve. In misorientation analysis (Figure 5.33e), the lattice misorientation increases toward the top of the pillar but in a homogeneous way. This is because of the stress concentration on the top of the pillar due to the inevitable tapered form of the FIB-cut pillars. The results of FEM simulations also showed the stress concentration at this area (Appendix F). Further OGM analysis (Figure 5.33f) shows near-zero orientation gradient on the sample cross section. This is evidence for the absence of lattice rotation and, thus, the absence of excess dislocations in the lattice.

5.7.2. Homogeneous medium with the presence of non-planar dislocations

In the next step we chose a single-crystalline micropillar with a double slip orientation. In this homogeneous medium (single crystal) and in the absence of any inhomogeneities such as a grain boundary, a second phase or precipitations, and also the absence of a macroscopic strain gradient (uniaxial compression test), it is expected that no GND-induced lattice rotation should be detected, as observed in the case before (section 5.6.1). In this single-crystalline pillar with double slip orientation, however, a misorientation gradient appears in a strip along one of the activated slip systems (in agreement with the SEM observations, Figure 5.35a) from the upper-left to the lower-right (Figure 5.35d). The measured misorientation increases within the core region, where the two activated slip systems interact. The dislocation motion on one activated slip system will be disturbed by the activation of the second slip system, which results in dislocation storage in the lattice. The non-parallel dislocations on the two slip systems form junctions, such as Lomer-Cottrell locks. These dislocations, if they cannot be unzipped, for example by cross-slip [*Hirth and Lothe*, 1982; *Guruprasad and Benzerga*, 2008], are not glissile on any glide system of the lattice and provide a barrier for further dislocation glide through the material [*Buehler et al.*, 2005]. Other simulation work [*Kubin*, 1993] has already shown that in multiple slip, strong forest obstacles are concentrated at the intersections of the active slip planes. It is proposed that a non-vanishing local GND density emerges in microscopic domains as a result of the evolving dislocation structure (dislocation wall formation, cell closure and cell subdivision), although the imposed deformation is macroscopically homogeneous [*Guruprasad and Benzerga*, 2008; *Benzerga et al.*, 2004]. Arrays of GNDs are subsequently formed to accommodate local lattice rotations. Such arrays were called Geometrically Necessary Boundaries (GNBs) [*Benzerga et al.*, 2004]. The OGM analysis (Figure 5.35e) is a confirmation of the storage of GNDs in the intersecting zone of these two slip systems.

5.7.3. Inhomogeneous medium with the presence of a grain boundary

In this third case, the microstructure becomes more complicated and a grain boundary is introduced into the lattice. This inhomogeneous medium will be compared with single-crystalline micropillars as a homogeneous medium in oder to investigate the perturbing effect of the grain boundary. A second comparison is also made in terms of the size. The large ($5\,\mu$m diameter) and the small ($1\,\mu$m diameter) bicrystalline micropillars should display this. In the large bicrystal, the misorientation analysis (Figure 5.40b) shows misorientation gradients in the two component crystals from the bottom to the top of the pillar. In the component crystal with single slip orientation (left grain), the maximum misorientation is 15°, while in the component crystal with multiple slip orientation (right grain) it is 20°. A small region on the top of the component crystal with single slip orientation shows a misorientation of 20°. As explained previously, in this region, due to the direct contact with the flat-ended tip and the tapering of the pillar, the stress concentration and therefore the deformation rate are very high. Apart from this region, the misorientation change in the two component crystals is independent. The changes in lattice misorientation in the component crystal with single slip orientation resembles those of the single-crystalline pillar with single slip orientation (Figure 5.40a). The same situation is observed in the component crystal with multiple slip orientation. In the latter, a misorientation gradient is observed in the crystal interior. In this crystal, multiple slip systems are activated (as the SEM observations show in Figure 5.36a) and the interaction between them causes the lattice rotation induced by dislocation storage within the lattice. The OGM analysis to a maximum value of 4° in Figure 5.36f shows no clear orientation gradient. By decreasing the scale bar upper limit from 4° to 2° (Figure 5.41b) in the crystal interior, the misorientation gradients of 2° are observable in agreement with the observations in the single-crystalline micropillar with double slip orientation (Figure 5.41c). There, the interaction of the two activated slip systems caused the accommodation of non-vanishing local GNDs in the crystal lattice (see the discussion in section 5.7.2).

By comparison of the OGM maps of single-crystalline and bicrystalline micropillars, it can be seen that the component crystal with single slip orientation has the same OGM map as the single-crystalline micropillar with single slip orientation, and the OGM analysis of the component crystals with multiple slip orientation is similar to that of the single-crystalline micropillar with multiple slip orientation.

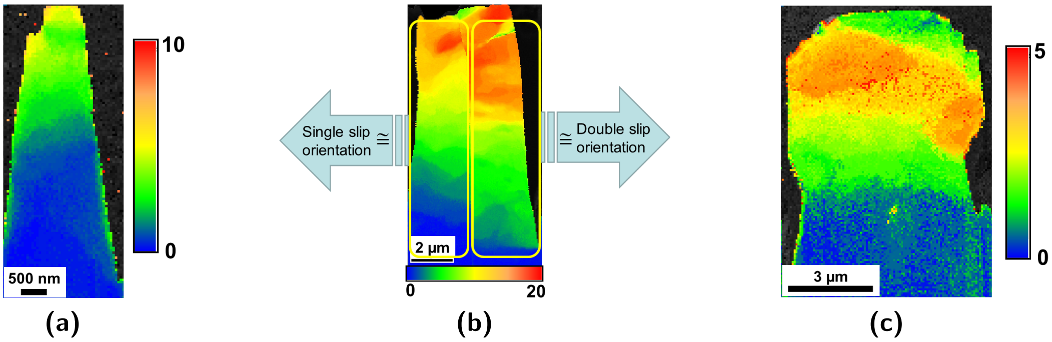

Figure 5.40.: Comparison of the misorientation changes between the component crystals of (b) the large bicrystal and the single-crystalline micropillars with (a) single slip and (c) with double slip orientations.

In small bicrystal 1 (Figure 5.37), the sample is deformed by activation of one slip system in crystal A and three slip systems in crystal B (Figure 5.37a). The flow curve (Figure 5.37b) shows the obvious work hardening effect of the grain boundary. On the cross section of the cut film (Figure 5.37c), the grain boundary is buckled. We believe that the incompatibly oriented grain on the left hinders the mobile dislocations in the right crystal. On the other hand, compatible deformation demands the accommodation

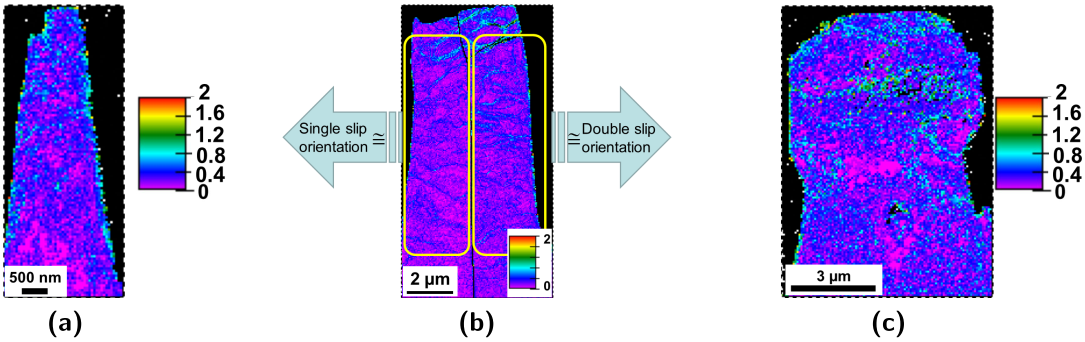

Figure 5.41.: Comparison of the OGM analysis between the component crystals of (b) the large bicrystal and the single-crystalline micropillars with (a) single slip and with (c) double slip orientations.

of GNDs. As a result, dislocations pile up at the grain boundary and cause the lattice rotation. Misorientation analysis (Figure 5.37e) reveals the high degree lattice misorientation at the buckled grain boundary, and the OGM analysis (Figure 5.37f) confirms the accumulation of dislocations, consisting of the sum of the same sign statistically stored dislocations and GNDs, in this region. In the multiple slip oriented crystal, the interaction of three slip systems, in addition to the constraint deformation of the crystals, results in high deformation and lattice rotation (Figure 5.37d). The orientation of a region at the bottom of the crystal near the grain boundary could not be evaluated with certainty by the automatic algorithm, possibly leading to an incorrect evaluation of the orientation results at these measurement points. Unevaluated orientation measurements lead to gaps in the orientation map. Often, those gaps are filled in after the measurement, e.g. by interpolation or using the orientation common to neighboring points. To avoid such artificial orientation gradient values here, such gaps are not closed [*Henning and Vehoff*, 2005]. The calculation of orientation gradients including such improper orientation measurements was omitted, and the corresponding points in Figure 5.37f are represented in black. The dislocation density distribution of both component crystals increases towards the top of the pillar, in the region with direct contact to the flat-ended tip. The resulting local misorientations in this area are explained by the formation of dislocation pile-ups at the specimen top due to constrained glide [*Kiener et al.*, 2008b].

In small bicrystal 2 (Figure 5.38), in the component crystal with single slip orientation (right grain), the lattice misorientation (and therefore dislocation density) decreases toward the pillar free surface along the slip band, as indicated by the dashed line in Figures 5.38a and 5.38f. The dislocations are eliminated when they reach the crystal free surface, creating a zone of depleted dislocation density there, and the largest step on the surface. In contrast, dislocation motion is hindered while approaching the grain boundary. As a result, the density increases because of the pile-up of dislocations. This can be observed along the grain boundary at the bottom of the pillar, where several slip systems have been activated and leave slip bands along the surface (Figure 5.38a). Compared to the rest of the crystal, the dislocation density is at its minimum on the slip band while transmitting the slip to the next crystal. This inhomogeneity of the dislocation density distribution can be related to the inhomogeneous distribution of dislocations.

The problems caused by high deformation which lead to the unevaluated orientation measurement, as observed in the two previous cases (Figures 5.37 and 5.38), disappear in small bicrystal 3 (Figure 5.39), where the bicrystal is only deformed to 0.5 %. At this strain the plastic deformation has already started and the accomodation of excess dislocations at the grain boundary is best observed in Figure 5.39f.

Chapter 6.

Conclusion and Outlook

6.1. Conclusion

In order to investigate the interaction of dislocations with a selected grain boundary and its strengthening effect as a function of the grain boundary type, a local mechanical testing method based on microcompression tests of FIB-cut bicrystalline micropillars was developed at the mesoscopic scale.

The method is used to study bicrystalline micropillars with the component crystals oriented for single slip and multiple slip as a soft/hard combination. Orientations identical to the experiment were used to generate models of the bicrystalline micropillars with up to four million atoms (140 nm in diameter). The compression tests on the models were simulated by means of Molecular Dynamics simulation and used empirical embedded atomic potentials. The simulation results were compared with the physical experiments and a detailed view of the process of slip transmission across the grain boundary was achieved.

The compression testing of these bicrystals was followed by EBSD measurements on bicrystal cross sections to investigate the crystal lattice rotations for a correlation with the excess dislocation density.

The single- and bicrystalline micropillars were prepared in FIB system using high-voltage ion beam, which interact with the host material and is referred to as the "FIB damage". In order to investigate the effect of FIB damage on the test results, the cross section of micropillars was measured by high-resolution EBSD at the near-free surface area. The abrupt increase of the local orientation gradient proved the emergence of a damaged layer on the pillar surface. The mechanical properties of this layer were investigated by nanoindentation, and the results show that the FIB damage is a function of the ion beam current and the crystallographic orientation of the lattice subjected to the ion beam. If the ions can implement in the lattice, then they form a hard layer on the surface; otherwise, they remove the material and produce a profile on the surface. In both cases the effect of the FIB damage is the introduction of surface defects and the facilitation of dislocation nucleation.

Different sized bicrystals from 1 to 5 μm diameters showed different deformation behaviors. In the large bicrystals with diameters 3 to 5 μm, flow stresses identical to those of single crystals with multiple slip orientation were obtained. These bicrystals resemble two single-crystalline micropillars connected in parallel, such that the component crystal with multiple slip orientation controls the plastic deformation, and the Taylor hardening is the mechanism responsible for deformation. From the diameter of 2 μm, the hardening effect of the grain boundary becomes pronounced, since the grain boundary-dislocation interaction plays a more crucial role than the dislocation-dislocation interaction. In such small bicrystals, due to the reduction of the grain size, the number of dislocations is limited compared to the large bicrystals. A prompt interaction of dislocations with the grain boundary leads to the pile-up of the same sign dislocations, of both statistically stored dislocations and GNDs, at the grain boundary, while the dislocations of the opposite sign exit the bicrystal free surface. According to Nye's theory, the accommodation of excess dislocations results in lattice rotation. Our EBSD measurements, and the consequent misorientation analysis with respect to the undeformed orientation and OGM analysis on 1 μm diameter bicrystal cross sections, proved the existence of lattice rotation in the vicinity of the grain boundary. In the former misorientation analysis method, the misorientation gradient increasing into the crystal is evidence of the accommodation of excess dislocations, and in the OGM analysis method the increasing local orientation gradients. In contrast, in a large bicrystalline micropillar with a 5 μm diameter, the lattice misorientation changes only in the bottom-up direction, parallel to the loading axis. Absence of the local orientation gradients within the the OGM analyses of the component crystals are clear evidences for the explanation about the independent deformation of the adjacent crystals as connected in parallel.

In agreement with the literature, it was observed that lattice rotation is required for slip transmission and, thus, for compatible deformation of the bicrystals. According to our experiments and MD simulations, the slip transmission across the studied grain boundary occurs on a primary slip system in the adjacent crystal. Thereby, no additional stresses are required for the activation of the secondary slip system to fulfill the compatibility conditions. Hence, the increased stresses of bicrystalline micropillars with diameters lower than 2 μm are a result of the effect of the grain boundary as a barrier for dislocation motion and the origin of the strain gradient plasticity.

6.2. Outlook

The presented local study, as a function of the grain boundary type at the mesoscopic length scale, followed by direct observations in SEM make the technique a powerful tool to study different features of a grain boundary. This technique can be improved, both for further studies on the deformation mechanisms and also the environmental effects, by using the following possibilities.

6.2.1. Determination of the grain boundary strength

For compatible elastic and plastic deformation of bicrystals, four independent slip systems are required to be activated. It is proposed that the activation of secondary slip systems in addition to primary slip systems requires higher stresses. In the present study, the component crystals provided the required four slip systems so that this parameter was excluded as a reason for high stresses. In this way, any changes in the flow stress of bicrystals in comparison to single crystals was related to the effect of the grain boundary. The same procedure can be used for grain boundaries whose component crystals slip on only a single slip system. Then, the required stress for compatible deformation of the bicrystal is expected to be higher than that of single crystals, even in large bicrystals.

Changing the relative misorientation of the component crystals results in changes in the geometry of the potential slip planes, and therefore, in the angle θ between their intersection lines on the grain boundary plane. Altering this angle controls the slip transmission from one grain to the next one, as a crucial deformation mechanism and an effective factor on the flow stress. Therefore, it is possible to measure the grain boundary strength while changing θ.

6.2.2. In-situ compression tests

Previous studies on macroscopic bicrystals introduce slip transmission as the point where the bicrystals start to yield. Due to experimental limitations we were not able to resolve the slip transmission at yield point. The in-situ compression tests of bicrystalline micropillars would be a possibility to prove this mechanism.

6.2.3. Hydrogen embrittlement

The developed local mechanical tests in nanoscale inside a solution, under electrochemical control, with in-situ imaging possibility by Barnoush and Vehoff [*Barnoush and Vehoff*, 2008] in combination with the present study on grain boundaries, provides new insight for the investigation of the grain boundary effect on hydrogen embrittlement.

Appendix A.

Compatibility conditions

Consider the bicrystal shown in Figure A.1 discussed by [*Hook and Hirth*, 1967a; *Livingstone and Chalmers*, 1957; *Hauser and Chalmers*, 1961]. The continuity of strain across the xz grain boundary is represented by the following relationships:

$$\epsilon_x^A = \epsilon_x^B, \quad \epsilon_z^A = \epsilon_z^B, \quad \gamma_{xz}^A = \gamma_{xz}^B \tag{A.1}$$

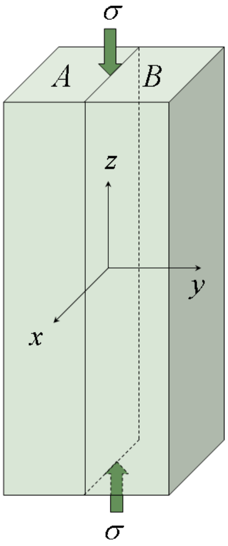

Figure A.1.: Bicrystal geometry employed in [*Hook and Hirth*, 1967a,b; *Livingstone and Chalmers*, 1957; *Hauser and Chalmers*, 1961].

These strain components suffice to describe the deformation of the boundary plane. The other strain components may be important when considering the effects of end constraints but do not affect the deformation of an arbitrary boundary. In addition to these three independent relations, a fourth relation is specified by experiment, namely the value of ϵ_z. Hence, in general, the operation of four slip systems is required for deformation of the A-B bicrystal.

When a bicrystal is subjected to a uniaxial stress σ in the elastic range, one of the compatibility relations specified in Equation A.1 is satisfied ($\epsilon_z^A = \epsilon_z^B$), but the remaining two are not likely to be satisfied. Thus, the two component crystals will be elastically incompatible. One would expect that this elastic incompatibility result in the development of local stresses depending on the degree of incompatibility and the amount of the applied stress. If the elastic incompatibility is big enough it could result in the development of stresses which add to the applied resolved shear stress and result in slip locally along the grain boundary. Elastic incompatibility applies to both isoaxial (the two crystals have the same crystallographic orientations along the tension axis) and non-isoaxial bicrystals of an anisotropic material. In the first case, the isoaxial bicrystal, if the compliance matrices of the component crystals do not match, even when the crystals are equally stressed, elastic incompatibility occurs, producing local stresses which in turn results in slip at the grain boundary. In the second case, the non-isoaxial bicrystal, under a condition of uniform axial elastic strain, the component crystals of a non-isoaxial bicrystal are not equally stressed, again resulting in elastic incompatibilities at the grain boundary. The ratio of the applied stress is proportional to the ratio of elastic moduli of the two component crystals in the axial direction.

Appendix B.

Prime criteria on slip transmission

Three basic criteria based on macroscopic bicrystal deformation and microscopic TEM observations are proposed in the literature to predict the slip transfer. These criteria predict the activated slip systems in the next grain as a result of the slip transmission.

1. Classical geometric condition: Livingstone and Chalmers [*Livingstone and Chalmers*, 1957] showed that for a pure shear stress the transmission parameter for a certain slip system can be expressed as

   $$N = (e_1 \cdot e_i) * (g_1 \cdot g_i) + (e_1 \cdot g_i) * (e_i \cdot g_1) \tag{B.1}$$

   where the dislocation pile-up lies in a slip plane with the normal e_1 and slip direction g_1, while e_i and g_i are the plane normal and slip direction in the next grain (Figure B.1a). All of the above terms are unit vectors. The operative slip system is predicted to be that for which N is a maximum. This criterion is only derived from the geometric relationship between the two component crystals. However, it is lacking in the consideration of the accommodation between incoming and outgoing dislocations on the grain boundary plane [*Kashihara and Inoko*, 2001]. This criterion was never satisfactory in the observations of Shen et al. [*Shen et al.*, 1988] and Clark et al. [*Clark et al.*, 1992].

2. Geometric and resolved shear stress condition: Shen at al. [*Shen et al.*, 1986, 1988] proposed a criterion to take account of the conditions of, not only the angle relation between the slip plane normals and slip directions in both component crystals, but also the angle relation between the line directions of the incoming and outgoing dislocations at a grain boundary. This criterion is expressed as follows:

   $$M = (L_1 \cdot L_i) * (g_1 \cdot g_i) \tag{B.2}$$

   where L_1 and L_i are the lines of intersection between the grain boundary and the slip planes of the pile-up and emitted dislocations, and g_1 and g_i are slip directions in the pile-up and next grains, respectively(Figure B.1b). The plane which minimizes the angles between the intersection lines is chosen as the favored slip plane. For this slip plane, the factor M should be maximized. In order to predict the slip direction, the force calculated from the Peach-Koehler Equation (Equation B.3), acting on a dislocation emitted from the pile-up, is applied.

$$F = (b \cdot \sigma) \times \xi \tag{B.3}$$

F is the force per unit length exerted on the emitted dislocation, b and ξ are the Burgers vector and line direction of the emitted dislocation, and σ is the stress tensor of the dislocation pile-up at the test dislocation site [*Shen et al.*, 1988]. The slip direction on which the force exerted for slip propagation is maximized, is the favored slip direction. Figure B.1 shows the difference between the two mentioned criteria.

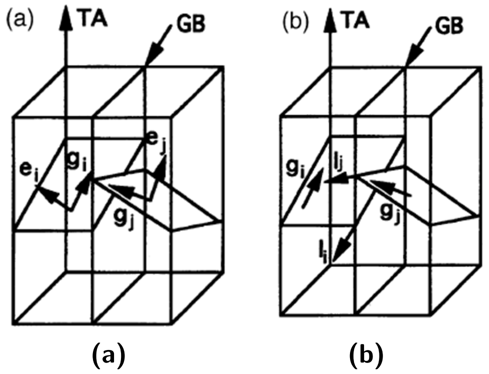

Figure B.1.: Pictured transmission criteria proposed by Livingstone (a) and Shen (b) [*Kashihara and Inoko*, 2001].

This criterion was not able to predict the slip system correctly in all the experiments analyzed. Finally a third criterion, incorporating both the grain boundary geometry and the anisotropic elastic stress field, was found to be satisfactory in all the observed cases [*Clark et al.*, 1992].

Appendix C.

Orientation characterization in OIM software

In general, rotation about a given axis $u = (u_x, u_y, u_z)$, where $u_x^2 + u_y^2 + u_z^2 = 1$, by an angle of θ is given by the rotation matrix $R_u(\theta)$.

$$R_u(\theta) = \begin{pmatrix} cos\theta + u_x^2(1 - cos\theta) & u_x u_y(1 - cos\theta) - u_x sin\theta & u_x u_z(1 - cos\theta) + u_y sin\theta \\ u_x u_y(1 - cos\theta) + u_z sin\theta & cos\theta + u_y^2(1 - cos\theta) & u_y u_z(1 - cos\theta) - u_x sin\theta \\ u_x u_z(1 - cos\theta) - u_y sin\theta & u_z u_y(1 - cos\theta) + u_x sin\theta & cos\theta + u_z^2(1 - cos\theta) \end{pmatrix}$$

This form of rotation can be used to describe misorientation of any kind; for example the misorientation of the crystal coordinate system relative to the sample coordinate system, or the misorientation of two orientations relative to each other. In the former case, in order to describe the crystallographic orientation of each crystal, three rotation matrices of this kind must be multiplied successively. These three rotations are defined by Euler angles, (ϕ_1, Φ, ϕ_2) (notation after Bunge) about z, $x^{'}$ and $z^{''}$ axes, respectively. These rotations are required to bring the principle axes of the crystal into coincidence with the principle axes of the sample. Other descriptions are available to represent orientation. These have their own sets of advantages and disadvantages. The Euler angle approach is used primarily due to convention. Another common description is the $\{h\ k\ l\}\langle u\ v\ w\rangle$ representation, where $\{h\ k\ l\}$ is the crystal plane perpendicular to the sample normal and $\langle u\ v\ w\rangle$ is the crystal direction aligned with the "RD" axis of the sample [*TSL and EDAX*, 2001] (Figure C.1).

The rotation given by Euler angles is given by the rotation matrix:

$$R_z(\phi_1)R_{x'}(\Phi)R_{z''(\phi_2)} = \begin{pmatrix} cos\Phi cos\theta - cos\theta sin\phi sin\Phi & cos\Phi sin\phi + cos\theta cos\phi sin\Phi & sin\Phi sin\theta \\ -sin\Phi cos\phi - cos\theta sin\phi sin\Phi & -sin\phi sin\Phi + cos\theta cos\phi sin\Phi & cos\Phi sin\theta \\ sin\theta sin\phi & -sin\theta cos\phi & cos\theta \end{pmatrix}$$

The latter case is used in the OIM data analysis software to generate the lattice misorientation analysis map. There, instead of the sample coordinate system, the orientation of a reference point (defined by the user) is used. The misorientation data will be shown as a rotation angle ω about an axis $\vec{d}$. This is another form of description of an orientation, called Angle/Axis [*TSL and EDAX*, 2001], and is defined as follows.

$$d = (d_1, d_2, d_3)$$

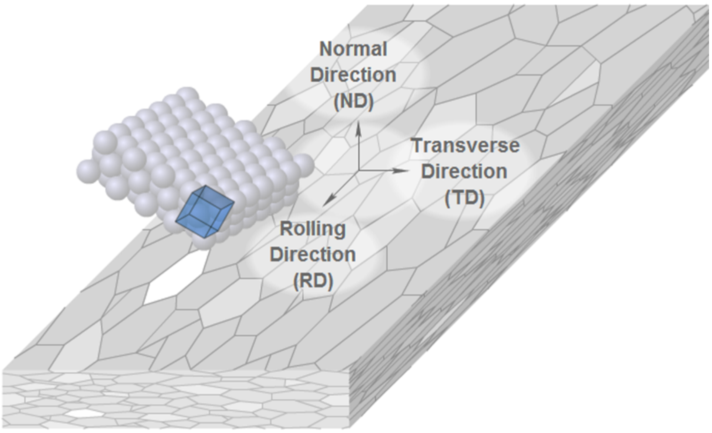

Figure C.1.: The position of the crystal coordinate system of a typical grain relative to the sample coordinate system. The sample coordinate system is defined by three axes named RD, TD and ND. The image is captured from the web site *Collaborative Open Resource Environment-for Materials* (http://core.materials.ac.uk/search/detail.php?id=2619)

$$R = \begin{pmatrix} (1-d_1^2)cos\omega + d_1^2 & d_1d_2(1-cos\omega) + d_3sin\omega & d_1d_3(1-cos\omega) + d_2sin\omega \\ d_1d_2(1-cos\omega) - d_3sin\omega & (1-d_1^2)cos\omega + d_2^2 & d_2d_3(1-cos\omega) - d_1sin\omega \\ d_1d_3(1-cos\omega) - d_2sin\omega & d_2d_3(1-cos\omega) - d_1sin\omega & 1-d_1^3)cos\omega + d_3^2 \end{pmatrix}$$

$$2cos\omega = Trace(R) = R_{11} + R_{22} + R_{33} - 1$$

The angle ω shows the misorientation about the axis which the two orientations have in common. As the misorientation gradient is measured for one crystal, the common axis of all measured points is the normal of that crystal surface. As an example, the Angle/Axis rotation of the deformed lattice with respect to the undeformed lattice point-by-point for a single-crystalline micropillar is shown in Figure C.2. The misorientation angle of each measured point is shown on the OIM map (Figure C.2a). The misorientation values are represented by colors and can be read from the scale bar. The rotation axes that these points have in common are shown on the inverse pole figure (Figure C.2b) and are parallel to the surface normal. For comparison, the surface normal is shown in Figure C.2c.

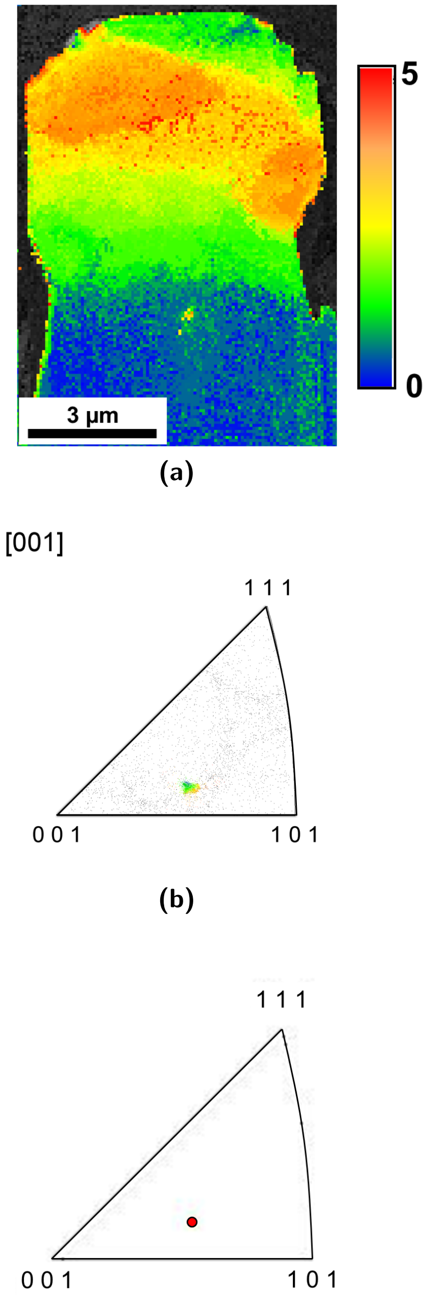

(a)

(b)

(c)

Figure C.2.: An example to show the Angle/Axis description. (a) The rotation angles are shown on the OIM map. (b) The rotation axes are shown in the inverse pole figure. The comparison with the crystal surface normal shown in (c) shows that the rotation axes are the same as the normal.

Appendix D.

Investigation of FIB damage by nanoindentation

In order to characterize the FIB-induced damaged layer, we sputtered several regions of the surface of a nickel sample with (1 1 1) orientation by altering the ion current and incidence angle (Figure D.1). We performed nanoindentation on each of these sputtered regions using three different loads. These parameters are listed in Table D.1.

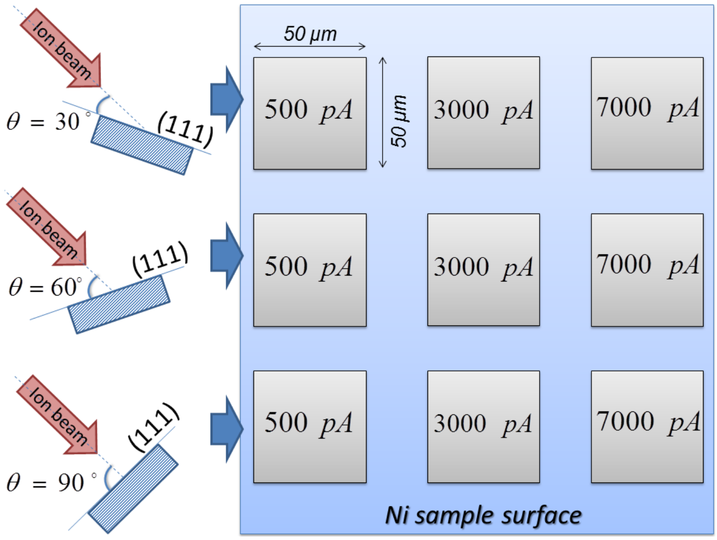

Figure D.1.: Schematical drawing of the Ni sample surface sputtered by different ion currents and at incidence angles.

Table D.1.: Parameters varied for the nanoindentation of FIB-damaged layers.

Parameters	Values
Ion beam current (pA)	500, 3000, 7000
Ion beam incident angle (degree)	30, 60 and 90
Indentation load (μN)	100, 200, 300

The results of the nanoindentation of the regions damaged by 7000 pA show that the hardness of the FIB-induced damaged layer is higher than the electropolished (EP) surface for all three incident angles (Figure D.2a). This regularity was not observed in the 3000 pA ion current results (Figure D.2b). The hardness for the 90° incidence angle is lower than for the electropolished surface. At 500 pA (Figure D.2c) this irregularity and the high scattering in the data is more pronounced for the 30° incidence angle. We studied the reason more precisely with the help of in-situ imaging capability of the nanoindentation system. In Figure D.3 the topography images of these irradiated regions are shown. The surfaces subjected to all of the used ion currents at 30° and 90° show a clear wavy profile. At 60° this was only observed for the 500 pA ion current and for the other 3000 and 7000 pA ion currents the surface becomes more homogeneous and the profile vanishes. On a wavy profile layer, the nanoindentations are made randomly either on the hills or on the valley of the wavy surface, and high data scatter is obtained (as observed for 500 pA irradiated at 30°). If the nanoindentation depth remains smaller than this profile thickness, lower hardnesses will be achieved, since the formed profile is softer than the electropolished Ni sample surface (as observed for 500 and 3000 pA irradiated at 90°). However, for all of the ion beam currents used, the hardness is the largest for the incidence angle of 60°. This shows the orientation dependence of the FIB damage. To explain this phenomenon, we may consider the crystallographic orientation of the indented sample. In the frontal incident angle, the ions hit the lattice plane with (1 1 1) orientation (Figure D.1). Rotating the sample surface while the ion direction remains constant, changes the lattice plane frontal to the ion beam. At 60° the (1 1 0) planes, which have a planar density of 8.54 atoms/nm^2 in comparison to the (1 1 1) planes with a planar density of 17.43 atoms/nm^2, are frontal to the incident ion beam. This implies that under a 60° incidence angle, more ions enter into the material, damage it and form a layer with a higher hardness than Ni hardness in its electropolished state.

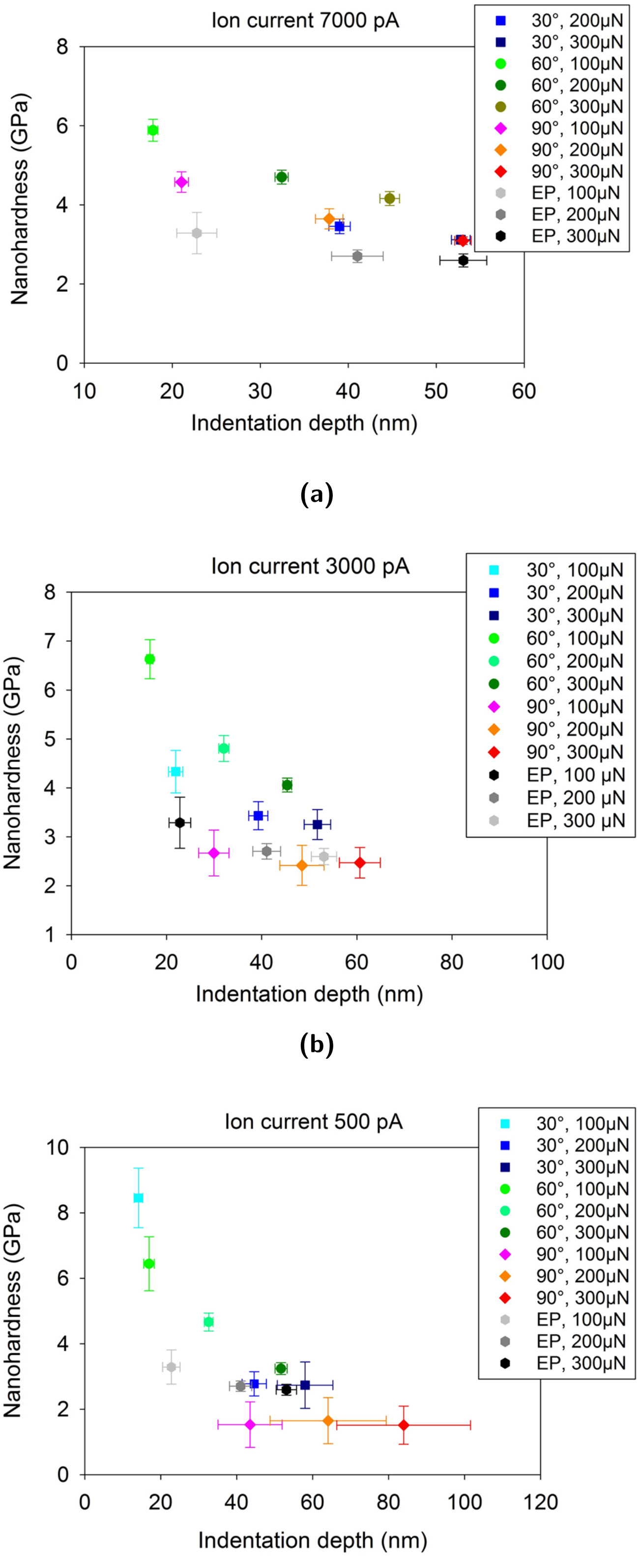

(a)

(b)

(c)

Figure D.2.: Nanoindentation results with varying loads on surfaces irradiated with different ion beam currents.

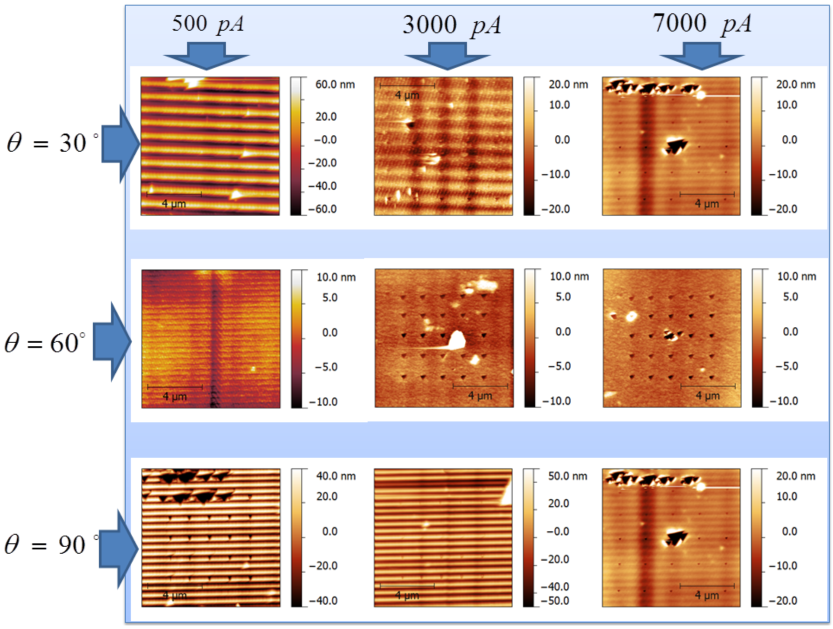

Figure D.3.: Topography images of the irradiated regions with the help of in-situ imaging capability of the nanoindentation system.

Appendix E.

Strain rate sensitivity of bicrystalline micropillars

In order to investigate the effect of different loading process modes of the bicrystalline micropillars, we performed strain rate sensitivity tests. For this, compression tests were performed systematically by varying the strain rate the same-size bicrystalline micropillars (average diameter 1.4 μm). The strain rates were 0.1, 1 and 10 nm/s. The engineering stress-strain curves of some of the samples are presented here (Figures E.1a, E.1b and E.1c) and are compared in Figure E.1d. In Figure E.1a, a bicrystalline micropillar of 1.4 μm diameter was loaded and unloaded by altering the loading rate from 0.1 nm/s, referred to as “slow”, to 10 nm/s, referred to as “fast”, in several successive steps. In Figure E.1b, a similar bicrystal was deformed using the same loading rates in one loading step. Another two similar bicrystals were deformed in one step using a constant loading rate of 1 nm/s. A comparison of these differently loaded samples (Figure E.1d) shows no strain rate sensitivity of bicrystalline micropillars. Absence of the strain rate sensitivity in these complementary tests supports that there is no difference between the load-controlled and displacement-controlled compression test data. However, because of the strain rate sensitivity observed in nanocrystalline and ultrafine grained materials in the literature, e.g. via nanoindentation tests, we expected to observe different behaviors when varying the loading rate. Therefore, these discrepancies are the motivation behind the investigation of strain rate sensitivity mechanisms. Possible experiments which can be used for further studies on this topic are: further reducing the dimension of the bicrystals to promote the interaction of dislocations with the grain boundary; increasing the loading rates with the help of the newly developed Hysitron® Performech™ Control Unit; and performing compression tests on the FIB-cut nanocrystalline and ultrafine grained micropillars.

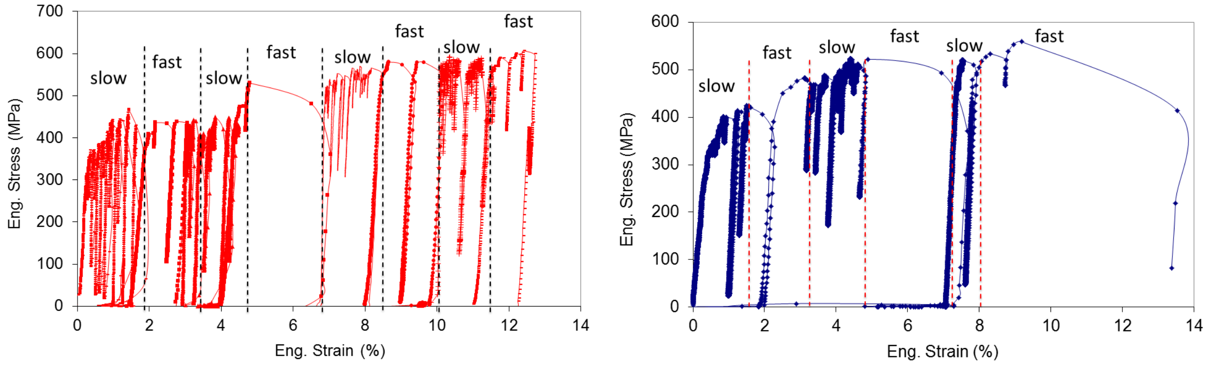

(a) Strain rate altering from 0.1 to 10 nm/s in *several successive* loading steps.

(b) Strain rate altering from 0.1 to 10 nm/s in *one* loading step.

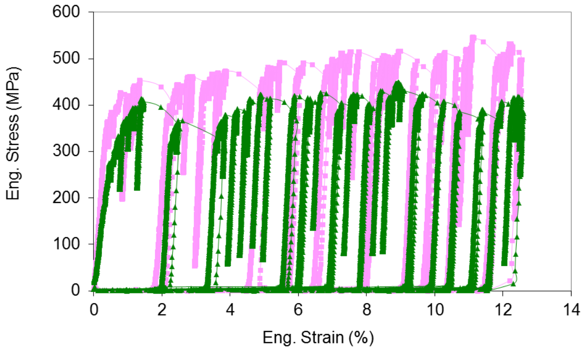

(c) Constant strain rate of 1 nm/s in *one* loading step for two individual bicrystalline micropillars.

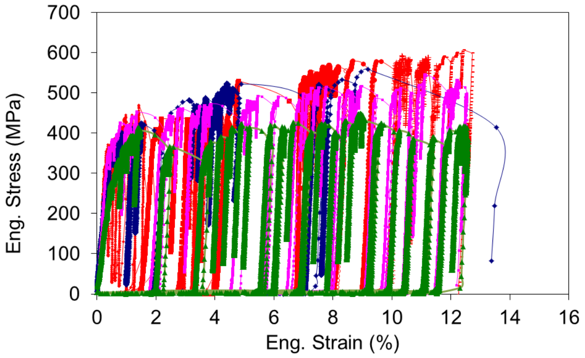

(d)

Figure E.1.: (a),(b) and (c) Some typical results of the strain rate sensitivity compression tests on bicrystalline micropillars of the same size. (d) Comparison of the results show no strain rate sensitivity in bicrystalline micropillars of this size can be observed.

Appendix F.

Finite Element Simulation

An inevitable problem with FIB milling of micropillars is the tapered form of the pillars and thus the deviation of the pillar from the ideal cylinder form. Although this problem could serve as an advantage for pillar stability by hindering the eventual buckling of pillars under the flat punch indenter, the stress distribution in these two different geometries is rather different. Finite element simulation was used to investigate this difference. Figure F.1 shows the stress distribution in these two geometries in the elastic regime. For both samples, a single slip orientation was chosen and their top surface diameters are $5\,\mu$m.

The simulations show that in pillars with a tapered form the stress concentration starts from the top of the pillar and will be distributed to the pillar bottom. The stress concentration is the highest at some places near the top surface. Experiments on the single-crystalline micropillar with the same size and orientation shows that the plastic deformation also starts at the same area as in simulations. Results of a pillar with no tapering shows that the stress distribution in an ideal cylindrical geometry is homogeneous. The stress concentration is not limited to the top area of the pillar, but also starts from the bottom corners of the pillar, where the pillar joins the bulk material. This shows that the form of the pillar influences the stress distribution and the plastic behavior of samples. It is noteworthy that the microscopic pillars studied in this work were all fabricated in FIB, which produced a tapered form in all of them.

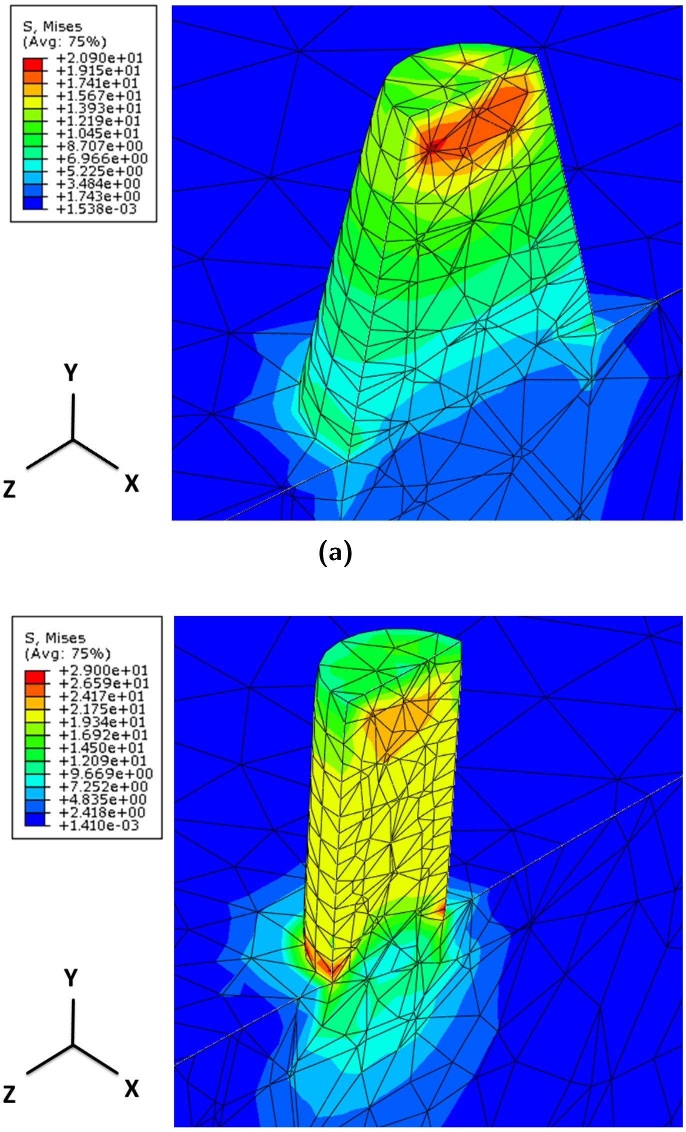

(a)

(b)

Figure F.1.: Stress distribution in different pillar geometries. (a) A tapered pillar. (b) An ideal cylinder with no tapering.

Bibliography

www.ntmdt.com/spm-basics/view/effect-tip-radius-cone-angle.

Afrin, N., and A. Ngan, Creep of micron-sized Ni3Al columns, *Scripta Materialia*, *54*(1), 7 – 12, 2006.

Ashby, M. F., The deformation of plastically non-homogeneous materials, *Philosophical Magazine*, *21*, 399–424, 1970.

Aust, K. T., and N. K. Chen, Effect of orientation difference on the plastic deformation of aluminum bicrystals, *Acta Metallurgica*, *2*, 632, 1954.

Baillin, X., J. Pelissier, J. J. Bacmann, A. Jacques, and A. George, Dislocation transmission through $\sigma=$ 9 symmetrical tilt boundaries in silicon and germanium, *Philosophical Magazine A*, *55*, 143–164, 1987.

Baillin, X., J. Pelissier, A. Jacques, and A. George, Direct evidence of dislocation transmission through $\sigma=$ 9 grain boundaries in germanium and silicon by in situ high-voltage electron microscopy observations, *Philosophical Magazine A*, *61*, 329–362, 1990.

Bamford, T. A., B. Hardimand, Z. Shen, W. A. T. Clark, and R. H. Wagoner, Micromechanism of slip propagation through a high angle boundary in alpha brass, *Scripta Metallurgica*, *20*, 253–258, 1986.

Barnoush, A., and H. Vehoff, In situ electrochemical nanoindentation: A technique for local examination of hydrogen embrittlement, *Corrosion Science*, *50*, 259–267, 2008.

Bassani, J. L., Single crystal hardening, *Applied Mechanics Reviews*, *43*, 320–327, 1990.

Bechtle, S., M. Kumar, B. Somerday, M. Launey, and R. Ritchie, Grain-boundary engineering markedly reduces susceptibility to intergranular hydrogen embrittlement in metallic materials, *Acta Materialia*, *57*, 41484157, 2009.

Bei, H., S. Shim, E. George, M. Miller, E. Herbert, and G. Pharr, Compressive strengths of molybdenum alloy micro-pillars prepared using a new technique, *Scripta Materialia*, *57*(5), 397–400, 2007.

Bei, H., S. Shim, G. Pharr, and E. George, Effects of pre-strain on the compressive stressstrain response of mo-alloy single-crystal micropillars, *Acta Materialia*, *56*, 47624770, 2008.

Benzerga, A., Y. Brechet, A. Needleman, and E. Van der Giessen, Incorporating three-dimensional mechanisms into twodimensional dislocation dynamics., *Modelling and Simulation in Materials Science and Engineering*, *12*, 159196., 2004.

Biener, J., A. Hodge, J. Hayes, C. Volkert, L. Zepeda-Ruiz, A. Hamza, and F. Abraham, Size effects on the mechanical behavior of nanoporous Au, *Nano letters*, *6*(10), 2379, 2006.

Brinckmann, S., J. Kim, and J. Greer, Fundamental differences in mechanical behavior between two types of crystals at the nanoscale, *Physical Review Letters*, *100*(15), 2008.

Bruemmer, S., and G. Was, Effects of irradiation on intergranular stress corrosion cracking, *Journal of Nuclear Materials*, *216*, 326–327, 1994.

Buehler, M. J., A. Hartmaier, M. A. Duchaineau, F. F. Abraham, and H. Gao, The dynamical complexity of work-hardening: a large-scale molecular dynamics simulation, *Acta Mech Sinica*, *21*, 103111, doi:10.1007/s10409-005-0019-9, 2005.

Chalmers, B., The influence of the difference of orientation of two crystals on the mechanical effect of their boundary, *Proc. R. Soc. Lond. A*, *162*, 120–127, 1937.

Clark, R., and B. Chalmers, Mechanical deformation of aluminium bicrystals, *Acta Metallurgica*, *2*, 80, 1954.

Clark, W., R. Wagoner, and Z. Shen, On the criteria for slip transmission across interfaces in polycrystals, *Scripta Metallurgica et Materialia*, *26*, 203–206, 1992.

Darby, T. P., R. Schindler, and R. W. Balluffi, On the interaction of lattice dislocations with grain boundaries, *Philosophical Magazine A*, *37, No. 2*, 245–256, 1978.

Dimiduk, D., M. Uchic, and T. Parthasarathy, Size-affected single-slip behavior of pure nickel microcrystals, *Acta Materialia*, *53*, 4065–4077, 2005.

Elkajbaji, M., and J. Thibault-Desseaux, Interactions of deformation-induced dislocations with sigma = 9(122) grain boundaries in si studied by hrem, *Philosophical Magazine A*, *58,No. 2*, 325–345, 1988.

Field, D. P., and A. Alankar, Observation of deformation and lattice rotation in a cu bicrystal, *Metallurgical and Materials Transactions A*, *42A*, 676–683, doi:10.1007/s11661-010-0570-2, 2011.

Fleck, N. A., G. M. Muller, M. F. Ashby, and J. W. Hutchinson, Strain gradient plasticity; theory and experiment, *Acta Metallurgica et Materialia*, *42*, 475, 1994.

Frick, C., B. Clark, S. Orso, P. Sonnweber-Ribic, and E. Arzt, Orientation-independent pseudoelasticity in small-scale NiTi compression pillars, *Scripta Materialia*, *59*(1), 7–10, 2008.

Friedman, L. H., and D. C. Chrzan, Continuum analysis of dislocation pile-ups: influence of sources, *Philosophical Magazine A*, *7 7, No. 5*, 1185–1204, 1998.

Gao, Y., M. Kumar, R. Nalla, and R. Ritchie, High-cycle fatigue of nickel-based superalloy me3 at ambient and elevated temperatures: Role of grain-boundary engineering, *Metallurgical and Materials Transactions A*, *36A*, 3325–3333, 2005.

Gemperle, A., N. Zarubova, and J. Gemperlova, Reactions of slip dislocations with twin boundary in fe-si bicrystals, *Journal of Materials Science*, *40*, 3247–3254, 2005.

Gerberich, W. W., J. Michler, W. M. Mook, R. Ghisleni, F. Östlund, D. D. Stauffer, and R. Ballarini, Scale effects for strength, ductility, and toughness in "brittle" materials, *Journal of Materials Research*, *24*(3), 898–906, 2009.

Gilman, J. J., *Acta Metallurgica*, *1*, 426, 1953.

Greer, J. R., and W. D. Nix, Nanoscale gold pillars strengthened through dislocation starvation, *Physical Review B*, *73*, 245–410, 2006.

Greer, J. R., W. C. Oliver, and W. D. Nix, Size dependence of mechanical properties of gold at the micron scale in the absence of strain gradients, *Acta Materialia*, *53*(6), 1821–1830, 2005.

Greer, J. R., C. R. Weinberger, and W. Cai, Comparing the strength of f.c.c. and b.c.c. sub-micrometer pillars: Compression experiments and dislocation dynamics simulations, *Materials Science and Engineering A*, *493*(1-2), 21 – 25, 2008.

Guruprasad, P. J., and A. Benzerga, Size effect under homogeneous deformation of single crystals: A discrete dislocation analysis, *Journal of the Mechanics and Physics of Solids*, *56*, 132–156, 2008.

Han, G., D. Feng, W. Ye, and H. Luo, Mechanical model on brittle crack initiation and propagation, *Journal of Materials Sciences and Technology*, *12*, 353–356, 1996.

Hauser, J. J., and B. Chalmers, The plastic deformation of bicrystals of f. c. c. metals, *Acta Metallurgica*, *9*, 802, 1961.

Henning, M., Größeneffekte auf die mechanischen eigenschaften - experiment und simulation, Ph.D. thesis, Universitt des Saarlandes, 2007.

Henning, M., and H. Vehoff, Local mechanical behavior and slip band formation within grains of thin sheets, *Acta Materialia*, *53*, 12851292, 2005.

Hirth, J. P., The influence of grain boundaries on mechanical properties, *Metallurgical Transaction*, *3*, 3047– 3067, 1972.

Hirth, J. P., and J. Lothe, *Theory of disloactions*, 764-789 pp., Wiley-Interscience Publication, 1982.

Hook, R. E., and J. P. Hirth, The deformation behaviour of isoaxial bicrytsals of fe-31967a.

Hook, R. E., and J. P. Hirth, The deformation behavior of non-isoaxial bicrystals of fe-31967b.

Hosson, J. T. M. D., W. A. Soer, A. M. Minor, Z. Shan, E. A. Stach, S. A. S. Asif, and O. L. Warren, In situ tem nanoindentation and dislocation-grain boundary interactions: a tribute to david brandon, *Journal of Materials Science*, *41*, 77047719, 2006.

Hysitron, *TriboIndenter Software Version 8.0 User Manual*, Minneapolis, MN., 2006.

Jennett, N. M., R. Ghisleni, and J. Michler, Enhanced yield strength of materials: The thinness effect, *Applied Physics Letters*, *95*(12), 123102, 2009.

Kashihara, K., and F. Inoko, Effect of piled-up dislocations on strain induced boundary migration (sibm) in deformed aluminum bicrystals with originally 3 twin boundary, *Acta Materialia*, *49*(15), 3051–3061, cited By (since 1996) 21, 2001.

Kiener, D., C. Motz, T. Schbert, M. Jenko, and G. Dehm, Determination of mechanical properties of copper at the micron scale, *Advanced Engineering Materials*, *8*(11), 1119–1125, 2006.

Kiener, D., C. Motz, M. Rester, M. Jenko, and G. Dehm, FIB damage of cu and possible consequences for miniaturized mechanical tests, *Materials Science and Engineering A*, *459*(1-2), 262–272, 2007a.

Kiener, D., M. Rester, S. Scheriau, B. Yang, R. Pippan, and G. Dehm, Influence of external and internal length scale on the flow stress of copper, *International Journal of Materials Research*, *98*(11), 1047–1053, 2007b.

Kiener, D., W. Grosinger, G. Dehm, and R. Pippan, A further step towards an understanding of size-dependent crystal plasticity: In situ tension experiments of miniaturized single-crystal copper samples, *Acta Materialia*, *56*(3), 580–592, 2008a.

Kiener, D., C. Motz, and G. Dehm, Dislocation-induced crystal rotations in micro-compressed single crystal copper columns, *Journal of Materials Science*, *43*(7), 2503–2506, 2008b.

Kiener, D., W. Grosinger, and G. Dehm, On the importance of sample compliance in uniaxial microtesting, *Scripta Materialia*, *60*(3), 148–151, 2009a.

Kiener, D., C. Motz, and G. Dehm, Micro-compression testing: A critical discussion of experimental constraints, *Materials Science and Engineering A*, *505*(1-2), 79–87, 2009b.

Kim, H. S., and Y. Estrin, Strength and strain hardening of nanocrystalline materials, *Materials Science and Engineering A*, *483484*, 127130, 2008.

Korte, S., and W. Clegg, Micropillar compression of ceramics at elevated temperatures, *Scripta Materialia*, *60*(9), 807 – 810, 2009.

Kubin, L. P., Dislocation patterning during multiple slip of F.C.C. crystals, a simulation approach, *Physica Status Solidi (a)*, *135*, 433, 1993.

Lee, S.-W., S. M. Han, and W. D. Nix, Uniaxial compression of fcc au nanopillars on an mgo substrate: The effects of prestraining and annealing, *Acta Materialia*, *57*(15), 4404 – 4415, 2009.

Lee, S.-W., D. Mordehai, E. Rabkin, and W. D. Nix, Effects of focused-ion-beam irradiation and prestraining on the mechanical properties of fcc au microparticles on a sapphire substrate, *Journal of Materials Research*, *26*(14), 1653–1661, 2011.

Lee, T., I. Robertson, and H. Birnbaum, Prediction of slip transfer mechanisms across grain boundaries, *Scripta Metallurgica*, *23*, 799–803, 1989.

Lee, T., I. Robertson, and H. Birnbaum, TEM in situ deformation study of interaction of lattice dislocation with grain boundaries in metal, *Philosophical Magazine A*, *62*, 131–153, 1990.

Lin, P., G. Palumbo, U. Erb, and K. Aust:, Modelling intergranular stress corrosion cracking in simulated three-dimensional microstructures, *Scripta Metallurgica et Materialia*, *33*, 1387, 1995.

Livingstone, J. D., and B. Chalmers, Multiple slip in bicrystal deformation, *Acta Metallurgica*, *5*, 322, 1957.

Ludwig, W., J.-Y. Buffiere, S. Savelli, and P. Cloetens, Study of the interaction of a short fatigue crack with grain boundaries in a cast al alloy using x-ray microtomography, *Acta Materialia*, *51*, 585–598, 2003.

Michler, J., K. Wasmer, S. Meier, F. Östlund, and K. Leifer, Plastic deformation of gallium arsenide micropillars under uniaxial compression at room temperature, *Applied Physics Letters*, *90*(4), 043123, 2007.

Miura, S., and Y. Saeki, Plastic deformation of aluminum bicrystals (100) oriented, *Acta Metallurgica*, *26*, 92–101, 1978.

Nadgorny, E. M., D. M. Dimiduk, and M. D. Uchic, Size effects in lif micron-scale single crystals of low dislocation density, *Journal of Materials Research*, *23*(11), 2829, 2008.

Norfleet, D., D. Dimiduk, S. Polasik, M. Uchic, and M. Mills, Dislocation structures and their relationship to strength in deformed nickel microcrystals, *Acta Materialia*, *56*(13), 2988–3001, 2008.

Nye, J. F., Some geometrical relations in dislocated crystals, *Acta metallurgica*, *1*, 153–162, 1953.

Ohmura, T., and K. Tsuzaki, Plasticity initiation and subsequent deformation behavior in the vicinity of single grain boundary investigated through nanoindentation technique, *Journal of Materials Science*, *42*, 17281732, 2007.

Östlund, F., K. Rzepiejewska-Malyska, K. Leifer, L. M. Hale, Y. Tang, R. Ballarini, W. W. Gerberich, and J. Michler, Brittle-to-ductile transition in uniaxial compression of silicon pillars at room temperature, *Advanced Functional Materials*, *19*, 2439–2444, 2009.

Pande, C., and K. Cooper, Nanomechanics of Hall-Petch Relationship in Nanocrystalline Materials, *Progress in Materials Science*, p. doi: 10.1016/j.pmatsci.2009.03.008, 2009.

Pouchon, M., J. Chen, R. Ghisleni, J. Michler, and W. Hoffelner, Characterization of irradiation damage of ferritic ods alloys with advanced micro-sample methods, *Experimental Mechanics*, pp. 1–6, 2008.

Randle, V., Grain boundary engineering: an overview after 25 years, *Materials Science and Technology*, *26*, 253–261, 2010.

Reed-Hill, R. E., and R. Abbaschian, *Physical Metallurgy Principles*, PWS Publishing company, 1994.

Rey, C., and A. Zaoui, Slip heterogeneitied in deformed aluminium bicrystals, *Acta Metallurgica*, *28*, 687–697, 1979.

Rey, C., and A. Zaoui, Grain boundary effects in deformed bicrystals, *Acta Metallurgica*, *30*, 523–535, 1982.

Schaef, W., M. Marx, H. Vehoff, A. Heckl, and P. Randelzhofer, A 3-d view on the mechanisms of short fatigue cracks interacting with grain boundaries, *Acta Materialia*, *doi:10.1016/j.actamat.2010.11.051*, 2010.

Schaef, W., M. Marx, H. Vehoff, A. Heckl, and P. Randelzhofer, A 3-d view on the mechanisms of short fatigue cracks interacting with grain boundaries, *Acta Materialia*, *59*, 18491861, 2011.

Schneider, A., B. Clark, C. Frick, P. Gruber, and E. Arzt, Effect of orientation and loading rate on compression behavior of small-scale mo pillars, *Materials Science and Engineering A*, *508*(1-2), 241–246, 2009a.

Schneider, A., D. Kaufmann, B. Clark, C. Frick, P. Gruber, R. Mönig, O. Kraft, and E. Arzt, Correlation between critical temperature and strength of small-scale bcc pillars, *Physical Review Letters*, *103*(10), 2009b.

Schoenenberger, C., Introduction to mesoscopic physics i, Internet, 2001.

Sevillano, J. G., I. O. Arizcorreta, and L. Kubin, Intrinsic size effects in plasticity by dislocation glide, *Materials Science and Engineering A*, *309-310*, 393–405, 2001.

Shen, Z., R. H. Wagoner, and W. A. T. Clark, Dislocation pile-up and grain boundary interactions in 304 stainless steel, *Scripta Metallurgica*, *20*, 921–926, 1986.

Shen, Z., R. H. Wagoner, and W. A. T. Clark, Dislocation and grain boundary interactions in metals, *Acta Metallurgica*, *36*, 3231–3242, 1988.

Sittner, P., and V. Paidar, Observation and interpretation of grain boundary compatibility effects in fe-3.3wt*37*, 1717–1726, 1989.

Soer, W., K. Aifantis, and J. D. Hosson, Incipient plasticity during nanoindentation at grain boundaries in body-centered cubic metals, *Acta Materialia*, *53*, 4665–4676, 2005.

Sun, S., B. L. Adams, and W. E. King, Observations of lattice curvature near the interface of a deformed aluminium bicrystal, *Philosophical Magazine A*, *80*, 9–25, 2000.

TSL, and EDAX, *OIM Analysis User Manual*, 2001.

Uchic, M., D. Dimiduk, J. Florando, and W. Nix, Sample dimensions influence strength and crystal plasticity, *Science*, *305*(5686), 986–989, 2004.

Uchic, M. D., and D. M. Dimiduk, A methodology to investigate size scale effects in crystalline plasticity using uniaxial compression testing, *Materials Science and Engineering A*, *400-401*, 268–278, 2005.

Volkert, C., and A. Minor, Focused ion beam microscopy and micromachining, *MRS BULLETIN*, *32*, 389–399, 2007.

Volkert, C. A., and E. T. Lilleodden, Size effects in the deformation of sub-micron au columns, *Philosophical Magazine*, *86*, 5567–5579, 2006.

Watanabe, T., An approach to grain boundary design for strong and ductile polycrystals., *Res Mechanica*, *11*, 4784, 1984.

Welsch, C., Fabrication of micropillars- elimination of ion effect, Master's thesis, Saarland University, 2010.

Welsch, C., Untersuchung der ionenschdigung von mit dem fib hergestellten nanopillars, Master's thesis, Saarland University, 2011.

Wilkinson, A. J., E. E. Clarke, T. B. Britton, P. Littlewood, and P. S. Karamched, High-resolution electron backscatter diffraction: an emerging tool for studying local deformation, *The Journal of Strain Analysis for Engineering Design*, *45*, 365–376, 2010.

Yang, B., and H. Vehoff, Dependence of nanohardness upon indentation size and grain size - a local examination of the interaction between dislocations and grain boundaries, *Acta Materialia*, *55*, 849–856, 2007.

Zaiser, M., J. Schwerdtfeger, A. Schneider, C. Frick, B. Clark, P. Gruber, and E. Arzt, Strain bursts in plastically deforming molybdenum micro- and nanopillars, *Philosophical Magazine*, *88*(30-32), 3861–3874, 2008.

Zepeda-Ruiz, L. A., B. Sadigh, J. Biener, A. M. Hodge, and A. V. Hamza, Mechanical response of freestanding au nanopillars under compression, *Applied Physics Letters*, *91*(10), 101907, 2007.